Compact, Portable Fabry-Pérot Reference Cavities

by

M. L. Kelleher

B.S., Ithaca College, 2015

M.S., University of Colorado Boulder, 2019

A thesis submitted to the

Faculty of the Graduate School of the

University of Colorado in partial fulfillment

of the requirements for the degree of

Doctor of Philosophy

Department of Physics

2023

Committee Members:

Scott Diddams, Chair

Franklyn Quinlan

Kelleher, M. L. (Ph.D., Physics)

Compact, Portable Fabry-Pérot Reference Cavities

Thesis directed by Dr. Scott Diddams

Lasers locked to optical cavities produce electromagnetic waves with exceptional frequency stability. The optical signals from optical-cavity stabilized lasers have applications in precision spectroscopy and optical atomic frequency standards. These signals can be used in gravitational wave detection and tests of fundamental physics, such as models for weakly interacting dark matter candidates. Using femtosecond frequency combs, the stability of the optical cavities can be transferred to the microwave regime. These microwave sources have some of the lowest phase noise of any microwave source. These microwave signals can be used for radar, better communications technology, and GPS.

The pursuit of portable vacuum-gap reference cavities arises from the need for rigid, compact, and robust laser frequency stabilization solutions in demanding and unpredictable environments. Many applications, such as portable optical atomic clocks, earthquake detection using undersea optical fiber, and low phase noise microwave generation, require sub- 10^{-13} instability in the optical domain, but the size, weight, and infrastructure demands of large or cryogenic cavity systems are incompatible with these applications. To address these challenges, I designed and developed three compact optical cavities. These designs represent promising steps towards achieving high stability performance while overcoming the limitations of traditional cavity systems, thereby opening up new possibilities for practical applications that require precise and portable laser frequency references.

The first design involves a series of two cavities with 6.3 mm long spacers made of ULE. These cavities were specifically tailored for low phase noise microwave generation. These cavities offer compactness while aiming to maintain high stability levels $(1-2\times10^{-14})$. One of the two cavities has 25.4 mm diameter ULE mirrors and is referred to as the ULE-ULE cavity. The other cavity has 12.7 mm diameter FS mirrors and is referred to as the FS-ULE cavity. High-bandwidth locking of the FS-ULE cavity demonstrates thermal noise limited laser noise to nearly 10 kHz. The ULE-ULE cavity was brought to a telecom fiber launch site and demonstrated remote operation. Both the FS-ULE cavity and the ULE-ULE cavity were used in a novel measurement of the cavity holding force sensitivity. The acceleration sensitivity of the FS-ULE cavity is better than $6 \times 10^{-10} g^{-1}$ along all mechanical axes.

The second design targets a portable Yb lattice clock. The spacer is made of ultra-low expansion (ULE) glass and is 25 mm long and 50 mm in diameter. The fused silica (FS) mirrors are 25.4 mm in diameter and 6.35 mm long with 10.2 m radius of curvature and crystalline coatings. This cavity has a thermal noise limited fractional frequency instability of $\approx 10^{-15}$. The design is highly symmetric, and the acceleration sensitivity is better than 2×10^{-10} per g along all mechanical axes. Preliminary phase noise measurements of a laser locked to the cavity show more than 90dB suppression of the free running laser noise, and thermal noise limited performance between 1 and 10 Hz. Preliminary measurements of the ADEV show that the laser lock is likely suffering from residual amplitude modulation (RAM) noise and drifting due to temperature. Further efforts are expected to improve the long-term stability of the cavity.

Dedication

To my mother, Kris M. Kelleher.

Acknowledgements

Thank you to Dr. Franklyn Quinlan, my direct advisor and to Dr. Scott Diddams, my academic adviser. Thank you for all of your advice and support.

Thank you to Yifan Liu, Dr. Charles McLemore, Dahyeon Lee, Dr. Takuma Nakamura, Dr. Jason Horng, Dr. James Hendrie, Dr. Josue Davila-Rodriguez, Dr. Nazanin Hoghooghi, Dr. Tara Fortier, Dr. Nick Nardelli. This work would not have been possible (or any fun) without you.

Thank you to Dr. Archita Hati, Dr. Craig Nelson, and Dr. Laura Nugent who first taught me about phase noise.

Thank you to Dr. Jeffrey Sherman who spent many hours teaching me about vacuum systems and time-keeping.

Thank you to Dr. Rich Fox, who gave me lots of advice about cavities, and also provided the ultra low expansion glass to make cavity spacers.

Thanks especially to Jose Valencia, who suggested that the NIST grad students and postdocs working on cavities get together for lunch and share ideas. I have learned a lot from my peers through those lunches. Thanks to Dr. Chun-Chia Chen, Dr. Tobias Bothwell, and Tanner Grogan for their insight and for the occasional loaning of parts.

Thanks to Dr. Andrew Ludlow and Dr. Elizabeth Donley for their comments on this thesis.

Contents

Chapter

1 Introduction **1**

1.1 How does this work fit into the existing body of research? 4

1.2 Chapter descriptions 6

2 Thermal Noise Limit **7**

2.1 Fluctuation Dissipation Theorem 7

2.2 Brownian Noise 9

2.2.1 Spacer Brownian 10

2.2.2 Mirror Substrate Brownian 10

2.2.3 Mirror Coating Brownian 12

2.3 Substrate Thermo-Elastic Noise 13

2.4 Coating Thermo-Optic Noise 16

2.5 Thermal Noise Calculations 17

3 Laser Locking **20**

3.1 Evaluating a PDH Lock 24

4 FS-ULE and ULE-ULE cavities **28**

4.1 Introduction 28

4.2 Cavity Design 29

4.3 Laser Locking 32

4.4 Phase Noise and Fractional Frequency Stability 34

5 Reference Cavity for a Portable Yb Clock **39**

5.1 Introduction 39

5.2 Cavity and System Design 40

5.3 Technical Challenges 41

5.4 Preliminary Phase Noise Measurement 43

5.4.1 Preliminary Allan Deviation Measurement 44

6 Temperature Sensitivity **46**

6.1 CTE Simulations 47

6.1.1 CTE and Holding Force 59

6.1.2 Millimeter Cavity CTE 60

6.2 Temperature Isolation & Heat Shields 60

7 Acceleration, Vibration, and Holding Force Sensitivity **66**

7.1 Holding Force 66

7.1.1 FS-ULE and ULE-ULE Holding Force Measurement 69

7.2 Acceleration Sensitivity 71

7.2.1 Theory 72

7.3 FS-ULE Flip Test Acceleration Sensitivity Measurements 75

7.4 Portable Yb Vibration Platform Test 78

8 Distributed Acoustic Sensing Using Underwater Fiber Optic Cables **84**

8.1 Measurement Setup 86

8.2 Fiber Frequency Noise Measurement 88

9 Conclusions **92**

9.1 Future Outlook 94

Bibliography **95**

Tables

Table

1.1 Physical descriptions of the cavities designed in this work. 3

2.1 Noise calculations for the different cavities. The spacer Brownian calculation includes strain energy calculated in COMSOL. The Brownian noise terms for the Yb Cavity all come from COMSOL as well (we used no analytical models for backing rings, but one could be made). All other values come from analytical solutions. The reason the thermoelastic noise is 0 for the ULE-ULE mirror is that the CTE of ULE is very small near any of the temperatures we would typically operate this cavity. This term in no significant in the total noise calculation. 19

6.1 A table of the parameters used in the COMSOL CTE simulations of the portable Yb Cavity. Note that the expression for the secant CTE of ULE is only valid when $T_{ref} = T_0$. 48

7.1 A table of the values used to calculate the acceleration sensitivity of the portable Yb axis. The acceleration noise spectrum PSD and the phase noise PSD are taken using the same resolution bandwidth, 940 mHz. The height of the peak in the acceleration noise PSD and in the phase noise PSD are entered into columns 2 and 3 and the acceleration sensitivity is calculated using these values. The modulation frequency is 11 Hz. For the V direction modulation, the 3rd and 5th harmonic are also visible on the phase noise PSD and can be used to calculate the acceleration sensitivity. . . 83

Figures

Figure

1.1 Photographs of the cavities described in this thesis. The slightly larger cavity, referred to as the Yb cavity in the text, has a 25 mm long spacer that is 50 mm in diameter. The other two cavities have the same spacer, which is 6.3 mm long and 27 mm in diameter. These cavities get referred to as the FS-ULE cavity and the ULE-ULE cavity. 3

1.2 There is a large variety of optical cavity shapes to date. In general, cavities have fractional instability inversely proportional to L. Longer cavities have lower/better instability. The instability number plotted here is the minimum reported stability. The black stars with the red outlines represent the cavities in this work. The other cavities shown here in order from shortest to longest are: red star [1], green circle [2], yellow hexagon [3], blue square [4, 5], brown diamond [6], orange pentagon [7, 8], purple triangle [9, 10], green triangle [11], yellow plus sign [12, 13], red star [14], green x [15]. The cavities in this work operate in the upper left hand corner of this plot. Traditional quartz mircowave oscillators, which is not shown in this plot, is typically $> 10^{-13}$. 5

1.3 There are many types of cm-scale frequency references each with their own advantages and disadvantages in terms of size, weight, portability, power requirements, cost, scalability/manufacturability, and environmental sensitivity. The selected works in this plot are [16], [17], [18], [19], [20], [21], the ULE-ULE cavity from this thesis [22], and another compact vacuum gap FP [1]. In general, operating at the 10^{-14} level requires a vacuum enclosure. As compact vacuum-gap Fabry-Pérot become easier to produce, they become a very attractive option for low noise frequency references. 5

2.1 The ratio of the COMSOL simulated strain energy and the calculated stain energy (which assumes that the stain is applied evenly over the spacer endfaces) versus cavity length in a Yb-like cavity. The assumption of uniform stain becomes more problematic in compact cavities, but the stain energy can easily be solved numerically in COMSOL. 11

2.2 Fractional frequency noise at 1s vs cavity length for a Yb-like cavity. By using crystalline coatings and large ROC substrates, higher performance can be fit into a compact cavity. 18

3.1 Top row: the cavity transmission, reflection dip, and reflection phase as the laser is swept through the cavity resonance. Lower left: basic PDH scheme. Laser light is sent through an elector-optic modulator (EOM) where sidebands are applied. A circulator is used to collect the reflected light on a photodetector (PD). This signal is mixed with the same frequency applied to the EOM to create the error signal (shown on the bottom right). This error signal is supplied to a loop filter (LF) or servo, which sends feedback to the laser. 21

4.1 a) Photograph of the optical cavity, which is 27 mm in diameter. The spacer is 6.3 mm thick and the mirrors are 12.7 mm in diameter and 6.35 mm thick. b) Photograph of the optical cavity in its mounting structure. The mounting structure sits on top of a Macor spacer and is placed inside of a heat shield, also pictured. c) Exploded cartoon view of the holding structure. The cavity is suspended in the Invar mounting structure by two Viton o-rings. These o-rings are held in place by two Invar holders. Note the notch on the holder that prevents the o-ring from rotating when the structure is assembled. Finally, threaded retaining rings are applied to rigidly hold the cavity in place. 30

4.2 a) Simplified block diagram of the optical cavity system. A 1550 nm laser is sent through a fiberized AOM then EOM. The light is then split in fiber. Some of the stabilized light is sent to the optical cavity. The 1550 nm laser is stabilized to the optical cavity resonance using feedback to the laser PZT, AOM, and EOM. A frequency diplexer (not shown) is used at the radio frequency (rf) input of the EOM so that the EOM can be used for both the PDH sideband generation (at 50 MHz) and feedback control. The transmission detector can provide a relative intensity noise (RIN) servo error signal, but is only utilized during flip tests to stabilize the intracavity power because the alignment is affected by the optical breadboard flexing. b) Stabilized laser light is sent on to be compared to two different optical references. One is another cavity-stabilized laser at 1550 nm. The other is a comb that is frequency-referenced to a cavity-stabilized 1156 nm laser [13]. Software defined radio (SDR) is used to track the phase of the signals, which are then cross-correlated to remove uncommon noise in the frequency combs and beat note detection. 33

4.3 Measured phase noise of the free-running commercial laser in blue, cavity-stabilized laser phase noise in green, the cavity thermal noise limit in black, an optical frequency divider in gold [23], and state-of-the-art photodetector phase noise at 10 GHz in brown [24]. The shaded region is an estimation of the statistical measurement limit of the cross-spectrum measurement of the cavity-stabilized laser phase noise given the single channel measurement levels [25]. The number of averages for each frequency offset band are: f < 100 Hz; 13 averages, 100 Hz < f < kHz; 125 averages, 1 kHz < f < 10 kHz; 1257 averages, 10 kHz < f < 1 MHz; 7954 averages. Note that the noise of the cavity-stabilized laser stays near the thermal noise limit to $\sim$ 10 kHz offset. Because the phase noise of the cavity-locked laser above 1 kHz offset frequency is at or below a state-of-the-art photodetector level, this cavity can serve as a compact, low-noise reference for OFD microwave generation. 35

4.4 Measured fractional frequency stability expressed as an Allan deviation (ADEV) of a laser locked to the primary cavity and the all-ULE cavity. An external AOM was used to compensate for a linear drift of 136 Hz/s on the locked laser. There was a residual drift of 14 Hz/s at the time of the measurement. The all-ULE cavity did not have a drift canceling AOM and the drift rate was substantially lower, 3 Hz/s at room temperature and 2 Hz/s at 55 °C. Note that the all-ULE Cavity is thermal noise limited at 1 s at 55 °C. 38

5.1 A system diagram for the laser locked to the portable Yb cavity. A commercially available 1156 nm external cavity diode laser (Littrow grating design), is used for the lock. The laser is coupled into fiber after two stages of built-in free-space isolation. A fiberized Acousto-Optic Modulator (AOM) is in the path, which is present for RIN feedback if needed. Then a fiber splitter is used to divide the light. One free-port can be used as the stabilized light output or a free space splitter may be used as well. Then the light is sent through a fiberized EOM, which is used to provide the sidebands involved in the PDH lock. After the AOM, the light is launched back into free space, where it passes through an isolator (ISO) before the circulator, which is comprised of a Faraday-Rotator (FR) and a polarization beam splitter (PBS). Transmitted light is detected and so is the reflected light. The reflected light is mixed with the same microwave frequency as is applied to the EOM, and this signal is the error signal provided to the servo or loop filter for the PDH lock. The PDH lock provides feedback to the piezo (PZT) and the current of the ECDL. 42

5.2 Preliminary phase noise measurements of the laser locked to the portable Yb cavity. Free running laser noise is shown in gold: two measurement techniques are required to measure this noise - both a frequency to voltage converter and a vector network signal analyzer was used in this measurement. The in-loop estimations of the electronic noise and random amplitude modulation (RAM) contribution are shown in the two purple traces. The measured out-of-loop phase noise is shown in blue. The estimated thermal noise limit is shown as a dotted black line. 45

5.3 A few preliminary fractional frequency instability, ADEV, measurements of the Yb Portable optical cavity. These measurements were taken periodically while trying to find the zero-CTE point of the cavity, which was, unexpectedly, not found below 55°C. These measurements of the ADEV are all significantly above the thermal noise limit. One suspected problem is the RAM, which is contributing even at 1 Hz/1s in the phase noise measurement. An active RAM cancellation lock may make an improvement here. 45

6.1 The Yb cavity geometry in COMSOL. The model is axis-symmetric around r=0. Technically, only the top half of what is drawn here is needed because the cavity is symmetric in the plane perpendicular to the optical axis (r=0 axis) as well. 49

6.2 **The right side axis and pink plot** is the simulated fractional length change of the portable Yb cavity design at different temperatures. Note that there is an arbitrary offset in the sense that the user sets the zero length change temperature, T_{ref} where $L = L_0$. **The Left side axis and purple trace** is the instantaneous CTE of the cavity as a function of temperature. Where this line crosses zero, the cavity is the least sensitive to temperature. This plot is for the simulation of the Yb cavity with all of the default/expected parameters. The zero-crossing in this case ≈ 44°C 52

6.3 This plot demonstrates the sensitivity of the cavity CTE to the zero-crossing of the ULE used in the spacer when there are no backing rings on the cavity. The cavity CTE is not very sensitive the ULE CTE zero-crossing. This method cannot be used to change the effective cavity CTE to above room temperature. 53

6.4 This plot shows that the cavity CTE is sensitive the CTE zero-crossing of the ULE used in the spacer and the backing rings. With backing rings, the strain between the mirror and spacer is minimized and the zCTE of the cavity is nearly the zCTE of the spacer. 53

6.5 This plot shows the cavity CTE dependence on backing ring inner radius. In this case, 1 mm diameter represents nearly a full disk and 10 mm diameter represents the thinnest ring simulated. More backing ring contact with the mirror represent causes a higher cavity CTE, but a hole in the backing ring is required for the AR coating on the mirror and to avoid etalons in the backing ring. 55

6.6 This plot shows how the cavity CTE depends on the thickness or height of the backing ring. There are diminishing returns for increasing backing ring thickness. There is almost no change in the cavity CTE zero-crossing from 6mm-10mm. 56

6.7 This plot demonstrates cavity CTE dependence on contact area when there is no backing ring. Imperfections in mirror or spacer polishing can limit the contact area. Without a backing ring, these variations can make the exact cavity CTE at room temperature difficult to predict. 56

6.8 This plot demonstrates cavity CTE dependence on contact area when a backing ring is applied to the cavity mirrors. Imperfections in mirror or spacer polishing can limit the contact area. However, the presence of a backing ring, reduces the effective CTE sensitivity to stain in the mirror-spacer interface and also variations in contact area. 57

6.9 A measurement of the cavity frequency vs temperature. A a parabolic fit is used to estimate the expected zero-crossing. 57

6.10 The measured instantaneous cavity CTE vs the COMSOL simulated cavity CTE. . 58

6.11 The simulated CTE of the cavity when the displacement in the holding rings is equal to the displacement of the holding structure (worst case scenario). The effective cavity CTE does change in these conditions, but not enough to explain the discrepancy in the measured cavity CTE. 61

6.12 A measurement of the relative frequency shift of the all ULE mm-scale cavity versus temperature. Surprisingly, no zero-crossing was found below 55 °C. The spacer was made of legacy ULE stored at NIST and has unkown material properties. 61

6.13 The simulated (blue) and calculated (orange) transfer function for two layers of aluminum heat shields with an emissivity of 0.4. The time constant of this system is greater than half a day. 63

6.14 Photograph of the optical cavity mount and the heat shields. The mounting structure is made of heat-treated Invar. The structure supported by PEEK screws and PEEK spacers are used to separate the heat shields. PEEK is used because of its low thermal conductivity. The heat shields are made of Aluminum and have been polished to increase the emissivity. In this photo a PEEK base plate is used to attach the structure to a 6” CF vacuum flange, however, this piece was later replaced with an identically shaped Macor part. This was because the PEEK base plate was found to increase the vacuum pressure of the chamber. PEEK is considered a vacuum-compatible material at the pressures we are interested in, $\sim 10^{-7}$ Torr, so there may have been a problem with this particular sample. We make no claim about the vacuum compatibility of these materials. 64

6.15 Laser frequency change versus time for two different temperature changes applied to the outside of the vacuum can for the Yb cavity. 65

7.1 A cartoon demonstrating how where a linear elastic cylinder is held on its endfaces might change the length along the z-axis of the cylinder. In the first case, when the edges of the cylinder are compressed, the cylinder bows outward, representing and increase in cavity length. In the second case, when the compression occurs along the center of the cylinder, the endfaces bow inward, representing a decrease in cavity length. 66

7.2 A holding force sensitivity plot for the Yb cavity based on COMSOL simulations. With the green trace, the spacer diameter is set to 40 mm. There is no holding force zero-crossing before the edge of the spacer with this cavity. In the gold trace, the spacer diameter is set to 50 mm. There is a zero-crossing in the holding force sensitivity near 45 mm in this case. In general, more "pancake-like" (R larger than L) cylindrical cavities have holding force zero-crossings. 68

7.3 **Left:** an exaggerated cartoon showing the contact area between the mirror and spacer. **Right:**A plot showing holding force sensitivity vs o-ring diameter for the ULE-ULE cavity. Each trace represents a different contact area between the mirror and spacer. From top to bottom the contact area decreases. The contact area between the mirror and spacer is a variable that can be difficult to control exactly due to variations in the polishing step and a very small sag in the mirror for large radius of curvature, but the green trace is the ideal and the blue trace is similar to what we observed in the lab as the clear area between the mirror and spacer. 70

7.4 a) Photographs of the primary cavity and the supplemental all-ULE cavity. The cavities have identical spacers, but different mirrors. b) Experimental results showing the holding force sensitivity's dependence on o-ring size, demonstrating excellent agreement with the finite element analysis results, which are shown as shaded regions. The y-error bars are a combination of the standard deviation in the frequency shift measurement and the uncertainty in the mass of the weight applied. This does not include any systematic offsets. The x-axis uncertainty is an estimate based on the thickness of the o-ring (1 mm). Simulations incorporated a range of mirror-spacer contact areas, where the contact annulus width varied from 3.2 mm to 2.5 mm in the FS-ULE cavity, and 6.4 mm to 5.1 mm in the all-ULE cavity. 70

7.5 Photographs of the flip table that was used in the FS-ULE cavity acceleration sensitivity measurement next to a cartoon illustration of how the cavity orientation will change during the flip. In this case, the cavity vacuum vent hole goes from pointing up to pointing down. 76

7.6 Preliminary acceleration sensitivity measurement of the FS-ULE cavity using the flip tests. A linear drift (presumably due to temperature) has been removed from the measurement. Mechanical axis 1 corresponds to the flip which takes the vent hole on the cavity from up to down. Mechanical axis 2 flips the cavity axis that is perpendicular to both the vent hole and the optical axis. Mechanical axis 3 flips the optical axis. The acceleration sensitivity of axes 1, 2, and 3 are $3 \times 10^{-9} g^{-1}$, $4 \times 10^{-10} g^{-1}$, and $1 \times 10^{-10} g^{-1}$. 77

7.7 a) Diagram of the cavity indicating the mechanical axis along which the cavity is flipped. In the red flip test, the cavity vent hole goes from up to down. In the blue flip test, the optical axis is flipped, and in the black flip test, the mechanical axis which is perpendicular to both the vent hole and the optical beam is flipped. b) Flip test measurements of the primary cavity acceleration sensitivity. The cavity is flipped along three mechanical axes inducing a 2g acceleration change while a laser stays locked to the cavity. The change in frequency is observed. Linear drift, attributed to cavity temperature change, is removed from the data. The worst axis is $6 \times 10^{-10} \frac{\Delta L}{L}$ per g, and this axis corresponds to flipping the vent hole up and down. The asymmetry caused by the vent hole is likely contributing to higher acceleration sensitivity along this axis. 79

7.8 Phase noise measurement of the portable Yb cavity against a reference. The reference noise level is significantly above the noise of the portable Yb cavity, but it is low enough to see some phase noise response at the modulation tone for the acceleration sensitivity measurement. The green trace is the phase noise when there is no modulation. The red trace is the V modulation, which is closely aligned with g. The light blue trace is the H1 modulation, which is closely aligned with the optical axis of the cavity. The dark blue trace is the H2 modulation perpendicular to the previous two axes. 81

7.9 The acceleration noise spectrum when the v-direction modulation is engaged. The measurement is taken along all three mechanical axes to confirm the coupling to the other axes is minimal. 81

7.10 The acceleration noise spectrum when the H1-direction modulation is engaged. The measurement is taken along all three mechanical axes to confirm the coupling to the other axes is minimal. 82

7.11 The acceleration noise spectrum when the H2-direction modulation is engaged. The measurement is taken along all three mechanical axes to confirm the coupling to the other axes is minimal. 83

8.1 Map of the underwater telecom fibers from TeleGeography [26]. 85

8.2 Photographs showing packaging and shipping of the ULE-ULE cavity. The free space optical components, fiber components, vacuum can and cavity all fit inside of a box that is 15.7 in x17.7in x14in. This box fits inside of a Pelican shipping case and was mailed to the fiber launch site. A NEG ion pump combo is used to maintain vacuum. The ion pump was not on durring the shipping stages. At the launch site, this box and a few additional microwave components are installed in a standard 18" rack. Further reductions in the volume of the cavity stabilized laser system will be implemented in future demonstrations. 85

8.3 Light from the cavity stabilized laser is sent through a single side band EOM which applies a sawtooth frequency sweep (there are actually two polarization channels each with separate sawtooth frequency sweeps - these channels can be separated at the end). The fiber is then sent under the Atlantic ocean. There are periodic erbium-doped fiber amplifiers (EDFA) which are followed by fiber Bragg gratings which send a small portion of the line monitoring signal backwards through a separate fiber. This signal is normally used to check the health of the amplifiers, but can be used for our purposes as the sensing light. Back at the launch site, the return signal is combined with a portion of the cavity stabilized light before frequency modulation, detected, and digitally demodulated. For details on the signal acquisition please see Mazur et al. [27] 87

8.4 Plots of the frequency noise of each reflector. The color indicates the closeness of the detector with dark navy representing detectors that are close to the fiber launch and light teal representing detectors that are further away. The right plot shows the measurement made using a commercial etalon stabilized laser. The left plot shows the fiber noise measurement using our cavity stabilized laser. These measurements were made at different times, so it is possible that the fiber noise changed in between these measurements. However, it does look like there may be some reference-limited noise above 100 Hz. In this region, the cavity stabilized laser looks like it would be a better choice as a reference laser. Note that at the low frequency end, there is little variation between the spans with either laser. This is because the noise in the first few reflectors is dominating and the further spans are not contributing much. . . . 90

8.5 Phase vs time for each reflector. The color indicates the closeness of the detector with dark navy representing detectors that are close to the fiber launch and light teal representing detectors that are further away. 90

8.6 A comparison of the noise spectrum measured with a commercial available etalon stabilized laser vs the compact cavity stabilized laser. Below 100 Hz, no obvious improvement to the noise can be identified when comparing the two systems. Some bands look quieter, but hard to make a conclusion knowing that the fiber noise may be different in the two measurements. From 100 Hz – 10 KHz, we see an improvement in the noise. However, above 1 kHz, both systems appear to be limited by laser noise, though the cavity stabilized noise level appears lower. The color indicates the closeness of the detector with dark navy representing detectors that are close to the fiber launch and light teal representing detectors that are further away. 91

Chapter 1

Introduction

Lasers frequency-locked to the resonance of a vacuum-gap Fabry-Pérot (FP) optical cavity have reached fractional frequency instability lower than 1×10^{-16} at 1 s of averaging time [15, 10]. The frequency instability is inherited from the fluctuations in cavity length as sampled by an optical beam. The sampled length fluctuations can be reduced to less than the diameter of a proton. Such extraordinary performance in laser frequency stability has aided in the advancement of state-of-the-art laboratory optical atomic clocks, with applications in the redefinition of the SI second [28] and tests of fundamental physics [29]. The best fractional frequency stabilities in cavity-stabilized lasers are achieved by exploiting long cavity lengths (up to ~ 48 cm [30, 15]), operation at cryogenic temperatures [10], and extensive environmental isolation by way of vibration-insensitive mounting and multiple layers of thermal isolation [31, 32]. However, many out-of-the-lab applications of stable lasers, such as portable optical atomic clocks [33], earthquake detection using undersea optical fiber [34], and low phase noise microwave generation via optical frequency division (OFD) [35, 23], benefit from the sub-10^{-13} stability available in the optical domain, but are incompatible with the size, weight, and infrastructure requirements of large or cryogenic cavity systems. Furthermore, short cavities have the potential for inherently low acceleration sensitivity without the need for active vibration stabilization [36].

The search for laser frequency reference cavities that are rigidly held, have reduced size and weight, and can operate in harsh and unpredictable environments has led to the development of both solid-state dielectric resonators [18, 19, 17, 20, 21], and compact vacuum-gap FPs [1, 4, 3, 37, 7, 31, 38]. Solid-state dielectric resonators are impressively small, typically millimeter-scale, and, in some cases, can be manufactured at scale. However, these resonators suffer from higher thermorefractive noise and temperature sensitivity that has limited the fractional frequency instability to the 10^{-13} level and above [21]. By placing the optical mode in vacuum and using low expansion materials, compact and rigidly held FPs can reach fractional frequency stabilities $\sim 1 \times 10^{-15}$ with a cavity volume near 60 mL [1]. Notably, simulations of the noise of vacuum-gap FPs predict that their size can be reduced to only a few milliliters while maintaining fractional frequency stability performance well below the 10^{-13} level of the best solid-state dielectric resonators; indeed, a recent demonstration of a 10 mm-long, 8 mL-volume cavity reached 6×10^{-15} [39], albeit without testing of holding force or acceleration sensitivity. Thus, there remains a compelling performance space that can be achieved with a compact FP optical frequency reference, provided that a laser locked to the FP can operate with noise at or near the cavity thermal noise limit, and the FP has low acceleration and holding force sensitivity.

In this thesis we will present two main designs for portable vacuum-gap reference cavities.

- A series of two cavities with 6.3 mm long spacers that have been designed with low phase noise microwave generation in mind
- An optical cavity designed for a portable Yb lattice clock with a 25 mm long spacer.

A photograph of these cavities can be found in Fig. 1.1 and a table with a basic description of the cavities can be found Table 1.1. The Yb cavity has an ultra-low expansion (ULE) glass spacer, fused silica (FS) mirrors, and ULE backing rings. The FS-ULE cavity has FS mirrors and a ULE spacer. The ULE-ULE cavity has ULE mirrors and a ULE spacer.

The measurements on the FS-ULE cavity and the ULE-ULE cavity are complete. The ULE-ULE cavity is currently being used in another system to generate microwaves [40]. The measurements on the Yb cavity are only preliminary and further efforts are needed to demonstrate the full performance capabilities of this system. I report the preliminary results in the thesis and simulation work so that future members of the lab may return to this cavity if desired to pick up

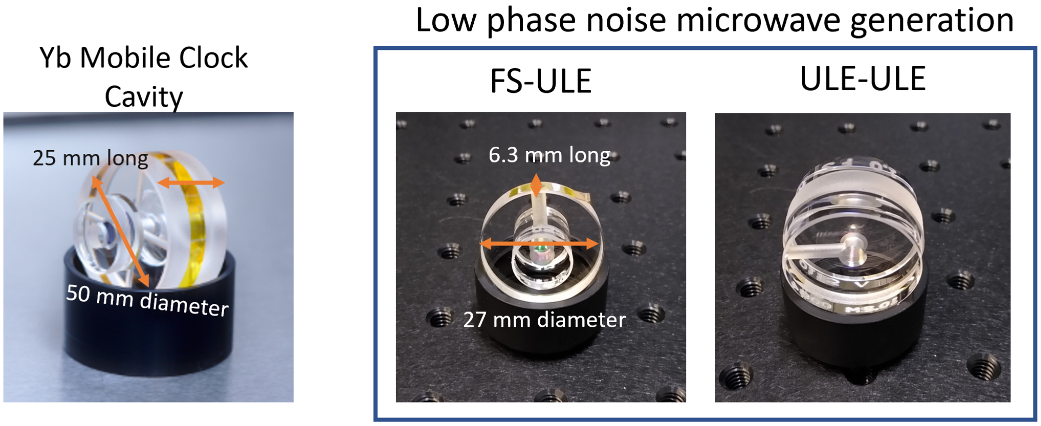
Yb Mobile Clock Cavity
25 mm long
50 mm diameter
Low phase noise microwave generation
FS-ULE
6.3 mm long
27 mm diameter
ULE-ULE

Figure 1.1: Photographs of the cavities described in this thesis. The slightly larger cavity, referred to as the Yb cavity in the text, has a 25 mm long spacer that is 50 mm in diameter. The other two cavities have the same spacer, which is 6.3 mm long and 27 mm in diameter. These cavities get referred to as the FS-ULE cavity and the ULE-ULE cavity.

Table 1.1: Physical descriptions of the cavities designed in this work.

	Yb Cavity	**FS-ULE Cavity**	**ULE-ULE Cavity**
Spacer length	25 mm	6.3 mm	6.3 mm
Spacer diameter	50 mm	27 mm	27 mm
Spacer material	ULE	ULE	ULE
Mirror length	6.35 mm	6.35 mm	6.35 mm
Mirror diameter	25.4 mm	12.7 mm	25.4 mm
Mirror substrate material	FS	FS	ULE
Mirror coating material	crystalline (GaAs/AlGaAs)	dielectric	dielectric
Mirror ROC	10.2 m	1 m	1 m
ULE backing ring?	Yes	No	No
Number of vent holes	4	1	1
Measured finesse	330,000	680,000	940,000
Design wavelength	1156 nm	1550 nm	1550 nm

where I leave it off.

1.1 How does this work fit into the existing body of research?

In order to understand the relevance of this work it makes sense to summarize a selection of the previous work to date on both vacuum-gap FPs and cm-scale frequency references. There have been many vacuum-gap FP cavities to date with many different sizes and shapes. A selection of these works can be found in Fig. 1.2 which is a plot of fractional instability vs. cavity spacer length. In general, longer cavities have lower instability, with some advantages given to cavities that operate at cryogenic temperatures or utilize crystalline materials in the coatings. However, longer cavities are typically more sensitive to vibration and acceleration and cryogenic systems are typically not portable. For portable systems, it makes sense to aim for more compact geometries that have passive vibration-insensitivity.

The cavity designs in this work build off of a previous design from this lab [1], which is cylindrical. The cylindrical geometry has a high degree of symmetry (important to low vibration sensitivity) and it has two flat endfaces, which can be used to mount the cavity. It is also a relatively simple shape which can manufactured easily.

There are also a number of other resonator types, and a selection of cm-scale resonators can be found in Fig. 1.3. Each of these resonators has advantages and disadvantages, but to achieve frequency instabilities at the 10^{-14} level or better typically requires vacuum operation. This is because when the resonant light propagates through a material or gas, it picks up additional thermo-refractive noise. One potential disadvantage of vacuum-gap FP cavities, is the use of standard mirrors, which are shaped and polished in small batches. However, there have been recent advances showing that cavity mirrors can be made using lithographic techniques [41] and these cavities can even be integrated with waveguide-based lasers [42]. Additionally, a new result from Liu et al. shows how a cavity might be vacuum bonded in order to eliminate the bulky vacuum can and ion-pump typically required for vacuum-gap devices [43].

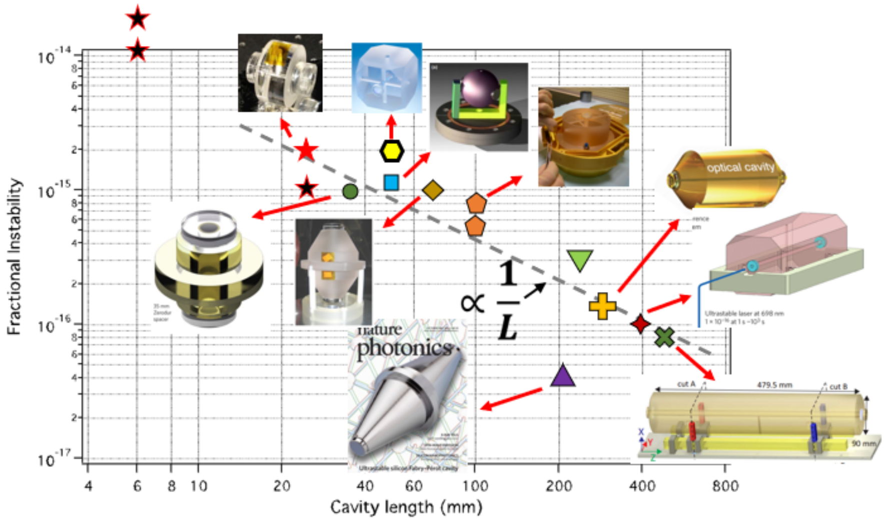

Figure 1.2: There is a large variety of optical cavity shapes to date. In general, cavities have fractional instability inversely proportional to L. Longer cavities have lower/better instability. The instability number plotted here is the minimum reported stability. The black stars with the red outlines represent the cavities in this work. The other cavities shown here in order from shortest to longest are: red star [1], green circle [2], yellow hexagon [3], blue square [4, 5], brown diamond [6], orange pentagon [7, 8], purple triangle [9, 10], green triangle [11], yellow plus sign [12, 13], red star [14], green x [15]. The cavities in this work operate in the upper left hand corner of this plot. Traditional quartz mircowave oscillators, which is not shown in this plot, is typically $> 10^{-13}$.

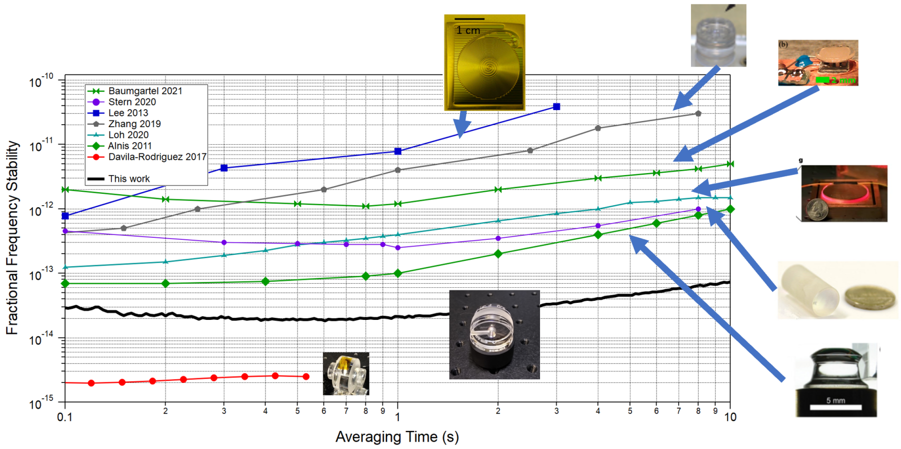

Figure 1.3: There are many types of cm-scale frequency references each with their own advantages and disadvantages in terms of size, weight, portability, power requirements, cost, scalability/manufacturability, and environmental sensitivity. The selected works in this plot are [16], [17], [18], [19], [20], [21], the ULE-ULE cavity from this thesis [22], and another compact vacuum gap FP [1]. In general, operating at the 10^{-14} level requires a vacuum enclosure. As compact vacuum-gap Fabry-Pérot become easier to produce, they become a very attractive option for low noise frequency references.

1.2 Chapter descriptions

In chapter 2, I will describe the fundamental noise limit of a FP and how to calculate and optimize this property. Chapter 3 is about locking the laser to the cavity using PDH locking. Chapter 4 is about measurements made on the FS-ULE and ULE-ULE cavity. Chapter 5 is about the preliminary measurements made on the Yb cavity. Chapter 6 and chapter 7 are about reducing a cavity's sensitivity to temperature and acceleration, respectively. Chapter 8 is about using the ULE-ULE cavity in a real-world application: undersea fiber-optic cables as sensors.

Chapter 2

Thermal Noise Limit

Lasers locked to optical cavities have a fundamental noise limitation arising from the volumetric and temperature fluctuations in the spacer, mirrors, and mirror coatings. There are different kinds of noise sources with different names:

- Brownian noise of the spacer, mirror substrate, and mirror coatings: a solid at a finite temperature undergoes random volumetric fluctuations, causing the surface of the solid to move relative to its center of mass.
- Thermoelastic noise in the mirror substrate: stochastic temperature fluctuations cause the substrate to change its length through the material coefficient of thermal expansion.
- Thermo-optic noise in the mirror coating: stochastic temperature fluctuations cause changes in length of the coating through the coefficient of thermal expansion and through temperature-dependent index changes of the material.

In this section I will describe the different noise sources and how to calculate their noise contributions either analytically or numerically. I will also provide the calculated noise for each of the cavities described in this thesis.

2.1 Fluctuation Dissipation Theorem

To quantitatively determine the thermal noise limit of a laser locked to a cavity, there are two approaches. Firstly, one can treat the optical cavity mechanical motions as a set of discrete modes, each populated by thermal energy [44, 45]. Each mode has a mechanical quality factor, dictating the frequency range over which the noise of that mode is spread. Additionally, each mode has an effective coefficient that describes the displacement experienced by the mirrored surface when the mode is excited to a certain amplitude. By summing the contributions from all relevant modes, we obtain the overall noise level. This method provides a clear mechanical picture, but is cumbersome because it can involve identifying and calculating the noise resulting from many mechanical resonances.

The second approach involves the Fluctuation Dissipation Theorem (FDT) [46]. The FDT relates irreversible dissipative processes (like those where heat is produced) with thermally driven fluctuations. The impedance of a particular physical variable is related to the fluctuations of that same variable in thermodynamic equilibrium. This is the generalized relationship for Johnson-Nyquist Noise (where the voltage noise in thermal equilibrium is related to the electrical resistance), grey body radiation (where the absorption is related to the radiation in thermal equilibrium), and Brownian motion (where drag is related to the motion in thermal equilibrium).

Levin's direct approach to calculating the thermal noise uses the FDT and is often the preferred method for calculating the noise in optical cavities [47]. For an optical cavity, the fluctuations that we are after are those that change the distance between the two mirrors, x, as sampled by the optical beam. These length fluctuations fundamentally limit the fractional frequency fluctuations, $S_y(f) = S_x(f)/L^2$, in the laser locked to the optical cavity (assuming all other sources of noise are suppressed). The power spectral density in the length fluctuations, $S_x(f)$, can be calculated by applying a force, F_0, in the shape of the optical beam on each mirror surface. For a Gaussian beam, we apply the pressure function:

$$P(t) = \frac{2F_0}{\pi w_0^2} e^{-2r^2/w_0^2} \cos(2\pi f t), \tag{2.1}$$

where ω_0 is the spot size and f is the frequency of the oscillation. We then calculate the time-averaged dissipated power, W_{diss}, for this applied pressure, which is related to the length fluctuations by:

$$S_x(f) = \frac{2k_BT}{\pi^2 f^2}\frac{W_{diss}}{F_0^2}, \tag{2.2}$$

where T is the temperature and k_B is the Boltzmann constant.

By finding the power dissipated due to the applied force, the noise can be determined. This can be determined analytically (under a few simplifying assumptions) or numerically. We will walk through some of the approaches in the following sections.

2.2 Brownian Noise

Kessler et al. used Levin's direct approach to calculate Brownian noise in optical cavities, and much of the following section is from that paper [48]. Numata et al. is also a good reference here [49]. To calculate the Brownian noise, we need the time-averaged dissipated power, and for that we need to understand the friction in the test mass (mirror substrate, mirror coating, or spacer). When you press on a linear elastic material, it will compress according to the Young's modulus, E. If the friction in the test mass comes from homogeneously distributed damping, it can be expressed as an imaginary component of the Young's modulus, $E(f) = E_0[1 + i\phi(f)]$, where $\phi(f)$ is the loss angle. The loss angle for many materials of interest, like FS and ULE, is taken to be a constant over the frequency ranges we are interested in. W_{diss} is related to the loss angle by:

$$W_{diss} = 2\pi f U\phi \tag{2.3}$$

where U is the maximum elastic strain energy when the displacement caused by the oscillating pressure is maximized. The cavities we are interested usually have mechanical resonances much greater than 100 kHz. As a result, U is constant over the frequency range of interest. We can apply a constant force, F_0 at $f = 0$, and use that number to calculate U for all f in the range of interest.

To get the total Brownian noise in the cavity, the contributions of the spacer, two substrates, and two mirror coatings must be summed.

$$\begin{aligned} S_x(f) = &\ S_x^{sp}(f) + 2S_x^{sb}(f) + 2S_x^{ct}(f) \\ S_x(f) = &\ \tfrac{4k_bT}{\pi f F_0}(U_{sp}\phi_{sp} + 2U_{sb}\phi_{sb} + 2U_{ct}\phi_{ct}) \end{aligned} \tag{2.4}$$

2.2.1 Spacer Brownian

To estimate the noise contribution of the spacer, one approach is to consider that the applied force to the mirror surface is causing the mirror to apply pressure evenly over the endfaces of the spacer. This ignores any variation in the stress in the mirror-spacer interface. Take a spacer of length, L, radius, R_{sp}, and central bore radius, r_{sp}, with Young's modulus, E. Now the strain energy is

$$U_{sp} = \frac{L}{2\pi E(R_{sp}^2 - r_{sp}^2)} F_0^2 \tag{2.5}$$

and the resulting length fluctuations in the spacer are

$$S_L(f) = \frac{4k_bT}{\pi f} \frac{L}{2\pi E(R_{sp}^2 - r_{sp}^2)} \phi_{sp}. \tag{2.6}$$

This estimate works pretty well, but for small cavities, the variation in the stress on the end of the spacer becomes a non-negligible fraction of the strain energy calculation. To get a sense of how this works, I simulated a cavity with the same parameters as the Yb cavity (see Table 1.1), but I varied the spacer length in a finite element anlysis (FEA) software, COMSOL. Fig. 2.1 shows how the ratio between the COMSOL calculated spacer strain energy and the analytically calculated strain energy changes as a function of spacer length. In COMSOL, we apply a constant force in the shape of the fundamental cavity mode to the simulated cavity mirrors and extract U. For short cavities, the assumption of uniformly applied strain becomes more problematic, but COMSOL can be used to calculated the strain energy numerically.

2.2.2 Mirror Substrate Brownian

For calculating the Brownian noise of the mirror coating and substrate, it is useful to consider the shape of the pressure applied over the Gaussian beam profile with $1/e^2$ beam radius, ω_0:

$$p(r) = \pm \frac{2F_0}{\pi\omega_0^2} e^{-2r^2/\omega_0^2}. \tag{2.7}$$

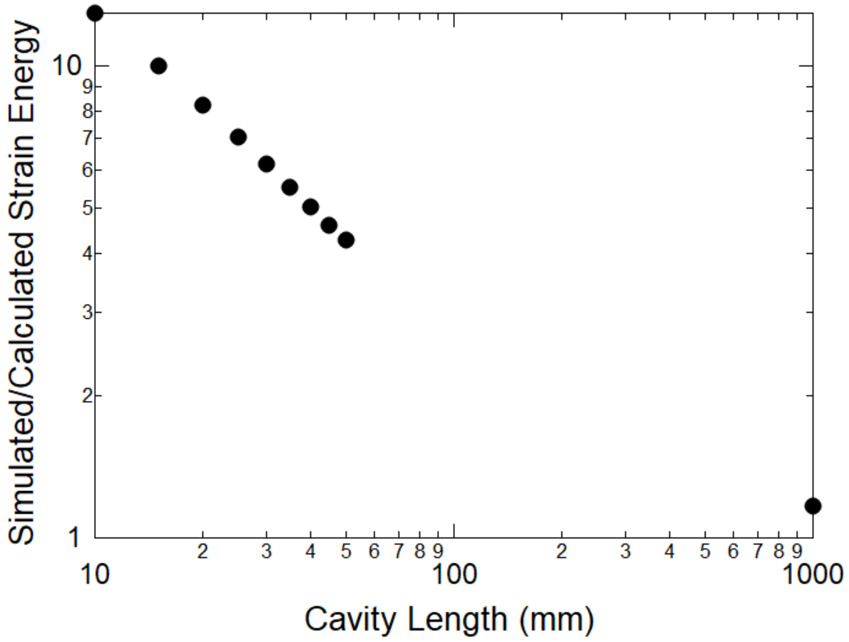

Figure 2.1: The ratio of the COMSOL simulated strain energy and the calculated stain energy (which assumes that the stain is applied evenly over the spacer endfaces) versus cavity length in a Yb-like cavity. The assumption of uniform stain becomes more problematic in compact cavities, but the stain energy can easily be solved numerically in COMSOL.

Here f has again been set to 0 because W_{diss} is constant for frequencies well below the mechanical resonances of the cavity. For many cavity geometries, the spot size, ω, is much smaller than the mirror dimensions, and it is reasonable to treat the mirror as an infinite half-space. In this case, the maximum stain energy is

$$U_{sb} = \frac{1-\sigma^2}{2\sqrt{\pi}E\omega}F_0^2. \tag{2.8}$$

The corresponding length fluctuations are therefor

$$S_x^{sb}(f) = \frac{4k_bT}{\pi f}\frac{1-\sigma^2}{2\sqrt{\pi}E\omega}\phi_{sb}, \tag{2.9}$$

where σ is the Poisson's ratio. Treating the mirrors as an infinite half-space works well for the cavities described in this thesis, but for a more thorough analysis of finite mirrors, see Bondu et al. and Liu and Thorne [50, 51].

2.2.3 Mirror Coating Brownian

To find the Brownian coating noise, we assume a uniform loss angle, ϕ_{ct}, by taking a weighted average of the loss angels of the layers in the coating. The coating is a thin layer of thickness, d, on top of the substrate, and the strain energy of the coating depends on the strain energy in the substrate:

$$\begin{aligned} U_{ct} &= U_{sb}\tfrac{2}{\sqrt{\pi}}\tfrac{1-2\sigma}{1-\sigma}\tfrac{d}{w} \\ s_x^{ct}(f) &= S_x^{sb}\tfrac{2}{\sqrt{\pi}}\tfrac{1-2\sigma}{1-\sigma}\tfrac{d}{w}\tfrac{\phi_{ct}}{\phi_{sb}} \end{aligned} \tag{2.10}$$

For compact cavities, the coating noise is a significant fraction of the total thermal noise, which means that there can be great benefits to reducing this term. One way to approach this would be to increase the spot size on the cavity. Typically, this involves increasing the radius of curvature (ROC) of the cavity mirrors. There is a trade off here though. Large ROC mirrors also mean a strong sensitivity to the tilt or an offset between the mirrors, which can reduce cavity finesse by introducing extra loss into the cavity or make it difficult to get a cavity mode at all. Additionally, in typical grind and polish cavity mirrors with contact annulus it is difficult to obtain larger than 10 m ROC for mirrors that are 25.4 mm in diameter and larger than 1 m ROC for mirrors that are 12.7 mm in diameter (both standard substrate sizes). This is because the sag on these mirrors for these ROCs is so small ($\approx 10\mu$m) that achieving a nice polish on both the curved mirror and the flat contact annulus (required for optical contact bonding the mirror to the spacer) is difficult. Experimentally, we have found that the cavities that are 6.3 mm in length are more likely to have a high finesse mode with 1 m ROC mirrors than with 10 m ROC mirrors (due to beam walk-off in the case of an angle between the two mirror surfaces or a small offset in the mirror placement).

Another approach to reducing coating thermal noise is to reduce the loss angle of the coating material. Crystalline mirrors, such as AlGaAs/GaAs mirrors, have smaller loss angles [2]. These mirrors can have a polarization mode splitting. Kedar et al. measured a strange polarization noise in cavities with extremely low noise [52]. In the case of the Yb cavity, we do not observe the polarization related noise, but extra care must be taken with mode matching. A typical circulator uses a $\lambda/4$ waveplate, but a Faraday rotator allows for better mode matching into just one polarization state.

2.3 Substrate Thermo-Elastic Noise

A material at temperature T undergoes constant stochastic temperature fluctuations, which in turn generate length noise on the surface of the solid. This noise arises from the expansion and contraction of the substrate as a result of temperature changes via the material coefficient of thermal expansion, α,

$$\alpha = \frac{dL}{LdT}. \tag{2.11}$$

As the material expands and contracts due to these stochastic temperature fluctuations, the position of the surface, as detected by a light beam, experiences shifts. It is important to note that this type of noise, known as thermoelastic noise, should be distinguished from the direct volumetric fluctuations referred to as Brownian noise.

This noise can be calculated using the Fluctuation Dissipation Theorem, which we take mostly from another article by Liu and Thorne [51]. First, we again apply an oscillating pressure in the shape of the optical beam:

$$P(t) = \frac{2F_0}{\pi\omega_0^2} e^{\frac{-2r^2}{\omega_0^2}} \cos(\omega t) \tag{2.12}$$

This oscillating pressure causes a material strain from the compression and expansion of the surface. The noise spectrum is related to time averaged power dissipated, W_{diss}:

$$S(\omega) = \frac{2k_B T W_{diss}}{F_0^2 \pi^2 f^2}. \tag{2.13}$$

In the case of thermoelastic noise, W_{diss} is:

$$W_{diss} = \left\langle T\frac{dS}{dT} \right\rangle = \left\langle \int \frac{\kappa}{T} (\nabla \delta T)^2 \, dV \right\rangle \tag{2.14}$$

Where S is the entropy and κ is the thermal conductivity of the material. To solve this equation, we need to find out how δT changes with the pressure applied $P(t)$. Again, because the vibrational modes of the cavity are so high frequency (higher than any noise offset frequency of interest), we can treat the problem as quasi static. That is, that the strain responds instantaneously to $P(t)$. The equation for the quasi-static stress balance is as follows:

$$(1-2\sigma)\nabla^2\vec{u} + \vec{\nabla} \cdot (\nabla \cdot \vec{u}) = 0 \tag{2.15}$$

Where σ is Poisson's ratio, and $\vec{u}$ is the strain displacement vector.

The heat equation can be expressed as:

$$\frac{\partial(\delta T)}{\partial t} - a^2 \nabla^2(\delta T) = q \tag{2.16}$$

Here, $a^2 = \frac{\kappa}{\rho C}$ and q represents the source term originating from the compression or expansion of the material. It can be defined as:

$$q = -\frac{\alpha E T}{\rho C (1-2\sigma)} \frac{\partial(\vec{\nabla} \cdot \vec{u})}{\partial t} \tag{2.17}$$

Now,

$$\frac{\partial(\delta T)}{\partial t} - a^2 \nabla^2(\delta T) = -\frac{\alpha E T}{\rho C (1-2\sigma)} \frac{\partial(\vec{\nabla} \cdot \vec{u})}{\partial t} \tag{2.18}$$

By solving this equation for $\delta T(x, y, z)$, we can calculate W_{diss} and subsequently obtain $S(\omega)$.

For short time scales and large optical spot sizes, heat flow can often be neglected, which corresponds to the adiabatic limit. The frequencies at which heat diffusion becomes significant are determined by $\omega_c < \frac{2\kappa}{\rho C w_0^2}$.

Taking the example of fused silica ($\kappa = 1.4$ W/m/K, $C = 730$ J/kg/K, $\rho = 2210$ kg/m) and a spot size on the mirror w_0 of $100\,\mu$m, we find $\omega_c = 90$ rad/s In the adiabatic limit, we can drop the $a^2\nabla^2(\delta T)$ term in the heat flow equation, resulting in:

$$\delta T = -\frac{\alpha E T}{\rho C(1-2\sigma)}\nabla \cdot \vec{u} \tag{2.19}$$

The energy dissipation rate then becomes

$$W_{diss} = \left(\kappa T\left(\frac{\alpha E}{\rho C(1-2\sigma)}\right)\right)^2 \left\langle \int (\vec{\nabla} \cdot (\vec{\nabla} \cdot \vec{u}))^2 \, dV \right\rangle \tag{2.20}$$

The calculation of the integral for an infinite half-plane is given in Liu and Thorne [51]. These solutions rely on the static stress balance equation under the influence of the pressure function $P(t)$. The solution is

$$W_{diss} = \frac{(1+\sigma)^2 \kappa \alpha^2 T}{\sqrt{2\pi} C^2 \rho^2 (w_0/\sqrt{2})^3} F_0^2 \tag{2.21}$$

Leading to

$$S(\omega) = \frac{16 k T^2 (1+\sigma)^2 \kappa \alpha^2}{\sqrt{2\pi} C^2 \rho^2 (w_0)^3 \omega^2} \tag{2.22}$$

Liu and Thorne also provide a finite test mass correction to the above noise spectrum. However, most of the noise contribution comes from material located within a "heat diffusion length" from the surface of the mirror. This length depends on material properties and time scale/frequency offset. Temperature fluctuations occurring at greater distances do not propagate to the surface in time to significantly affect the noise. The heat diffusion length is given by:

$$a\sqrt{t} = \sqrt{\frac{2\pi\kappa}{\rho C \omega}}. \tag{2.23}$$

For noise at 1 Hz in fused silica, the heat diffusion length is approximately 1 mm, which is smaller than the mirrors used in this work. Therefore, the finite mirror corrections are unnecessary for our purposes. However, the adiabatic limit overestimates the noise at short time scales, i.e. frequencies less than ω_c.

Cerdonio, et al. derived an expression valid at all frequencies and spot sizes [53], which was later corrected by Black et al for a missing factor of $1/\pi$ [54]. In the more general form, the displacement noise power spectral density is:

$$S_x(\omega) = \frac{4}{\sqrt{\pi}} \frac{\alpha^2(1+\sigma)^2}{\kappa} k_B T^2 w_0 J(\Omega), \tag{2.24}$$

where $J(\Omega)$ is a dimensionless integral:

$$J(\Omega) = \frac{\sqrt(2)}{\pi^{3/2}} \int_0^\infty du \int_{-\infty}^\infty dv \frac{u^3 e^{-u^2/2}}{(u^2+v^2)[(u^2+v^2)^2+\Omega^2]}. \tag{2.25}$$

The dimensionless frequency ω_c is defined as

$$\Omega = \omega/\omega_c, \tag{2.26}$$

where ω is the (angular) measurement frequency.

2.4 Coating Thermo-Optic Noise

The coating thermo-optic noise arises from the coating thermal fluctuations observed by the Gaussian beam profile of the light resonating in the cavity:

$$S_{T0}^{\Delta T} = \frac{2\sqrt{2} k_B T^2}{\pi \omega_0^2 \sqrt{\kappa C 2\pi f}}, \tag{2.27}$$

where κ is thermal conductivity and C is heat capacity per volume. These thermal fluctuations induce length changes in the cavity observed by the light, which cause a phase shift on the light reflected off of the cavity mirrors. To my knowledge, prior to Evans et al. in 2008 [55], thermo-refractive and thermo-elastic noise sources in the coatings were treated as independent terms, but this is a problem as it can lead to an overestimate of the noise. As the coating material expands due to a temperature change (thermo-elastic), the effective index will cause an apparent length decrease from the perspective of the Gaussian beam (thermo-refractive). When the two are considered together, the thermo-optic noise is less than the independent treatment of the thermo-refractive and thermo-elastic noise. The spectral density of this thermo-optic noise can be expressed like this:

$$S_{T0}^{\Delta z} = S_{T0}^{\Delta T} \left(\bar{\alpha_c} d - \bar{\beta} \lambda - \bar{\alpha}_s d \frac{C_c}{C_s} \right)^2 , \tag{2.28}$$

where $\bar{\alpha_c}$ is the effective coefficient of thermal expansions of the coating, d is the coating thickness, $\bar{\beta}$ is the effective thermorefractive coefficient, λ is the wavelength, $\bar{\alpha_s}$ is the effective coefficent of thermal expansions of the substrate, and C_c and C_s are the heat capacities per volume of the coating and substrate. The analytical solutions for the coating thermo-optic noise are complex, especially if the assumption that the thermal diffusion length is much smaller than the coating thickness is not valid, which complicates the heat diffusion equation and requires several lines of equations to solve. Instead of duplicating these results here, we will refer you to Evans et al. [55].

2.5 Thermal Noise Calculations

The portable Yb cavity needed to fit into a very compact space while still providing excellent stability. The required metric was fractional frequency instability better than 1×10^{-15}. With compact cavities, coating noise can represent a significant fraction of the total thermal noise. There are a couple of ways to reduce this noise. One is to increase the spot size on the mirror, which effectively increases the area over which the noise is averaged. The other is to use specialty mirrors with small loss angles, such as crystalline coating. Fig. 2.2 shows the fractional frequency instability estimate for a Yb-like cavity vs cavity length for different design choices. Utilizing large ROC mirrors and crystalline coatings means that the cavity can be short (25 mm was the design choice) while still providing the required stability.

For each cavity, the spacer Brownian noise was calculated using COMSOL. For the Yb cavity, which uses a backing ring to reduce the temperature sensitivity of the cavity, all of the Brownian terms were calculated in COMSOL. The other noise terms were calculated from analytical solutions. A summary of the calculated cavity thermal noise limit and individual terms can be found in

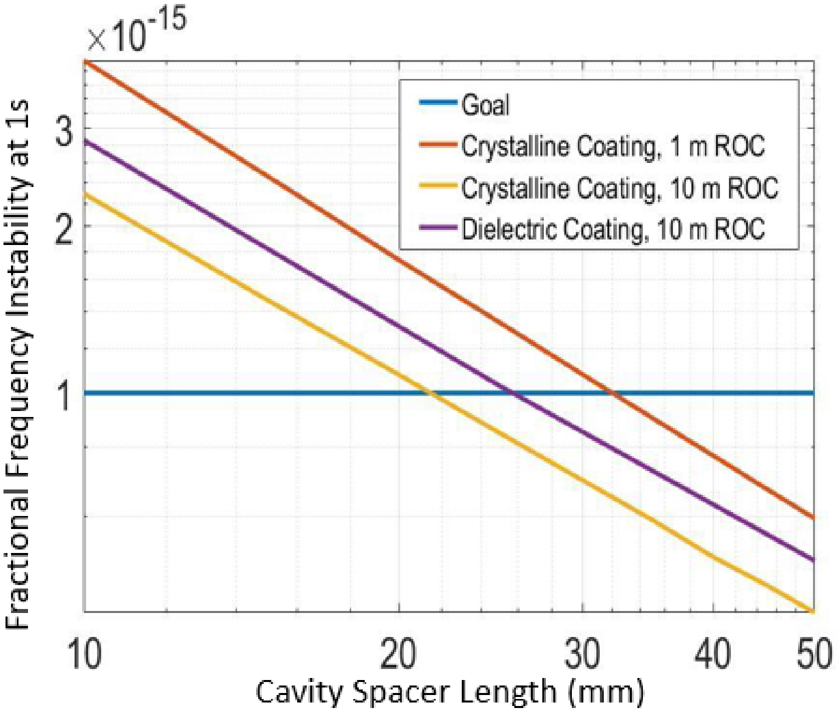

Figure 2.2: Fractional frequency noise at 1s vs cavity length for a Yb-like cavity. By using crystalline coatings and large ROC substrates, higher performance can be fit into a compact cavity.

Name	**Yb**	**FS-ULE**	**ULE - ULE**	**Units**
Spacer Brownian (1 Hz)	0.0062	0.39	0.39	Hz^2/Hz
Substrate Brownian (1 Hz)	0.012	0.22	4.0	Hz^2/Hz
Coating Brownian (1 Hz)	0.0049	2.9	5.6	Hz^2/Hz
Backing Ring Brownian (1 Hz)	0.0026	N/A	N/A	Hz^2/Hz
Substrate Thermoelastic (1 Hz)	0.00060	0.25	0*	Hz^2/Hz
Coating Thermo-optic (1 Hz)	0.0020	0.069	0.068	Hz^2/Hz
1 s ADEV	9.5×10^{-16}	1.1×10^{-14}	1.93×10^{-14}	Hz/Hz

Table 2.1: Noise calculations for the different cavities. The spacer Brownian calculation includes strain energy calculated in COMSOL. The Brownian noise terms for the Yb Cavity all come from COMSOL as well (we used no analytical models for backing rings, but one could be made). All other values come from analytical solutions. The reason the thermoelastic noise is 0 for the ULE-ULE mirror is that the CTE of ULE is very small near any of the temperatures we would typically operate this cavity. This term in no significant in the total noise calculation.

Table 2.1.

Chapter 3

Laser Locking

In order to lock the laser to the cavity, we must take a signal from the cavity and use it to send feedback to the laser. An intuitive answer to this problem might be to lock the laser frequency to a photodetector that observes the transmitted light through the cavity when the laser is on resonance. One potential problem here though is that it is difficult to lock the laser to the peak of the transmission because it can be hard to infer the sign of the laser frequency when it moves off resonance. If the laser frequency goes up or down, the amount of transmission will decrease. One could dither the laser (modulate the laser frequency) and lock to the side of the transmission peak, but this method will strongly couple changes in laser power with changes in the laser frequency.

A better technique for stabilizing the laser frequency is the Pound-Drever-Hall method [56]. This method takes advantage of the anti-symmetric phase of the light reflected from the cavity near resonance. See Fig. 3.1 for a basic schematic of the PDH technique. In order to detect this phase, sidebands are applied to the laser that probes the cavity, typically with an EOM. These EOM sidebands are always reflected when the carrier is on the cavity resonance. Using a circulator before the optical cavity, the reflected light is collected onto a photodetector. The signal at this photodetector is mixed with a microwave signal at the same frequency as the EOM sidebands and an error signal is extracted. A really nice break down of this technique was written by Black [57], and much of the information found in this section has been reproduced from this paper.

Oftentimes, we find the the thermal-noise limited linewidth of a cavity stabilized laser is much smaller than the natural linewidth of the optical cavity. For example, if you consider the

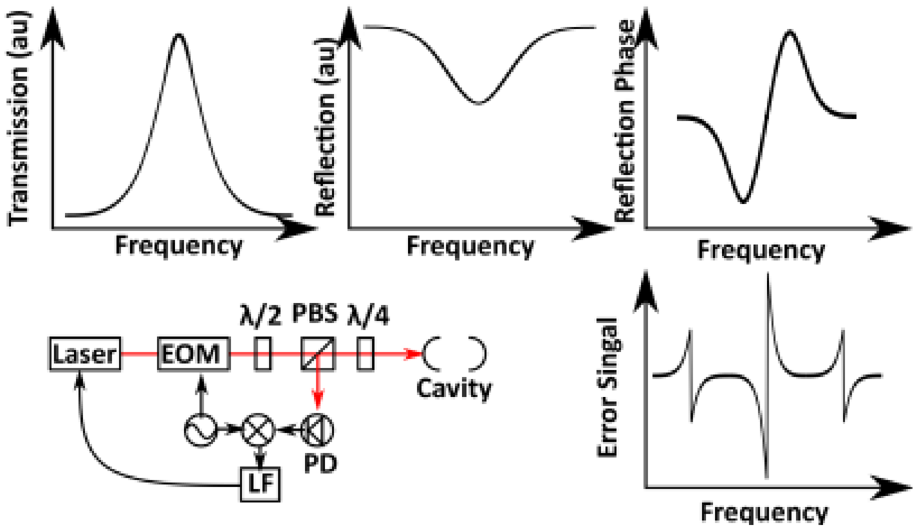
Transmission (au)
Frequency
Reflection (au)
Frequency
Reflection Phase
Frequency
λ/2
PBS
λ/4
Laser
EOM
Cavity
PD
LF
Error Singal
Frequency

Figure 3.1: Top row: the cavity transmission, reflection dip, and reflection phase as the laser is swept through the cavity resonance. Lower left: basic PDH scheme. Laser light is sent through an elector-optic modulator (EOM) where sidebands are applied. A circulator is used to collect the reflected light on a photodetector (PD). This signal is mixed with the same frequency applied to the EOM to create the error signal (shown on the bottom right). This error signal is supplied to a loop filter (LF) or servo, which sends feedback to the laser.

FS-ULE cavity described in Chapter 4, the linewidth of the resonance, given by $\Delta\nu = FSR/F$, where FSR is the free-spectral range of the optical cavity and F is the finesse of the optical cavity, is ≈40 kHz. At the cavity thermal noise limit, the fractional frequency stability of a laser locked to the cavity resonance is $\approx 2 \times 10^{-14}$, which corresponds to a linewidth of a few Hz. We must be able to split the linewidth of the cavity 40,000 times. To achieve this goal we need to suppress any electronic noise that would prevent us from reaching the thermal noise limit. This is achieved through a careful optimization of the PDH discriminator slope, D, which is the slope of the error signal (V/Hz):

$$V_{PDH}(\delta F) = D\delta f \tag{3.1}$$

$$D = \frac{-8\sqrt{P_s P_c}}{\Delta\nu}(\epsilon(1-\xi)) \tag{3.2}$$

P_s is the optical power in the sidebands, P_c is the optical power in the carrier, $\Delta\nu$ is the cavity linewidth, ϵ is a mode-matching parameter describing the optical power coupled into the cavity due to a difference in the spatial profile of the input light and the mode in the cavity, and ξ is the vacuum impedance-matching term related to the loss and transmission of the mirrors [58, 59]. A few things can be observed from this expression. One is that, with careful thinking, the discriminator slope is optimized when the $P_s = 0.5P_c$ (see Eric Black paper for full discussion) [57].

The mode matching term, ϵ, is optimized when the input beam has perfect spatial overlap with the resonant mode in the cavity. The spatial modes of an optical cavity with two spherical mirrors (or one spherical and one flat) are Hermite-Gaussian modes. The TEM$_{00}$ mode is a convenient shape for mode matching and is typically used, although the thermal noise limit of the higher order modes can be smaller due to their larger spatial profile (the thermal noise is averaged over a larger area in this case). To find the spot size of the cavity, we use Gaussian beam equations.

$$R(z) = z[1 + (\frac{Z_R}{Z})^2] \tag{3.3}$$

For a cavity with two curved mirrors and equal radius of curvature (ROC), $R(L/2) = ROC$, where L is the cavity length. This can be used to solve for the Rayleigh range. From there, we can calculate the spot size at the center of the cavity, ω_0.

$$z_R = \frac{\pi \omega_0^2 n}{\lambda} \tag{3.4}$$

From here, it is possible to select the required collimators and lenses to optimize the spatial coupling into the optical cavity.

Even with perfect spatial mode matching, a fraction of the input light on resonance will be reflected due to the loss and transmission of the mirrors, which is described by the vacuum-impedance matching term, ξ,

$$\xi \approx 1 - \frac{T}{T + l}, \tag{3.5}$$

where l is the loss of the mirrors, including both absorption and scattering losses, and T is the mirror transmission. In this expression we assume equal loss and transmission in the cavity mirrors so $T_1 = T_2 = T$ and $l_1 = l_2 = l$. When $\xi = 0$ the cavity is critically coupled, when $0 < \xi \leq 1$ the cavity is under-coupled, and $-1 \leq \xi < 0$ when the cavity is over-coupled.

The finesse of the cavity depends on the loss and transmission of the mirrors and is related to an important term in the discriminator slope, the cavity linewidth [60].

$$F = \frac{\pi}{T + l} = \frac{FSR}{\Delta\nu} \tag{3.6}$$

The discriminator slope and finesse are both inversely proportional to ν, which means that high finesse cavities are important to good locks. This implies that we would like T to be very near 0, but there is a little extra nuance here. Using this relationship and the approximation for ξ, the discriminator slope can be re-written such that:

$$D \propto \frac{T}{(T + L)^2}. \tag{3.7}$$

This is expression is proportional to the cavity gain,

$$G = \frac{4T}{(T + L)^2}. \tag{3.8}$$

The gain in the cavity looks similar to the electronic impedance matching that many are familiar with where the power dissipated in a load resistor is maximized when it set equal to the resistance of the of the source:

$$P_L = V_s^2 \frac{R_L}{(R_s + R_L)^2}. \tag{3.9}$$

This expression implies for a fixed loss, l, that the best discriminator slope occurs when $T = l$ and the intracavity power is optimized, and not when $T = 0$.

3.1 Evaluating a PDH Lock

The most direct assessment of laser frequency or phase noise is an "out-of-loop" measurement, where the light is directly compared (heterodyned) with a quieter reference or (several references and cross-correlated). However, during the setup of a new cavity system, it is advantageous to conduct several "in-loop" noise measurements to determine if further optimization of the discriminator slope or parts with lower noise are required to achieve the desired noise performance. These "in-loop" measurements can help identify and eliminate technical noise sources such as:

- RAM, residual amplitude noise. The EOM is primarily a phase modulator, but it also causes amplitude modulation. This residual amplitude modulation causes the error signal to shift up and down, which changes the frequency lock point. RAM can occur due to polarization noise at the input of the EOM, temperature-dependent birefingence in the EOM, and etalon effects from reflective surfaces in the system (other than the optical cavity) [61].

- Excess electronic noise (from the photodetector, loop filter, amplifiers, mixers, etc.). The voltage noise of the electronic components is typically dominated by the transimpedance amplifier in the photodetector.

RAM and excess electronic noise have a direct impact on the PDH lock. Optimizing the discriminator slope is instrumental in suppressing the laser's inherent noise, the excess electronic noise, and the RAM, all of which manifest in the "in-loop" measurements when the loop filter is locked (on resonance) and unlocked (far from cavity resonance). These "in-loop" measurements are measurements of the electronic error signal sent to the loop filter. To convert the voltage noise to expected frequency noise we use the measured discriminator slope of the cavity. The discriminator slope only applies within the linewidth of the cavity, which is typically less than frequency offset range of interest. We will need a frequency dependent form of the discriminator slope:

$$k(f) = \frac{k_0}{\sqrt{1 + 4\left(\frac{f}{\Delta\nu_{FWHM}}\right)^2}} \tag{3.10}$$

Where k_0 the slope of the error signal in [V/Hz], and $\Delta\nu_{FWHM}$ is the full width at half maximum cavity linewidth [62, 59]. Now we can use the error signal to get a phase noise estimate using a few simple steps.

(1) Measure the PSD of the error signal. This will be voltage noise and have units of $\mathrm{dBV}^2_{rms}/\mathrm{Hz}$.

(2) Find the the discriminator slope, k_0 [V/Hz] using an oscilloscope.

(3) Divide by the k function squared or subtract $20\log(\mathrm{k(f)}^2)$. You now have the voltage noise in $\mathrm{dBHz}^2/\mathrm{Hz}$.

(4) To get to phase noise, divide by f^2 or subtract $20\log(\mathrm{f})$. Now you should have $\mathrm{dBrad}^2/\mathrm{Hz}$.

(5) For dBc/Hz, subtract 3 dB.

The locked “in-loop” noise measurement will indicate if there is sufficient gain in the loop to suppress the free running laser noise to the required level. To get the desired noise, sometimes all that is needed is an adjustment to the loop filter setting, but other times the problem is more fundamental, such as a quieter starting laser is needed or high bandwidth frequency actuators are required. I have seen more than 90 dB suppression of free-running laser noise in the lab (see Chapter 5), but there are limits and a pre-stabilization step can help if the laser is particularly noisy or the goal is particularly low noise. Faster actuators can be used to suppress the noise higher offset frequencies. In Chapter 4, I used fast actuators to improve the cavity noise at 10 kHz to state-of-the-art levels despite the cavities compact size. Typically, the performance goal is that the in-loop noise measurements are below the thermal noise limit of the cavity, but the requirements will be set by the application.

Occasionally, the “in-loop” locked noise may appear lower than the unlocked “in-loop” noise, but the actual out-of-loop noise level will always be higher than the unlocked in-loop level. This is attributed to the loop filter effectively imposing the inverse of the photodetector noise onto the light.

The “unlocked” in-loop noise level serves to identify the electronic noise and RAM contributions to phase noise. RAM typically becomes noticeable at low offset levels (typically below 100 Hz) and can be separately identified by shutting off the microwave signal to the EOM (Electro-Optic Modulator) temporarily. Performing an in-loop unlocked measurement while the laser light is off can help discern between noise written on the light and noise directly from the detector or electronics.

There is also another source of noise to consider, RIN, relative intensity noise. Even with the PDH technique, fluctuations in laser intensity can still couple to the frequency noise of the locked laser if the cavity length changes with intensity. Some of the coating loss is from absorption which produces heat and causes index changes and length changes in the mirror coatings. RIN can be mitigated through a distinct feedback loop, separate from the PDH loop, which, unless the laser has a lot of intensity noise or the noise requirements of the system are particularly low, can be fairly easy to set up. There is no phase detection in this case, just a photodetector, a loop filter (servo), and an intensity actuator are required. RIN can be measured by looking at the voltage noise on a detector placed before the optical circulator in the PDH loop. To calibrate this signal’s impact on phase noise of the locked laser, sometimes it is helpful to place a pilot tone on the light by intensity modulating the light at a frequency that goes to the cavity and searching for a response on the locked laser phase noise at that frequency.

Typically, the laser RIN has not contributed to the phase noise of lasers locked to the cavities in this work. This is in part due to the choice of lasers (which have relatively little RIN) and the thermal noise limits of the cavities involved in this work (which are high compared to the state-of-the-art, but sufficient for our purposes). However, we have used RIN feedback loops to keep the intracavity power constant during an acceleration-sensitive flip test. During these tests, the optical bread board can flex substantially and change the spatial coupling of light into the cavity. By using the transmitted light detector and sending feedback to the microwave power sent to an AOM, the optical power in the cavity can be held constant even as the coupling changes.

Chapter 4

FS-ULE and ULE-ULE cavities

4.1 Introduction

Here I present a simple, rigidly held cylindrical vacuum-gap FP cavity, called the FS-ULE cavity or the primary cavity in this chapter, reaching a fractional frequency stability of 2×10^{-14}, capable of supporting applications in low phase noise microwave generation via optical frequency division (OFD)[35, 23], distributed optical fiber sensing [63, 64, 65], and mobile optical clocks [33]. The cavity is composed of fused silica (FS) mirrors and an ultralow expansion (ULE) glass spacer which is only 6.3 mm long. The cavity volume is 5.2 mL. A laser locked to the cavity operates at the cavity thermal noise limit for noise offset frequencies ranging from $\sim$ 1 Hz to $\sim$ 10 kHz. To our knowledge, the phase noise level at 10 kHz, at approximately -108 dBc/Hz on the optical carrier, is one of the lowest reported for any vacuum-gap FP [66, 1], or dielectric resonator [67, 68]. If paired with an optical frequency comb, the laser system can support state-of-the-art microwave phase noise that is comparable to the lowest phase noise achieved to date for offset frequencies above $\sim$ 100 Hz. Measurements of the cavity's low sensitivity to holding force indicate the cavity may be reliably held on its end faces, which can be found in Chapter 7. Though other groups have simulated and studied its impact [69, 70, 4, 3], these are the first direct measurements of holding force sensitivity of which we are aware. Additionally, the cavity acceleration sensitivity for three mechanical axes was measured to be $5 \times 10^{-11} g^{-1}$, $3 \times 10^{-10} g^{-1}$, and $6 \times 10^{-10} g^{-1}$ (see Chapter 7 for more details on this measurement). A variation on our design, called the ULE-ULE cavity, also allowed us to explore trade-offs in holding force sensitivity, noise, and long-term stability for a cavity composed only of ULE and larger diameter mirrors.

4.2 Cavity Design

Compact and portable FP reference cavity designs must balance noise performance, temperature sensitivity, acceleration sensitivity, tolerance to mirror misalignment [4], sensitivity to changes in the holding force, and manufacturability. We have chosen a simple cylindrical geometry for ease of manufacture and its high degree of mechanical symmetry (see Fig. 4.1). Mechanical symmetry is important for maintaining low acceleration sensitivity, and has been exploited in many compact cavity geometries, including cubes [3], spheres [4], pyramids [37], and other compact cylinders [1]. The ULE spacer material is chosen for its low thermal expansion and measures 27 mm in diameter and 6.3 mm in length. The spacer has a single vent hole with a diameter of 3 mm for evacuating the cavity. The mirror substrates are FS with a diameter of 12.7 mm and a standard thickness of 6.35 mm. Both mirrors have a radius of curvature (ROC) of 1 m with a flat outer contact annulus for optical contact bonding to the spacer. The total cavity volume is only 5.2 mL. The mirrors were manufactured and polished in the same batch, leading to nearly equal optical contact areas. As we show below, the asymmetry introduced by the single vent hole increases the acceleration sensitivity of the cavity.

The mirror material was chosen by considering the thermal noise and temperature sensitivity. Fused silica has a higher mechanical quality factor than ULE, and results in lower thermal noise [49]. For the lowest temperature sensitivity, the cavity should be operated at its zero-crossing temperature (T_{zc}), where the linear coefficient of thermal expansion (CTE) passes through zero [71]. The T_{zc} of ULE is typically near room temperature. However, employing FS mirrors shifts the T_{zc} of the cavity to well below room temperature due to distortions of the mirror shape caused by the comparatively large radial expansion of the mirrors [72]. This effect is particularly important for short FP cavities, where the mirror distortions are a larger fraction of the cavity length. To counteract this effect, ULE backing rings [72] can be used to shift the cavity T_{zc} back to a convenient temperature, but it is not always possible to fully compensate the large T_{zc} shift of compact cavities

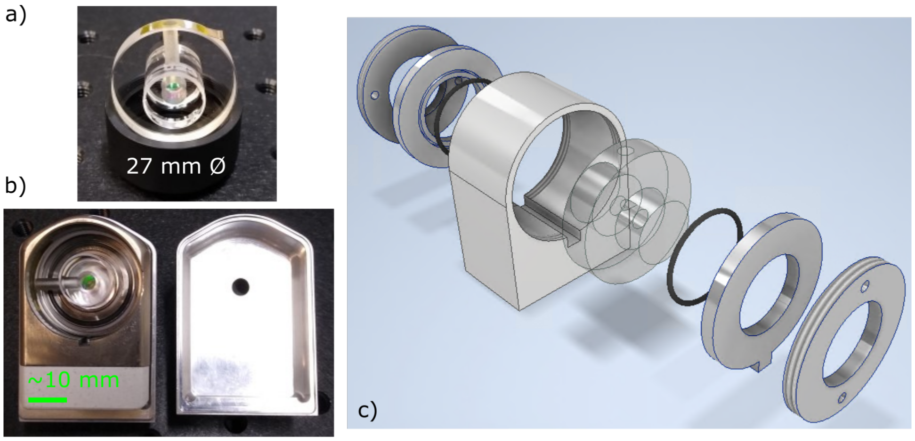

Figure 4.1: a) Photograph of the optical cavity, which is 27 mm in diameter. The spacer is 6.3 mm thick and the mirrors are 12.7 mm in diameter and 6.35 mm thick. b) Photograph of the optical cavity in its mounting structure. The mounting structure sits on top of a Macor spacer and is placed inside of a heat shield, also pictured. c) Exploded cartoon view of the holding structure. The cavity is suspended in the Invar mounting structure by two Viton o-rings. These o-rings are held in place by two Invar holders. Note the notch on the holder that prevents the o-ring from rotating when the structure is assembled. Finally, threaded retaining rings are applied to rigidly hold the cavity in place.

in this way. High T_{zc} ULE [39] can also be used but is not typically specified to the required precision for a repeatable compact cavity manufacturing process. Here, using a ULE spacer with unknown T_{zc}, we designed our system to rely on temperature stabilization and shielding of the cavity enclosure. This was driven by our targeted application of low noise microwave generation and undersea fiber optic cable measurements, where short-term phase and frequency fluctuations are of greater concern than long-term cavity length drift.

The 1 m ROC of the mirrors was chosen to maximize the optical spot size on the mirrors, w, while maintaining reasonable tolerance to mirror misalignment. For an optical cavity whose thermal noise is dominated by Brownian noise in the coatings (as is the case here), the phase noise power scales as $1/w^2$ [45], and for cavities where the ROC is much larger than the cavity length (L), w^2 is proportional to $\sqrt{\mathrm{ROC}}$. However, the larger ROC results in a larger optical axis displacement due to a mirror tilt or displacement, and the shift in the optical axis away from the cavity mechanical axis increases the effective acceleration sensitivity of the cavity [73]. Again assuming ROC $\gg L$, the beam displacement on the mirror surfaces d is given by $d \approx 0.5 \times \mathrm{ROC} \times \theta$, where θ is the mirror tilt angle [74]. The residual angle between the faces of our spacer is < 50 μrad, leading to a maximum beam displacement near 25 μm. Furthermore, sag in the mirror surface for large ROC mirrors is extremely small when the mirror diameter is small. For example, the sag at the center of a 12.7 mm diameter mirror with 1 m ROC is only ~ 20 μm. This makes creating a contact annulus with the required roughness and surface figure without spoiling the smoothness of the center of the mirror extremely difficult. Indeed, the largest ROC we could obtain on 12.7 mm diameter mirrors with an annulus for optical contact bonding was 1 m.

The cavity's rigid holding structure was designed to minimize the effect of holding force variation on cavity length, shown in Fig. 4.1. We used finite element analysis (FEA) software to design a holding geometry that can provide first-order insensitivity to the holding force (see Chapter 7 for more details). Given the short length of our cavity spacer, the cavity is held on the spacer end faces with Viton o-rings. The o-rings are held against the cavity with a backing plate, behind which is a threaded piece that screws into a holding mount. The backing plates and holding mount are made of low expansion Invar to minimize temperature changes of the holding structure from coupling to changes to the cavity holding force. The base of the holding mount is composed of Macor to reduce the thermal conductivity from the outer vacuum enclosure. Additionally, a polished aluminum heat shield is placed around the cavity and holding structure to reduce the radiative heat transfer to the cavity. The volume enclosed by the heat shield is $\sim$40 mL.

4.3 Laser Locking

The laser frequency was locked to the cavity with the Pound-Drever-Hall (PDH) technique [57], as shown in Fig. 4.2. Cavity ring-down measurements yielded a finesse of 600,000, providing a steep discriminator slope for laser locking. We employed a broadband locking scheme utilizing feedback to an electro-optic modulator (EOM) to achieve nearly cavity thermal noise-limited performance over a broad offset frequency range [75, 76, 66]. Light from a 1550 nm commercial fiber laser was routed through a fiber-coupled acousto-optic modulator (AOM) frequency shifter, followed by a fiber-coupled EOM and a 90/10 fiber coupler, then was launched into free space to interrogate the cavity. A free-space circulator directs light reflected from the cavity to a photodetector used for PDH frequency stabilization. A separate photodetector placed at the back end of the cavity was used to stabilize the intracavity power, though during normal operation it is not needed as it was determined that our laser's intensity noise does not contribute to the measured phase noise. Laser frequency stabilization to the cavity was implemented through three feedback paths: a piezoelectric transducer controlling the laser cavity length was used for low bandwidth/large dynamic range frequency corrections, the AOM was used for mid-bandwidth (to few 100 kHz) feedback, and the EOM was used for high bandwidth (up to 1 MHz) feedback. The same EOM was also used to impart 50 MHz phase modulation sidebands on the laser light for the PDH error signal generation. The optical power impinging on the cavity was $\sim$ 600 μW, leaving greater than 10 mW of frequency-stabilized output from the 90/10 coupler. Since we use a single EOM for both PDH phase modulation and feedback control, the stabilized light output had 50 MHz sidebands. These sidebands are outside the bandwidth of any frequency comb lock, and is not anticipated to impede

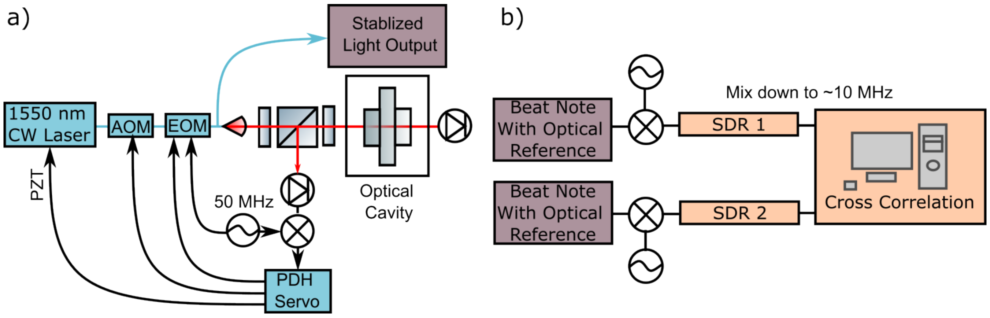
a)
Stablized Light Output
1550 nm CW Laser
AOM
EOM
Optical Cavity
50 MHz
PZT
PDH Servo
b)
Beat Note With Optical Reference
Beat Note With Optical Reference
Mix down to ~10 MHz
SDR 1
SDR 2
Cross Correlation

Figure 4.2: a) Simplified block diagram of the optical cavity system. A 1550 nm laser is sent through a fiberized AOM then EOM. The light is then split in fiber. Some of the stabilized light is sent to the optical cavity. The 1550 nm laser is stabilized to the optical cavity resonance using feedback to the laser PZT, AOM, and EOM. A frequency diplexer (not shown) is used at the radio frequency (rf) input of the EOM so that the EOM can be used for both the PDH sideband generation (at 50 MHz) and feedback control. The transmission detector can provide a relative intensity noise (RIN) servo error signal, but is only utilized during flip tests to stabilize the intracavity power because the alignment is affected by the optical breadboard flexing. b) Stabilized laser light is sent on to be compared to two different optical references. One is another cavity-stabilized laser at 1550 nm. The other is a comb that is frequency-referenced to a cavity-stabilized 1156 nm laser [13]. Software defined radio (SDR) is used to track the phase of the signals, which are then cross-correlated to remove uncommon noise in the frequency combs and beat note detection.

any applications using a comb. If stabilized light without PDH sidebands is desired, PDH phase modulation and feedback control can be separated by using two EOMs. The extremely low noise at 10 kHz offset is enabled by the feedback bandwidth, high finesse of the cavity, and relatively high optical power on the cavity.

To measure the laser phase noise, the stabilized laser output was split and heterodyned against two separate ultrastable optical frequency references. The heterodyne beat notes were simultaneously digitally sampled by software defined radio (SDR), and the phase fluctuations were extracted [77]. The phase noise cross-spectrum was then obtained by averaging the complex product of the Fourier transforms of the individual phase records [1]. This allowed us to reject the noise of the optical phase references and proved to be particularly important to reveal the low phase noise of our system for offset frequencies > 1 kHz.

4.4 Phase Noise and Fractional Frequency Stability

Phase noise of the cavity-stabilized laser, the predicted cavity thermal noise limit, and the laser's free-running noise, are shown in Fig. 4.3. The integrated timing jitter from 1 MHz to 1.3 Hz is 12 fs. The laser phase noise closely follows the cavity thermal noise for offset frequencies between 1 Hz and 10 kHz. The predicted thermal noise is calculated using FEA software [48] and includes Brownian noise of the spacer, mirror coatings, and mirror substrates, as well as thermoelastic noise of the substrates and spacer. Only the Brownian noise of our small spacer differed significantly from simple analytic models. Thermo-optic noise was calculated analytically [78, 79, 2], but did not make a substantial contribution to the total thermal noise. The effect of residual amplitude modulation (RAM) on the frequency stability is captured by the in-loop PDH error signal when the feedback control is not engaged [80], and was determined to be below the measured noise level at all offset frequencies for the phase noise. Likewise, RAM contributions to the fractional frequency stability measurement (discussed below) were also negligible. Broadband noise reduction of the free-running laser noise was realized using feedback to the EOM, resulting in a gain bandwidth > 1 MHz. At 10 kHz offset, this large feedback bandwidth provides > 60 dB suppression of the

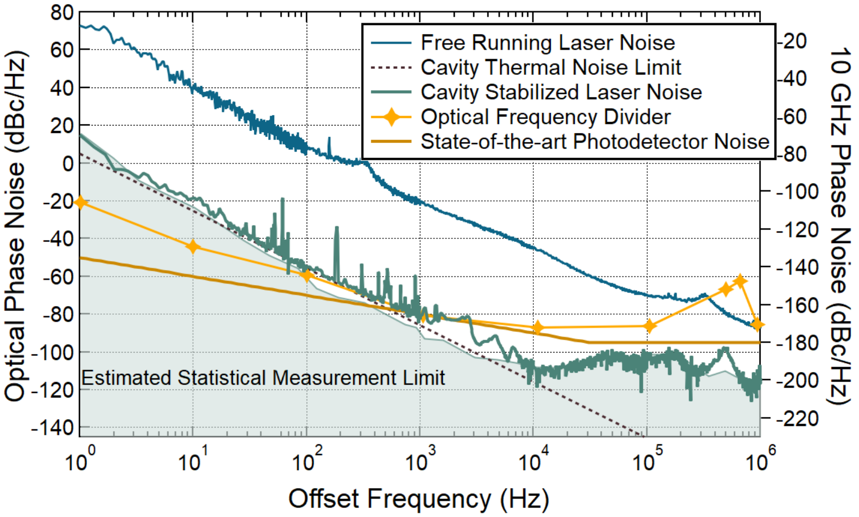

Figure 4.3: Measured phase noise of the free-running commercial laser in blue, cavity-stabilized laser phase noise in green, the cavity thermal noise limit in black, an optical frequency divider in gold [23], and state-of-the-art photodetector phase noise at 10 GHz in brown [24]. The shaded region is an estimation of the statistical measurement limit of the cross-spectrum measurement of the cavity-stabilized laser phase noise given the single channel measurement levels [25]. The number of averages for each frequency offset band are: f < 100 Hz; 13 averages, 100 Hz < f < kHz; 125 averages, 1 kHz < f < 10 kHz; 1257 averages, 10 kHz < f < 1 MHz; 7954 averages. Note that the noise of the cavity-stabilized laser stays near the thermal noise limit to ∼ 10 kHz offset. Because the phase noise of the cavity-locked laser above 1 kHz offset frequency is at or below a state-of-the-art photodetector level, this cavity can serve as a compact, low-noise reference for OFD microwave generation.

free-running laser noise. To our knowledge, the measured phase noise level at 10 kHz is one of the lowest reported for any vacuum-gap FP (despite the cavity's small size) [66, 1] or dielectric resonator [67, 68] .

When coupled with an optical frequency comb, this cavity can support low-noise microwave generation through OFD [35]. The phase noise contribution of our cavity on a 10 GHz carrier is shown on the right axis of Fig. 4.3. For comparison, the phase noise of a state-of-the-art 10 GHz photodetector [24], and one of the lowest noise OFD systems demonstrated to date are also shown [23]. Importantly, our compact cavity can support microwaves comparable to that of the lowest noise OFD signals produced yet-to-date for offset frequencies greater than ∼100 Hz. Above ∼1 kHz, the microwave noise contribution from the cavity is below that of the projected photodetector noise, and thus will not adversely impact the signal. Above 10 kHz offset frequencies, the cavity supports 10 GHz phase noise below -180 dBc/Hz. Of course, the residual noise of the optical frequency comb will also contribute to the final microwave phase noise; however, these results show that an extremely compact cavity can enable microwave signals whose noise is competitive with those systems that are referenced to much larger-size optical cavity systems.

Figure 4.4 shows the measured fractional frequency stability of our primary (FS mirrors and ULE spacer) cavity, given in terms of the Allan deviation (ADEV). For comparison, the ADEV of the all-ULE cavity is also shown. The ADEV is calculated using the phase record of the SDR measuring the beat note of our cavities against a comb that is frequency-referenced to a cavity-stabilized 1156 nm laser. For the primary cavity, an external AOM driven by a direct digital synthesizer (DDS) with a linearly chirped frequency correction was used to compensate for the 136 Hz/s linear drift, which is likely due to the CTE of this cavity. A resistive heater is used to stabilize the temperature of the vacuum can around the cavity to better than 0.1 K, but the CTE of this mixed material cavity is $\sim 1 \times 10^{-7} \Delta L/L$ per K. A residual drift of 14 Hz/s remained after compensation, limited by the frequency resolution of the DDS. The fractional frequency stability of the primary cavity (black curve) is near its calculated thermal noise limit (dashed black curve) at 0.1 s averaging time. The slightly larger thermal noise limit of the all-ULE cavity is shown in dashed blue. The ADEV of the all-ULE cavity was measured at both room temperature near 23 °C and at 55 °C, demonstrating the large range of temperatures at which this cavity can operate (our setup did not allow for cooling the cavity below room temperature). At room temperature, the frequency is nearly thermal noise limited from 0.1 s to 1 s with a linear drift of 3 Hz/s. At 55 °C, the frequency stability reaches the calculated thermal noise limit from 0.3 s to 0.8 s, and exhibits a slightly lower drift rate of 2 Hz/s. No T_{zc} was found with this cavity below 55 °C, though we note the ULE used for this spacer is legacy material from previous experiments [71], and its material properties are not well known. Still, despite the higher thermal noise and lack of T_{zc}, the all-ULE design can be a valuable compromise where long term-stability and low drift are desirable.

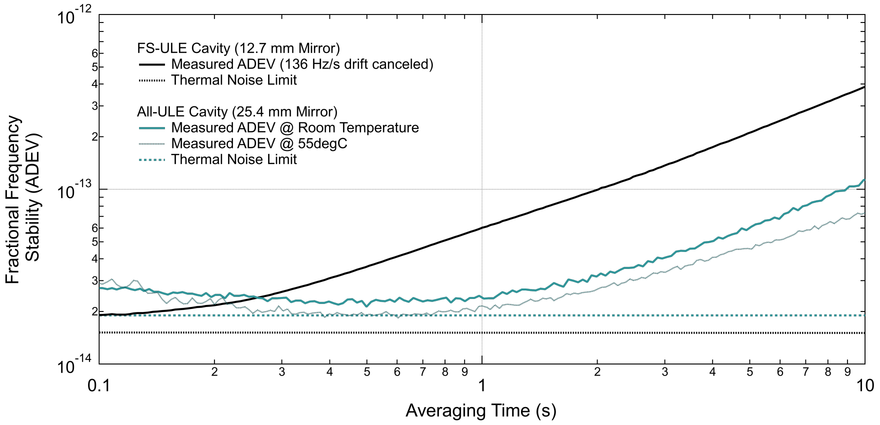

Figure 4.4: Measured fractional frequency stability expressed as an Allan deviation (ADEV) of a laser locked to the primary cavity and the all-ULE cavity. An external AOM was used to compensate for a linear drift of 136 Hz/s on the locked laser. There was a residual drift of 14 Hz/s at the time of the measurement. The all-ULE cavity did not have a drift canceling AOM and the drift rate was substantially lower, 3 Hz/s at room temperature and 2 Hz/s at 55 °C. Note that the all-ULE Cavity is thermal noise limited at 1 s at 55 °C.

Chapter 5

Reference Cavity for a Portable Yb Clock

5.1 Introduction

Microwave oscillators, like quartz and sapphire oscillators, have exceptionally low phase noise but drift with temperature and require external references for long-term stability. Atomic transitions make excellent frequency references since all atoms of a given element are identical, and careful engineering choices can yield frequency selectivity of order 10^{-15} or more while limiting sensitivities to the environment. Microwave clocks using laser-cooled atoms, such as Rb or Cs fountain devices, exhibit frequency stability of about $\sigma_y(\tau) = 10^{-13}/\sqrt{\tau}$ (for an averaging interval τ in seconds) and $\leq 5 \times 10^{-16}$ accuracy [81], while not being transportable or miniturizable. Further, a frequency accuracy (or long-term stability) of $5 \cdot 10^{-15}$ is only sufficient for 1 ns monthly timing performance if operated 100%-continuously and without technical fault—the expected time dispersion $\epsilon_x \approx \sigma_y(\tau) \times \tau = 1.3$ ns at $\tau =$1 month.

Atomic clocks based on optical electronic transitions promise orders of magnitude improvement over microwave clocks, in part due to their much higher oscillation frequency. Laboratory-scale optical atomic clocks have demonstrated $10^{-16}/\sqrt{\tau}$ stability [82, 83] and relative uncertainties near 10^{-18} [84, 85, 86]. While these instruments have already performed new tests of fundamental physics (e.g. dark matter searches [29]), they are often physically large, complicated, and require a team of dedicated scientists to operate. Several applications including very long baseline interferometry (VLBI) telescopes [87], absolute geodesy [84], and navigation [88] can benefit from optical clock performance but are not compatible with the size and complexity of a laboratory-grade optical clock.

There have been a few demonstrations of portable optical clocks to date including $^{40}\mathrm{Ca}^{+}$ [89], and ^{87}Sr optical lattice clocks [90, 91]. Practical, portable optical atomic clocks must balance conflicting demands on stability, size, simplicity, cost, and robustness. For a deployed optical clock, the short-term stability is provided mostly by a laser locked to an optical cavity. For portable optical atomic clocks, the cavity must also be compact and insensitive to the environment. Here we design and build a cavity-stabilized laser system based on a 25 mm long vacuum-gap Fabry-Perot optical cavity, which has been designed to be compatible with a portable Yb clock [92].

In this Chapter, I will present a preliminary measurement of phase noise and stability with this cavity. Final measurements were never conducted due to a number of technical challenges including three separate incidence of contamination of the cavity mirrors and problems with the vacuum system. I describe these challenges, the preliminary results, and next steps so that future grad students may use them as a reference, but this work on this cavity is incomplete at this time and should be treated as preliminary.

5.2 Cavity and System Design

The cavity has a 25 mm long, 50 mm diameter, ultra-low expansion (ULE) glass spacer. The cavity spacer has 4 evenly spaced vacuum vent holes (2 through cross vents) that are 3 mm in diameter. The central bore is 7 mm in diameter with a 1.5 mm chamfer, which prevents the coatings from contacting the spacer. The mirrors are fused silica with crystalline coatings. The mirrors are 25.4 mm in diameter and 6.3 mm long. The coatings are high finesse ($> 300,000$) at 1156 nm, but the exact finesse depends on the specific cavity modes because even in low vacuum (10^{-7} Torr), there is significant water absorption near 1156 nm. Backing rings are contacted to the backside of the mirrors. The backing rings are made from the same ULE as the spacer, which has been designed to have a high-temperature zero-crossing in the CTE, near 45^{o} C. The backing rings are the same diameter as the mirror and are 4.5 mm thick with a 5 mm bore. For more details on the CTE simulations and preliminary results of the portable Yb Cavity, please see section 6.1.

We use a commercially available diode laser with an external cavity design at 1156 nm. It is locked to the portable Yb cavity, as shown in Figure 5.1. The laser light is first isolated using built-in free-space stages before being coupled into a fiber. An Acousto-Optic Modulator (AOM) is included in the fiber path for potential Relative Intensity Noise (RIN) feedback. The light is then split using a fiber splitter, with one output serving as the stabilized light output. Next, the light passes through a fiberized Electro-Optic Modulator (EOM) that generates sidebands for the PDH lock. After the EOM, the light is launched back into free space, passing through an isolator (ISO) and reaching the circulator. The circulator consists of a Faraday-Rotator (FR) and a polarization beam splitter (PBS). This circulator is used so that the light incident on the cavity is linearly polarized. The crystalline mirrors have a birefringence that splits the TEM_{00} spatial mode into two frequencies. In order to couple to just one, linearly polarized light is required. Both transmitted and reflected light are detected.

The reflected light is mixed with the same microwave frequency applied to the EOM. This mixed signal becomes the error signal, which is used for the PDH lock by feeding it into the servo or loop filter. The PDH lock system provides feedback to control both the piezo (PZT) and the current of the diode laser (ECDL), allowing precise stabilization of the laser output.

5.3 Technical Challenges

A number of technical challenges were encountered with this design. I hope that detailing these challenges will be useful to people designing future cavity systems.

The custom-designed aluminum vacuum enclosure for the Yb cavity used a 1.33" CF flange to connect the tee for the ion pump and valve to turbo pump, which limited vacuum conductance from the chamber to the turbo pump and the ion pump. In previous systems, vacuum conductance was not a primary concern and the surface area of our parts was smaller. The combination of the 1.33" CF tee design and the greater system surface area in this system, resulted in a longer turbo pump time (approximately 1 month) and a relatively elevated ion pump vacuum pressure. The higher-than-usual pressure (around 2×10^{-6} Torr, in contrast to the usual low 10^{-7} Torr) could be

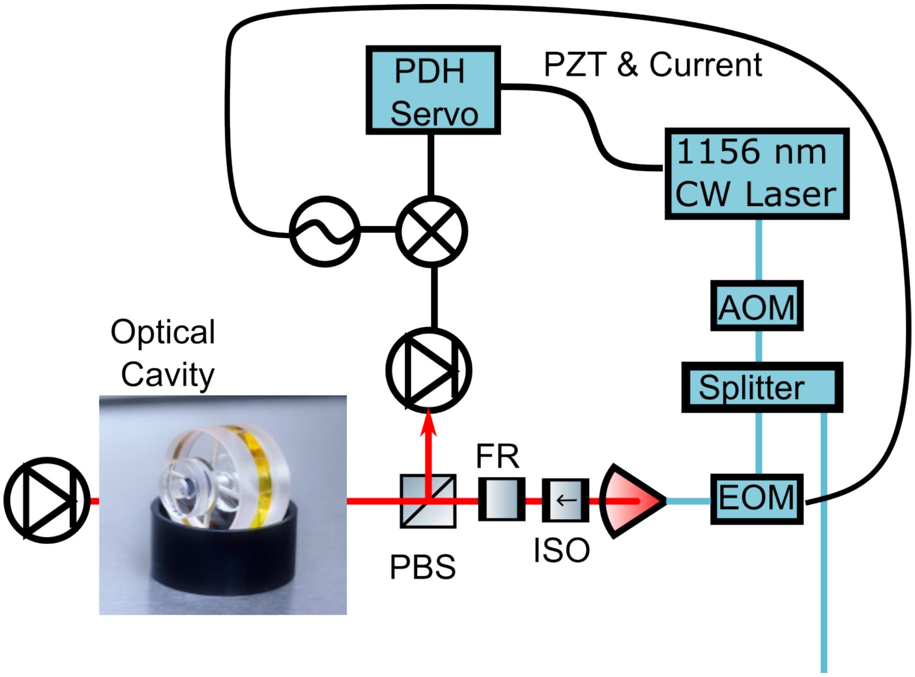

Figure 5.1: A system diagram for the laser locked to the portable Yb cavity. A commercially available 1156 nm external cavity diode laser (Littrow grating design), is used for the lock. The laser is coupled into fiber after two stages of built-in free-space isolation. A fiberized Acousto-Optic Modulator (AOM) is in the path, which is present for RIN feedback if needed. Then a fiber splitter is used to divide the light. One free-port can be used as the stabilized light output or a free space splitter may be used as well. Then the light is sent through a fiberized EOM, which is used to provide the sidebands involved in the PDH lock. After the AOM, the light is launched back into free space, where it passes through an isolator (ISO) before the circulator, which is comprised of a Faraday-Rotator (FR) and a polarization beam splitter (PBS). Transmitted light is detected and so is the reflected light. The reflected light is mixed with the same microwave frequency as is applied to the EOM, and this signal is the error signal provided to the servo or loop filter for the PDH lock. The PDH lock provides feedback to the piezo (PZT) and the current of the ECDL.

a factor behind the ion pump malfunction and subsequent replacement. Ultimately, we substituted the vacuum can with one featuring a 2.75" CF flange port for the pumps.

The original heat shield shields are cylindrical and initially they were attached to the base with large inner threads (similar to a jar). We used methanol and DI water to lubricate the shields during assembly (we wanted to avoid any vacuum grease as it might contaminate the cavity mirrors and be difficult to remove). However, without grease, the large threads ended generating aluminum dust that contaminated the mirrors, which caused us to send the cavity out for cleaning and re-contacting more than once. Ultimately, we replaced the large threads with tiny set screws. This was a technical challenge because the walls of the shields were very thin and there was very little room in the chamber to make adjustments to the design.

After we repaired the shields, the cavity was contaminated again. We do not know the exact cause, but some people working at 1156 nm have speculated that cavities at this wavelength may be more susceptible to contamination due to water absorption near this wavelength. It is not always possible to choose the design wavelength of a cavity, but sometimes an optical comb can be used to transfer the stability of a cavity to another wavelength.

5.4 Preliminary Phase Noise Measurement

The estimated thermal-noise-limited fractional frequency instability for the optical cavity is a little under 1×10^{-15}. The Yb cavity has crystalline mirrors, which have lower coating Brownian noise than dielectric mirrors. This can be particularly advantageous in compact cavities where the coating noise represents a significant contribution to the total cavity noise. Please see Table 2.1 for more detail on the Yb cavity noise. After locking up the cavity, we measured the phase noise, shown in Fig. 5.2. The free-running laser noise is suppressed by more than 90 dB at some offsets. The laser is nearly thermal-noise-limited in the first decade. Between 10 Hz and 100 Hz offset frequency, there is some mysterious additional noise that has yes to be explained but could be coming from the reference. Further measurements are required to sort this out. Above 100 Hz, the in-loop electronic noise is a significant contribution.

The in-loop unlocked noise sits just below the thermal noise limit, which makes improvements to the system challenging. A lower noise photodetector or more optical power on the cavity (which can increase the discriminator slope) could help improve this problem. More optical power can also help improve the discriminator slope. I was typically operating the cavity with 100-500μW, which is considered high. Because of the shape of the in-loop noise near 1 Hz and below (not pictured), I also suspect that RAM is contributing to problems with the long-term stability of the cavity. Careful characterization of laser RIN should also be performed in the future.

5.4.1 Preliminary Allan Deviation Measurement

Preliminary measurements of the fractional frequency instability can be found in Fig. 5.3. These measurements show laser noise far above the estimated thermal noise limit of the optical cavity. Further measurements and analysis will be required. RAM is suspected to be a problem here. These results are not near the thermal noise limit at these times scales are not at present good enough for use with a mobile clock.

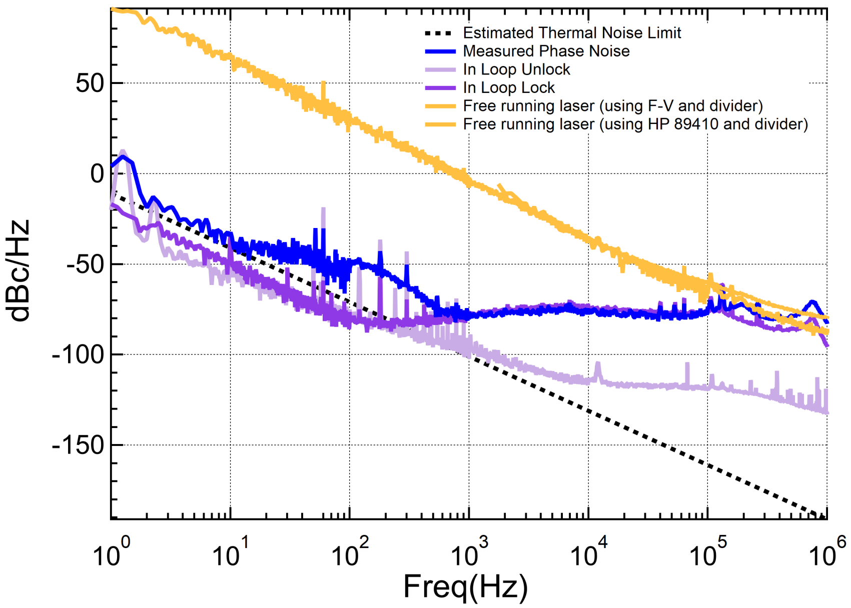

Figure 5.2: Preliminary phase noise measurements of the laser locked to the portable Yb cavity. Free running laser noise is shown in gold: two measurement techniques are required to measure this noise - both a frequency to voltage converter and a vector network signal analyzer was used in this measurement. The in-loop estimations of the electronic noise and random amplitude modulation (RAM) contribution are shown in the two purple traces. The measured out-of-loop phase noise is shown in blue. The estimated thermal noise limit is shown as a dotted black line.

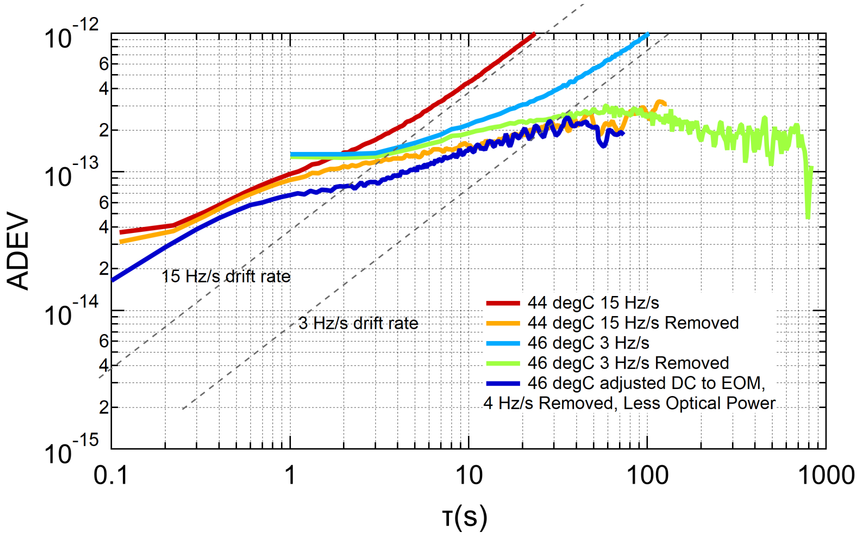

Figure 5.3: A few preliminary fractional frequency instability, ADEV, measurements of the Yb Portable optical cavity. These measurements were taken periodically while trying to find the zero-CTE point of the cavity, which was, unexpectedly, not found below 55°C. These measurements of the ADEV are all significantly above the thermal noise limit. One suspected problem is the RAM, which is contributing even at 1 Hz/1s in the phase noise measurement. An active RAM cancellation lock may make an improvement here.

Chapter 6

Temperature Sensitivity

The long-term stability of the optical cavity is heavily influenced by sensitivity to temperature [71]. The cavity expands and contracts according to its coefficient of thermal expansion (CTE), α, which describes the fractional length change per Kelvin ($\frac{dL}{LdT}$ [1/K]).

For portable cavities, a CTE zero-crossing at a point above room temperature is desirable because it is generally easier to heat a system up than to cool to cryogenic temperatures. Ultra-low expansion glass (ULE) is a material with a CTE zero-crossing near room temperature, but it has worse Brownian noise than materials like fused silica (FS), which has a high CTE near room temperature. In order to get the best of both worlds, some have used mixed material cavities where the spacer is made of a low thermal expansion material and the mirrors are made of a low Brownian noise material. For cavities made of a single material, the CTE of the cavity is the same as the CTE of the material. However, in mixed material cavities, the mismatch in the CTE of the two materials can cause a strain at the mirror-spacer interface with temperature changes. This strain causes the mirror to bow and can influence the effective CTE of the cavity.

The mirror strain caused by CTE mismatch has been described well by Wong et al. and Legero et al. [72, 93]. Here we reproduce some of the relevant equations from their work. The CTE difference in the mirror and spacer results in a temperature-dependent radial expansion:

$$dR = (\alpha_m - \alpha_s)RdT. \tag{6.1}$$

Assuming that the contact between the mirror and spacer is rigid, the thermal expansion of the mirror (which is large relative to the spacer in our specific case) results in a radial mirror stress which causes the mirror to bow along the axial direction. Assuming a linear stress-strain relationship (fused silica is a linear elastic material), the radial expansion dR and the mirror displacement along the axis dB should be connected by a temperature-independent coeffiecent δ such that $dB = \delta dR$. The differential thermal expansion of the whole cavity dL as a function of temperature can be expressed as the spacer's expansion, $L\alpha_s dT$, plus the axial displacement of the mirrors $2dB$. Now, the effective CTE of the cavity, $\alpha_{eff}(T)$ can be written in terms of the CTE of the spacer, $\alpha_s(T)$, and the CTE of the mirrors, $\alpha_m(T)$:

$$\alpha_{eff} = \alpha_s + 2\delta \frac{R}{L}[\alpha_m(T) - \alpha_s(T)], \tag{6.2}$$

where R is the radius of the spacer, L is the length of the spacer, and δ is a parameter that is dependent on the geometry and material properties of the cavity, but not the temperature or CTE of the materials [72]. Using backing rings, which are rings made of the spacer material optically contacted to the back-sides of the mirrors, can reduce the δ term and make $\alpha_{eff} \sim \alpha_s$.

6.1 CTE Simulations

For the portable Yb clock, long-term stability is critically important. In order to minimize the sensitivity to temperature, which causes the laser frequency to drift, the effective cavity CTE was simulated in a finite element analysis software, COMSOL.

The cavity is a mixed material cavity. The spacer is made of ULE and the mirrors are made of FS. The spacer has a 50 mm diameter, is 25 mm long, and has 7 mm diameter central bore. The mirrors are 25.4 mm in diameter and 6.35 mm long. After careful simulations, the backing ring was designed to be 4.5 mm long with the same outer diameter as the mirrors and a 5 mm inner diameter. The ULE of the spacer and the mirrors is a specialty ULE that has been designed to have a zero-crossing 45 °C ±5°C. Unless otherwise specified, the plots in the following sections will default to these design parameters (and those more thoroughly described in Table 6.1) while varying a single parameter. Fig. 6.1 shows what the Yb geometry looks like in COMSOL.

The simulation in COMSOL uses custom equations for the CTE of the ULE and the FS

Spacer length	25 mm
Spacer diameter	50 mm
Mirror diameter	25.4 mm
Mirror length	6.35 mm
Bore hole diameter	7 mm
Bore hole chamfer	1.5 mm
Mirror, backing ring, and spacer chamfer	0.5 mm
Backing ring outer diameter	25.4 mm
Backing ring inner diameter	5 mm
Backing ring length	4.5 mm
Optical spot size, ω_0	0.36 mm
Contact area (between mirror and spacer) inner diameter	6.35 mm
Holding ring radius	23 mm
ULE zCTE, T_0	45 °C
Simulation reference temperature	T_0
a	2.4×10^{-9} 1/K^2
Secant CTE ULE	$a(T - T_0)/2$
Secant CTE FS	500×10^{-9} 1/K

Table 6.1: A table of the parameters used in the COMSOL CTE simulations of the portable Yb Cavity. Note that the expression for the secant CTE of ULE is only valid when $T_{ref} = T_0$.

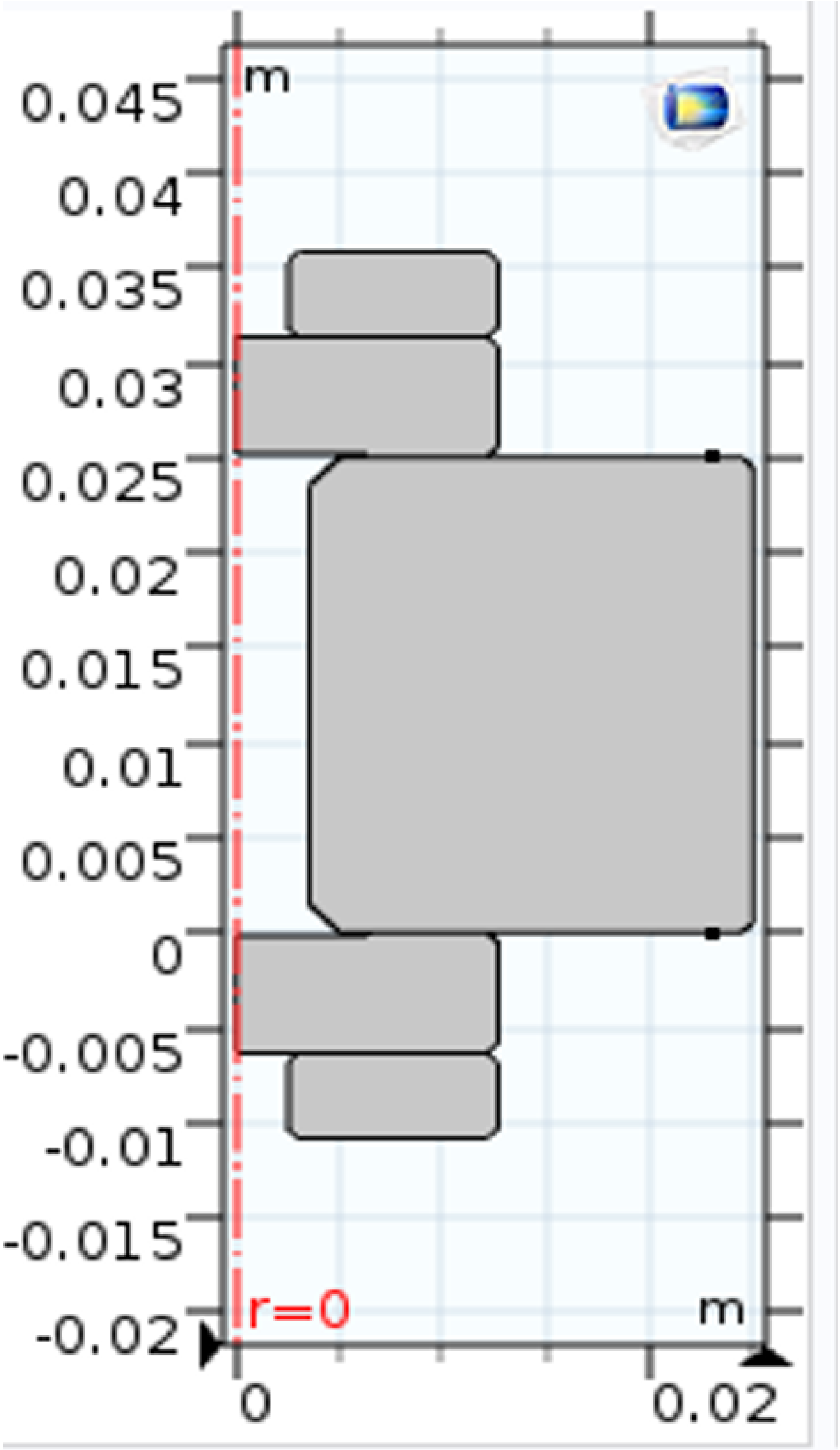
m
0.045
0.04
0.035
0.03
0.025
0.02
0.015
0.01
0.005
0
-0.005
-0.01
-0.015
-0.02
r=0
m
0
0.02

Figure 6.1: The Yb cavity geometry in COMSOL. The model is axis-symmetric around r=0. Technically, only the top half of what is drawn here is needed because the cavity is symmetric in the plane perpendicular to the optical axis (r=0 axis) as well.

based on Legero's paper. The CTE of the ULE, $\alpha_{ULE}(T)$ is:

$$\alpha_{ULE}(T) = a(T - T_0) + b(T - T_0)^2 \tag{6.3}$$

Where T_0 is the zero-crossing temperature of the ULE. For most of the simulations, we assume that $a = 2.4 \times 10^{-9}[1/K^2]$ and $b = 0[1/K^3]$ unless otherwise explicitly noted. The CTE of FS, α_{FS}, was set to $500 \times 10^{-9}[1/K]$.

The coefficient of thermal expansion CTE equation, Eq. 6.3, describes the instantaneous or tangent CTE. It is important to note that COMSOL prefers a different formulation, the secant CTE. Tangent CTE or instantaneous CTE is defined like this:

$$\frac{dL}{L} = \alpha_{tangent} dT \tag{6.4}$$

Secant CTE, which is more commonly used in engineering contexts, depends on the reference temperature, T_{ref}, at which the length of the material is L_0.

$$\frac{\Delta L}{L_0} = \alpha_{secant}(T, T_{ref})\Delta T \tag{6.5}$$

To convert from instantaneous CTE to secant CTE, we can integrate Eq. 6.4 from T_{ref} to T:

$$ln(L/L_0) = \int_{T_{ref}}^{T} \alpha_{tangent}(\tau) d\tau. \tag{6.6}$$

We define $I(T, T_{ref})$:

$$I(T, T_{ref}) = \int_{T_{ref}}^{T} \alpha_{tangent}(\tau) d\tau \tag{6.7}$$

So that,

$$\frac{\Delta L}{L_0} = \frac{L}{L_0} - 1 = e^{I(T,T_{ref})} - 1. \tag{6.8}$$

For most temperatures and materials, $I(T, T_{ref}) \ll 1$, such that:

$$\alpha_{secant} = \frac{I(T, T_{ref})}{(T - T_{ref})}. \tag{6.9}$$

Let's consider FS, where $\alpha_{FS,tan}$ is a constant, which we will call, c:

$$\alpha_{FS,secant} = \frac{\int_{T_{ref}}^{T} c d\tau}{T - T_{ref}} = c \tag{6.10}$$

So, $\alpha_{FS,tan} = \alpha_{FS,secant}$. What about ULE? If $\alpha_{tan,ULE} = a(T - T0)$,

$$\alpha_{secant,ULE} = \frac{\int_{T_{ref}}^{T} a(\tau - T0)d\tau}{T - T_{ref}} = \frac{a}{2}(T + T_{ref} - 2T_0). \tag{6.11}$$

For the special case of $T_{ref} = T_0$, $\alpha_{FS,secant}(T, T_0) = \alpha_{FS,tan}(T)/2$. Because the CTE of ULE is small, it is reasonable to set $T_{ref} = T_0$ (the measured L_0 is not measured to a part in 10^{-7} anyway, only relative changes are measured well), but for some materials, it may not be as straightforward. For more information on thermal expansion in COMSOL, please see this documentation: https://doc.comsol.com/5.4/doc/com.comsol.help.sme/sme$_{u}g_{m}odeling.05.115.html$

Fig. 6.2 shows a result from a CTE simulation. The output of the simulation is the fractional length change in the cavity at different temperatures. There is an arbitrary offset in this plot in the sense that the zero length change point is set by the user (this is the same as the starting temperature of the simulation, T_{ref}). Because of this arbitrary offset and in order to make it easier to read the zero-crossing point, I typically take the derivative of this plot, which is shown in the figure as well.

The exact CTE zero-crossing of ULE, zCTE, depends on the doping of Titania in the glass [71]. Fig. 6.3 shows what would happen to the effective cavity CTE given a ULE with different zero-crossing and without a backing ring. Without the backing ring, the term that describes the strain between the mirror and the spacer in Eq. 6.2 dominates. Changing the zCTE of the ULE does not significantly change the effective cavity CTE when there are no backing rings on the cavity.

However, if backing rings are added to the cavity, the second term in Eq. 6.2 can be minimized, and the effective cavity CTE should depend more on the CTE of the ULE used in the spacer (and in the backing rings). The results from this simulation are shown in Fig. 6.4. The effective cavity CTE is much more sensitive to the CTE of the ULE in this case, and the zCTE of the cavity is very similar to the zCTE of the spacer.

The exact zero-crossing depends strongly on the geometry of the backing ring. Fig. 6.5 shows how the inner diameter of the backing ring affects the effective cavity CTE. The “1 mm ring” represents nearly a full disk. A ”thicker” ring (smaller inner diameter) is ideal for shifting

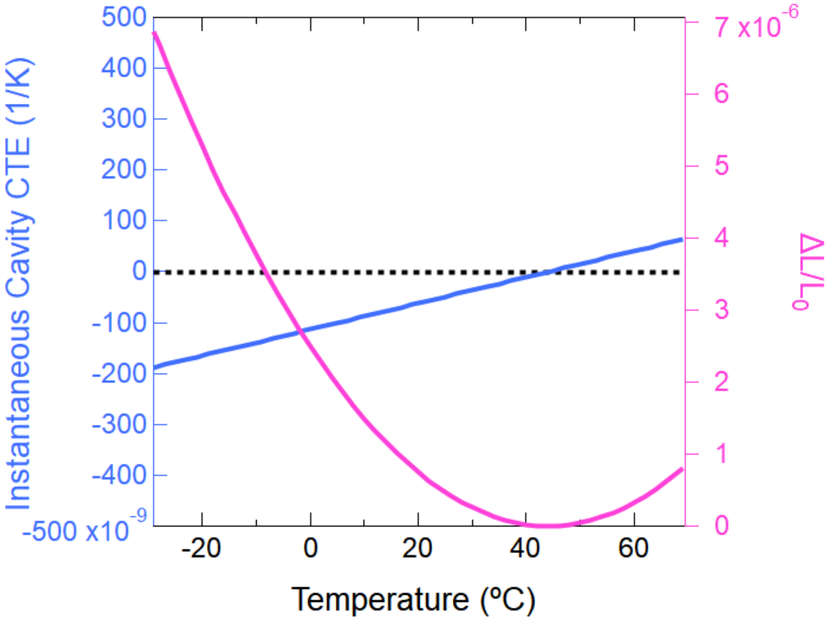

Figure 6.2: **The right side axis and pink plot** is the simulated fractional length change of the portable Yb cavity design at different temperatures. Note that there is an arbitrary offset in the sense that the user sets the zero length change temperature, T_{ref} where $L = L_0$. **The Left side axis and purple trace** is the instantaneous CTE of the cavity as a function of temperature. Where this line crosses zero, the cavity is the least sensitive to temperature. This plot is for the simulation of the Yb cavity with all of the default/expected parameters. The zero-crossing in this case $\approx 44°\mathrm{C}$.

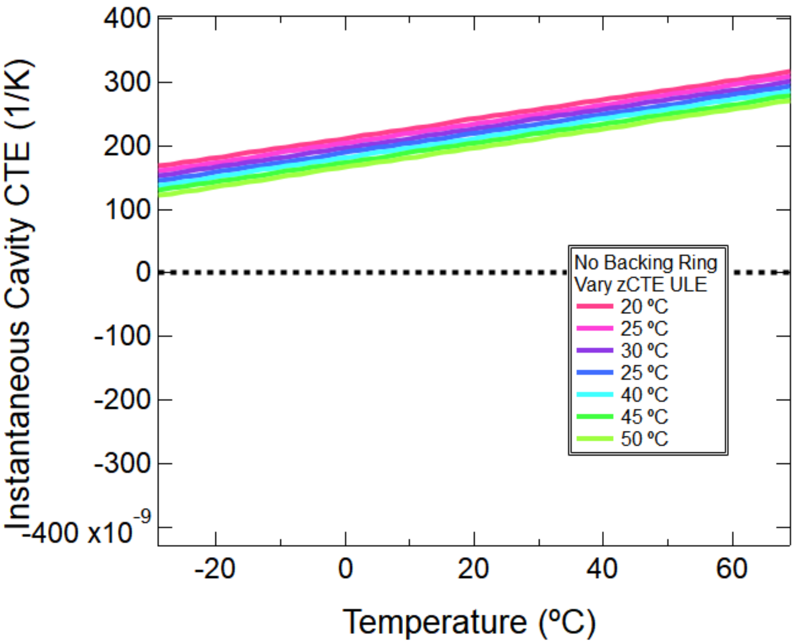

Figure 6.3: This plot demonstrates the sensitivity of the cavity CTE to the zero-crossing of the ULE used in the spacer when there are no backing rings on the cavity. The cavity CTE is not very sensitive the ULE CTE zero-crossing. This method cannot be used to change the effective cavity CTE to above room temperature.

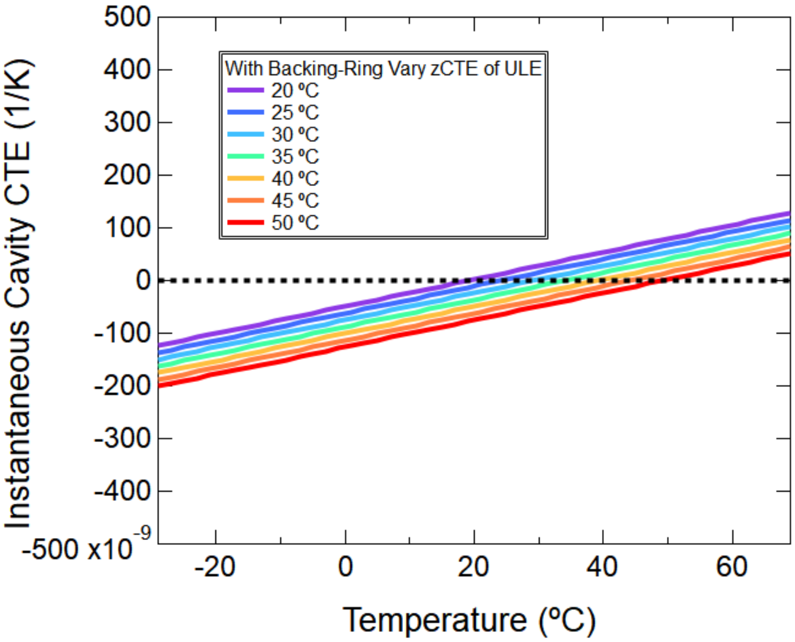

Figure 6.4: This plot shows that the cavity CTE is sensitive the CTE zero-crossing of the ULE used in the spacer and the backing rings. With backing rings, the strain between the mirror and spacer is minimized and the zCTE of the cavity is nearly the zCTE of the spacer.

the zCTE of the cavity up. Fig. 6.6 shows the effective cavity CTE dependence on backing ring thickness. Thicker rings increase the zCTE crossing point of the cavity until the ring is about 6 mm thick, then there are diminishing returns on backing ring thickness.

Fig. 6.7 shows the dependence of the effective cavity CTE on the contact area between the mirror and the spacer when there is no backing ring on the cavity mirrors and Fig. 6.8 shows the same plot when there are backing rings. From previous COMSOL simulations, we understood that this was an important parameter and one that can be difficult to predict. Imperfections in the polishing process lead to variability in this parameter. However, when there are backing rings on the mirrors, the zCTE of the cavity is insensitive to the mirror-spacer strain and also less sensitive to the contact area between the mirror and spacer.

After mounting the optical cavity and setting up the laser lock, we measured the CTE of the cavity by tracking the locked laser frequency as we changed the temperature of the vacuum chamber. The results were very surprising. Fig. 6.9 shows the measured frequency shift vs. temperature for the portable Yb cavity as well as a parabolic fit to the measured data pints. The fit suggests a CTE zero-crossing of 63 °C, which is much higher than the predicted zero-crossing of 44 °C.

By converting to a fractional frequency shift and taking the derivative of the fit, we can compare the predicted effective cavity CTE to the measured cavity CTE, which is shown in Fig. 6.10. The measured CTE curve is substantially different than the simulated curve.

Let's reconsider Eq. 6.2 and the CTE ULE estimation (Eq. 6.3):

$$\alpha_{eff} = a(T-T_0) + b(T-T_0)^2 + 2\delta\frac{R}{L}[\alpha_m(T) - a(T-T_0). - b(T-T_0)^2] \tag{6.12}$$

Let's assume it is reasonable to estimate $b = 0$ and that $\alpha_m(T)$ is a constant around room temperature, then:

$$\alpha_{eff} = a(T-T_0) + 2\delta\frac{R}{L}[\alpha_m - a(T-T_0)]. \tag{6.13}$$

For our cavity, R/L is 1. We can re-write this as:

$$\alpha_{eff} = a(1-2\delta)(T-T_0) + 2\delta\alpha_m. \tag{6.14}$$

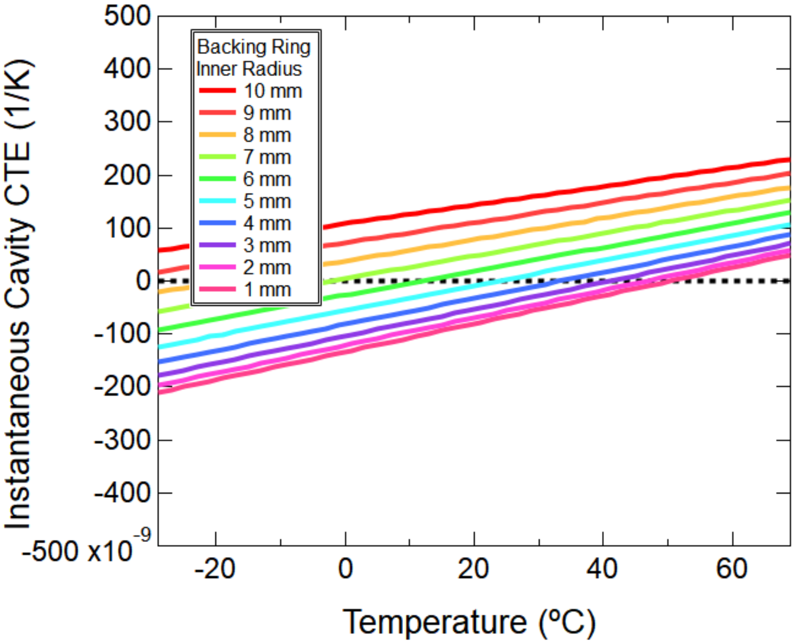

Figure 6.5: This plot shows the cavity CTE dependence on backing ring inner radius. In this case, 1 mm diameter represents nearly a full disk and 10 mm diameter represents the thinnest ring simulated. More backing ring contact with the mirror represent causes a higher cavity CTE, but a hole in the backing ring is required for the AR coating on the mirror and to avoid etalons in the backing ring.

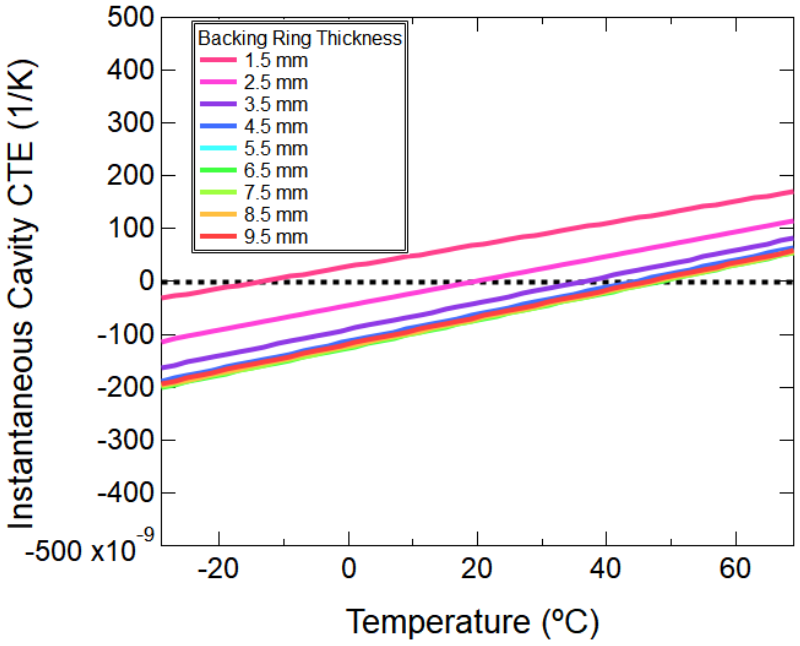

Figure 6.6: This plot shows how the cavity CTE depends on the thickness or height of the backing ring. There are diminishing returns for increasing backing ring thickness. There is almost no change in the cavity CTE zero-crossing from 6mm-10mm.

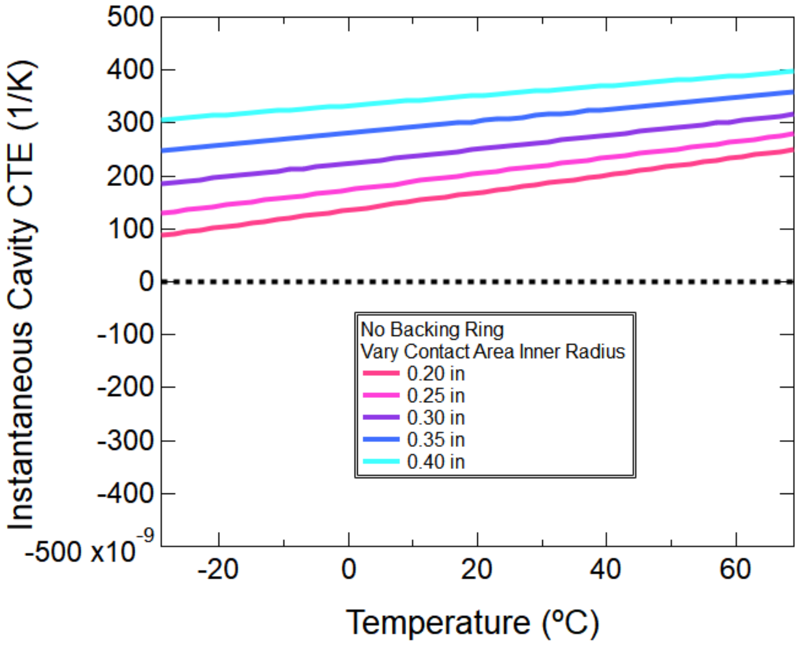

Figure 6.7: This plot demonstrates cavity CTE dependence on contact area when there is no backing ring. Imperfections in mirror or spacer polishing can limit the contact area. Without a backing ring, these variations can make the exact cavity CTE at room temperature difficult to predict.

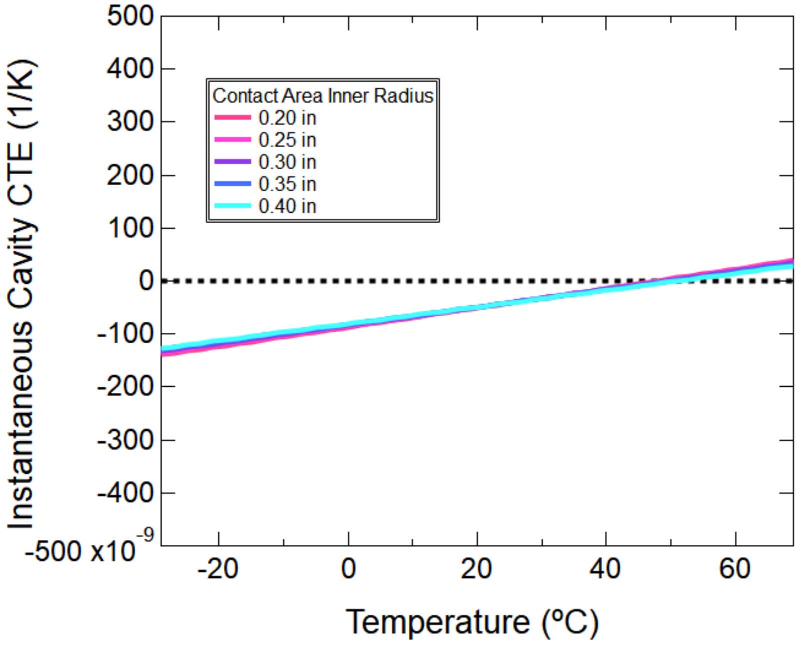

Figure 6.8: This plot demonstrates cavity CTE dependence on contact area when a backing ring is applied to the cavity mirrors. Imperfections in mirror or spacer polishing can limit the contact area. However, the presence of a backing ring, reduces the effective CTE sensitivity to stain in the mirror-spacer interface and also variations in contact area.

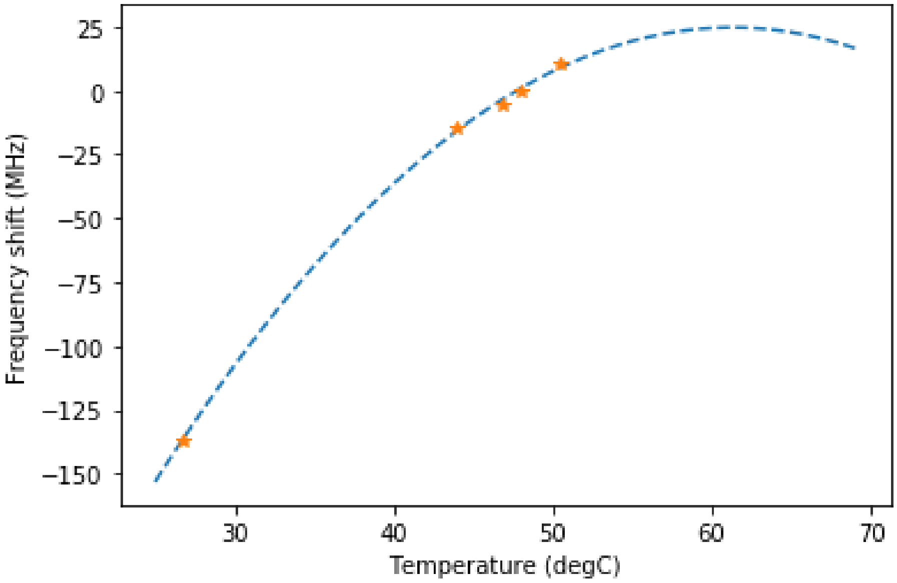

Figure 6.9: A measurement of the cavity frequency vs temperature. A a parabolic fit is used to estimate the expected zero-crossing.

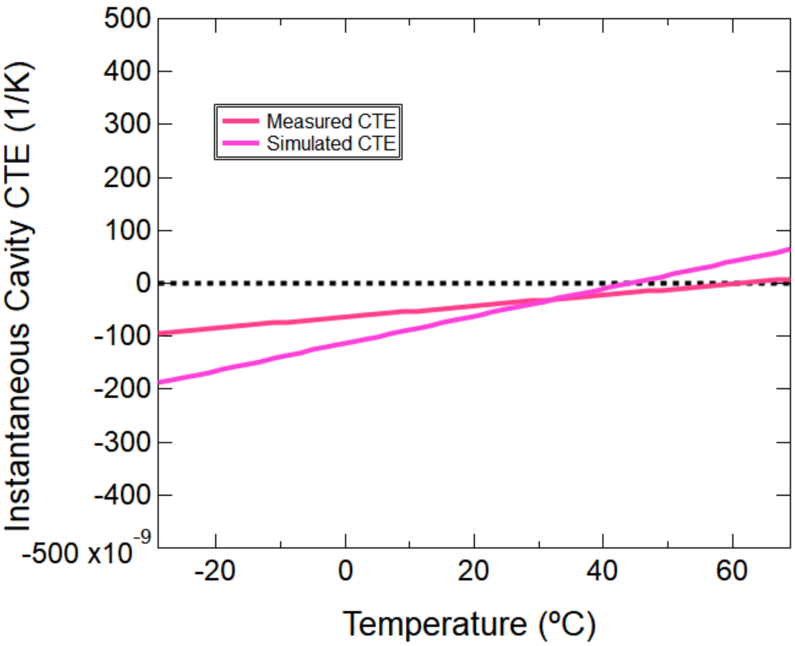

Figure 6.10: The measured instantaneous cavity CTE vs the COMSOL simulated cavity CTE.

The slope of the curve can be written as $a(1-2\delta)$. The simulated slope $\approx 2.6\times10^{-9}$, so $\delta \approx -0.04$. The cavity effective CTE should be very similar to the the spacer CTE when δ is small. The slope of the measurement, is $\approx 1.0\times10^{-9}$ [1/K] and the zero-crossing is above 60 °C. This implies that the spacer material CTE has both a different slope and zero-crossing than expected. However, there may be something wrong with the measurement or our simulation inputs. In terms of the measurement, there are very few points in the frequency versus temperature plot (Fig. 6.10). It takes approximately 1 week to add 1 point to the temperature plot due to the heat shields around the cavity. The temperature is measured on the outside of the can where heater tape is applied. A week of measurement time was required to allow cavity to thermalize and for the frequency to be within 1 MHz of the fully settled value. Ideally, for a good parabolic fit, there would be points after the derivative change. However, during this measurement, the ion pump died. A new measurement will need to be completed now that that the ion pump has been replaced. It would also be ideal to heat the cavity shields instead of the outside of the vacuum can in order to reduce the thermal mass to be heated and amount of time required to heat the cavity. On the other hand, this measurement strongly implies that there will not be a zero-crossing at or below 50°C, which still is still inconsistent with the simulations. I built confidence in the simulations by running them on a cavity in the Legero et al. paper (for which there are both simulation results and measurements) with good agreement. In the following subsection, I revisit the COMSOL simulations with more careful consideration of the cavity holding structure, but this does not explain the discrepancy either. At this point it seems likely that there is a problem with our understanding of the material properties or the system behaviour. I suspect that the highly doped ULE has material properties that are different from my simulation inputs, but more investigation is needed.

6.1.1 CTE and Holding Force

The CTE of the cavity is much less than the CTE of the holding structure, which is made of Invar. It is reasonable to wonder if a change in the holding structure may induce a CTE change in the cavity. To get a sense of the correct order of magnitude, we may want to consider the stress-strain relationship for the Viton o-rings that sit between cavity and mounting structure:

$$\sigma = \epsilon E = \frac{\Delta L_{viton}}{L_{viton}} E, \tag{6.15}$$

where σ is the stress (force per area), ϵ is the strain (fractional length change), and E is the Young's modulus. Invar is a lot more rigid than Viton, so we can assume that $\Delta L_{viton} = -\Delta L_{invar}$. We want to know how the force applied to the cavity changes with temperature, so we can write the length change in terms of the CTE of Invar.

$$\Delta F(T)/\Delta T = \sigma A = -(\alpha_{invar} L_{invar}) \frac{E}{L_{viton}} \pi (r_{outer}^2 - r_{inner}^2) \tag{6.16}$$

Here $r_i nner$ and $r_o uter$ are the inner and outer radii of the cylindrical cavity. For the Yb cavity, this works out to be ≈(100 mN/K).

If we re-run the CTE simulation where the holding ring pushes on the cavity in this temperature dependent way, there is no significant change in the effective CTE of the cavity. However, there is a worst case example we may want to consider. Suppose that the Viton o-rings are extremely over compressed and no longer compressible. In this case the displacement where the rings touch the spacer is equal to the displacement applied by the holding structure. This does change the zCTE of the cavity, as shown in Fig. 6.1.1,

6.1.2 Millimeter Cavity CTE

The all ULE cavity in Chapter 4 is made of legacy material from NIST for the spacer and off-the-shelf ULE mirrors. The exact zCTE of the spacer and mirrors is unknown, but the material properties should be similar enough that the strain between the mirror and spacer should be small. The effective CTE of the cavity should be similar to that of the spacer. I tried to measure this CTE in Fig. 6.12, but found no zero-crossing below 55°C, which is surprising for ULE.

6.2 Temperature Isolation & Heat Shields

Even when the cavity is designed to be insensitive to temperature, care must be taken to isolate the cavity from any external temperature fluctuations, $S_{T_0}^{1/2}(f)$. Although the cavity is op-

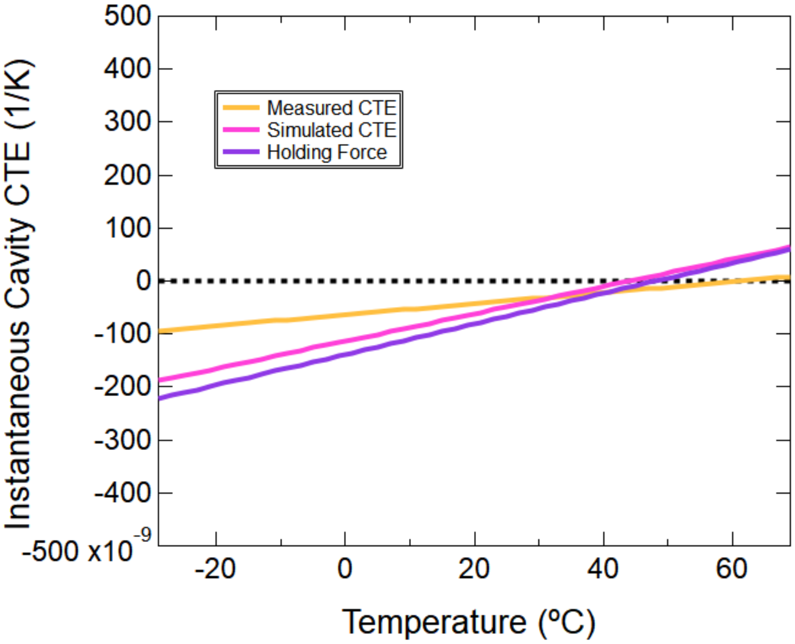

Figure 6.11: The simulated CTE of the cavity when the displacement in the holding rings is equal to the displacement of the holding structure (worst case scenario). The effective cavity CTE does change in these conditions, but not enough to explain the discrepancy in the measured cavity CTE.

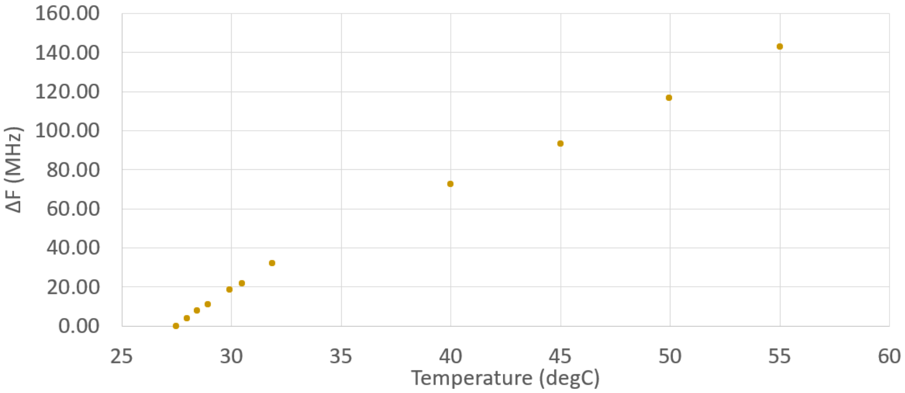

Figure 6.12: A measurement of the relative frequency shift of the all ULE mm-scale cavity versus temperature. Surprisingly, no zero-crossing was found below 55 °C. The spacer was made of legacy ULE stored at NIST and has unkown material properties.

erated near the zCTE point, there are limitations in the precision and accuracy of temperature feedback control. To see the best possible performance, temperature fluctuations from the environment can be suppressed using heat shields. In the limit of radiation-dominated heat transfer, these heat shields act like low pass filters on the heat transfer [94].

The transfer function, $\tilde{H}_{ij}(\omega)$ between two layers in a heat shield can be written as:

$$\tilde{H_{ij}}(\omega) = \frac{\tilde{T_j}(\omega)}{\tilde{T_i}(\omega)} \tag{6.17}$$

Where $\tilde{T_i}(\omega)$ is the temperature of the i^{th} layer. To find the form of this transfer function, one can either solve for the result in COMSOL or analytically solve the Fourier transform of the heat exchange equation:

$$\dot{q}_V = \rho c \frac{\partial T}{\partial T} - \nabla \cdot (k \nabla T) \tag{6.18}$$

Where ρ is the density, c is the specific heat, and k is the thermal conductivity. For radiative heat transfer ,

$$\dot{q}_j(T) = \frac{\sigma A_j [T_i^4(t) - T_j^4]}{\beta_{ij}} \tag{6.19}$$

Where σ is the Stefan-Boltzmann constant, A_j is the area, T_j is the temperature in Kelvin of the respective layers and β_{ij} is a term including the view factors and emissivities, (see Sanjuan et al. [94] for details). In the simplest case of radiative heat transfer with no temperature gradients in the layers, all layers have the same material properties, and the layers are uncoupled, the heat transfer can be written as:

$$\tilde{H}(\omega) = (1 + i\omega\tau)^{-N} \tag{6.20}$$

Where there are N concentric thermal shields (N + 1 layers) and τ is the time constant of the system or the inverse of the characteristic frequency, ω_C^{-1}:

$$\omega_C = \frac{4\sigma A_j T_0^3}{m_j c_j \beta_{ij}}. \tag{6.21}$$

In this way, the heat shields act as low-pass filters for temperature fluctuations. In order to improve the stability of the optical cavity, one can increase the number of layers of the heat shields or improve the characteristic frequency of the layers by improving the emissivity of the layers, for example.

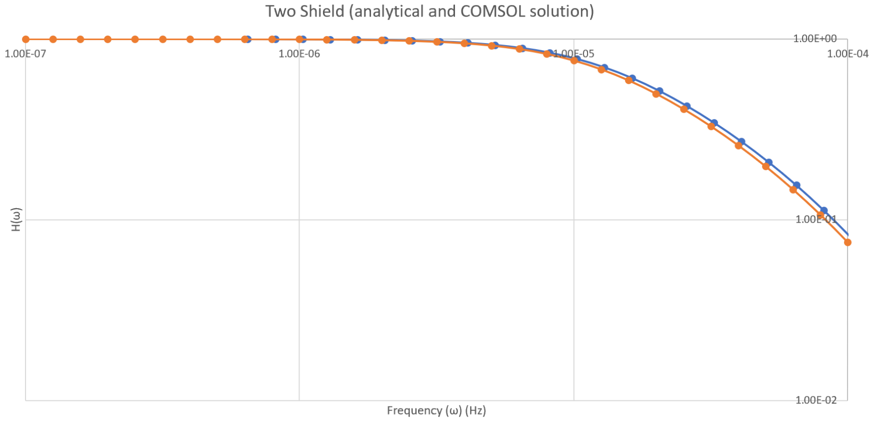

Figure 6.13: The simulated (blue) and calculated (orange) transfer function for two layers of aluminum heat shields with an emissivity of 0.4. The time constant of this system is greater than half a day.

The solution that is written in Eq. 6.20 makes many simplifications. For a more complete solution, including conductive heat transfer of the supports, please see Sanjuan et al. [94]. We used the solutions from this paper and COMSOL modeling to determine the number of heat shields required for the Yb Cavity.

It can be difficult to get the exact parameters for the heat shield calculations/simulations. Emissivity for example, can depend on variability of the polishing of the surface. However, the simulations can be used to draw conclusions which are useful to the design. In general, what works best is highly polished shields with small apertures for the optical beam bath. The supports should have a small cross section and be made of a low thermal conductivity material.

Fig. 6.13 shows the results from a heat shield COMSOL simulation and the analytical calculation for the same design. The simulated shields are made of aluminum and have an emissivity of 0.4. The time constant for this system is greater than half of a day, which means fluctuations on times scales of less than half of a day will be filtered out.

Fig. 6.14 shows a photograph of the head shields used with the portable Yb cavity. The heat shields have been specially polished to improve emissivity.

To measure the CTE of the cavity, I changed the temperature of the vacuum can enclosure

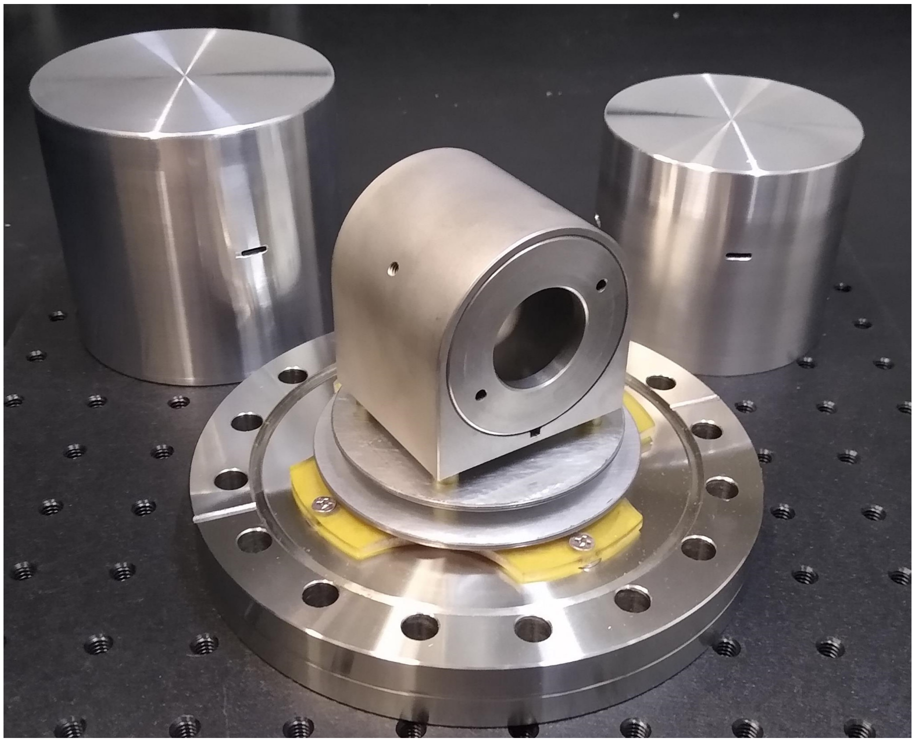

Figure 6.14: Photograph of the optical cavity mount and the heat shields. The mounting structure is made of heat-treated Invar. The structure supported by PEEK screws and PEEK spacers are used to separate the heat shields. PEEK is used because of its low thermal conductivity. The heat shields are made of Aluminum and have been polished to increase the emissivity. In this photo a PEEK base plate is used to attach the structure to a 6” CF vacuum flange, however, this piece was later replaced with an identically shaped Macor part. This was because the PEEK base plate was found to increase the vacuum pressure of the chamber. PEEK is considered a vacuum-compatible material at the pressures we are interested in, $\sim 10^{-7}$ Torr, so there may have been a problem with this particular sample. We make no claim about the vacuum compatibility of these materials.

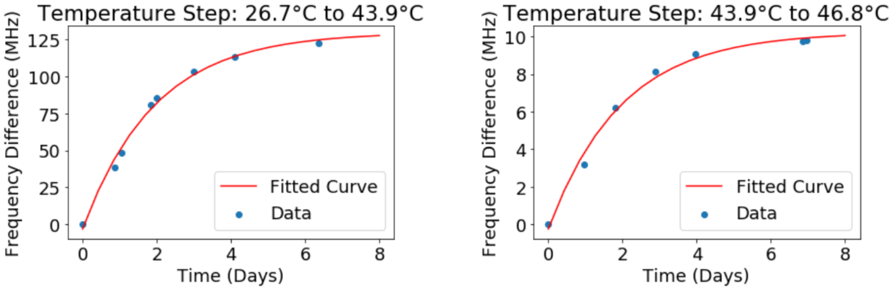

Figure 6.15: Laser frequency change versus time for two different temperature changes applied to the outside of the vacuum can for the Yb cavity.

and waited for the frequency of a beat note between a laser locked to the cavity and a laser locked to a more stable cavity to settle out. For a few of the temperature steps, I recorded the frequency versus time shown in Fig. 6.15. I fitted these curves to an exponential decay fit, $F = Ae^{-t/\tau} + F_0$, and found that the time constant, τ, was 2 days. This is a good indication that the heat shields are working well.

Chapter 7

Acceleration, Vibration, and Holding Force Sensitivity

7.1 Holding Force

Lab-based cavities can rest on surfaces without being clamped, but portable cavities must be rigidly held. The holding structure can cause the length of the cavity to change. This can be understood by considering the behavior of a linear elastic cylinder compressed on the end faces either near the center or the outer diameter (see Fig. 7.1). For a small ring-radius holding force, the length of cylinder's central axis will reduce as the holding force is increased. In contrast, when squeezed at a large diameter near the cylinder's rim, distortions in the spacer shape cause the length along the central axis to increase. A first-order holding force-insensitive point on cavity length lies in between these two extremes. This simple description is complicated by the fact that spacer distortions are coupled to mirror distortions, such that the mirror diameter, thickness and

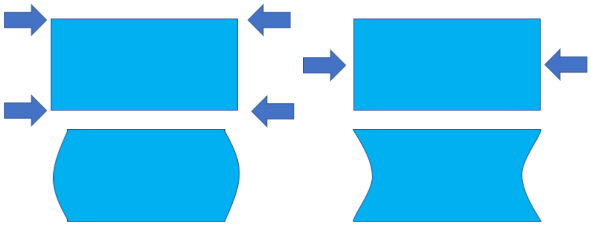

Figure 7.1: A cartoon demonstrating how where a linear elastic cylinder is held on its endfaces might change the length along the z-axis of the cylinder. In the first case, when the edges of the cylinder are compressed, the cylinder bows outward, representing and increase in cavity length. In the second case, when the compression occurs along the center of the cylinder, the endfaces bow inward, representing a decrease in cavity length.

the contact area between the mirror and spacer impact the holding force sensitivity. Moreover, depending on the spacer's aspect ratio, the holding force insensitive radius may be too close to the outer rim to be practicable. Simulations can be used to gain intuition about what kind of cavity parameters are important to holding force sensitivity.

To find this holding force insensitive point, we use COMSOL to model the cavity. In this chapter, the COMSOL simulations for the FS-ULE and ULE-ULE cavity are compared to direct measurements of the cavity holding force sensitivity and found to be in good agreement. The Yb cavity holding force is simulated, but these simulations are not experimentally verified. The Yb cavity was very prone to contamination or excess loss caused by some sort of particle on the mirrors. The holding force sensitivity measurements are typically performed in air, and were deemed too risky for the Yb cavity, which is operated at 1156 nm. There are water absorption lines near 1156 nm, and there is a possibility that the strong light field in the cavity could lead to evaporation of water onto the mirrors leaving a residue behind.

For the Yb cavity, the holding force sensitivity was simulated with spacers of varying diameter. Fig. 7.2 shows the results of this simulation. In general, more "pancake-like" cavities (where $R > L$), have holding force zero-crossings.

To simulate this holding force sensitivity for our for the FS-ULE and ULE-ULE cavities, an axisymmetric cavity model was built in FEA simulation software, and a simulated force was applied to the ULE spacer end faces along a $\sim$0.2 mm-wide ring that is equal and opposite on both ends of the cavity. Cavity length changes were calculated as a function of the holding force ring radius. As expected, the holding force sensitivity depends on many parameters such as mirror thickness and diameter, spacer thickness and diameter, and contact area.

Fig. 7.3 shows how the holding force sensitivity of the ULE-ULE cavity depends on the contact area between the mirror and spacer. It is useful to know that holding force is sensitive to this parameter because it can be difficult to control the contact area exactly. The mirrors are hand polished. When the radius of curvature of the mirrors is large, the sag is very small. This means that it can be difficult to obtain a smooth surface without changing the amount of contact area

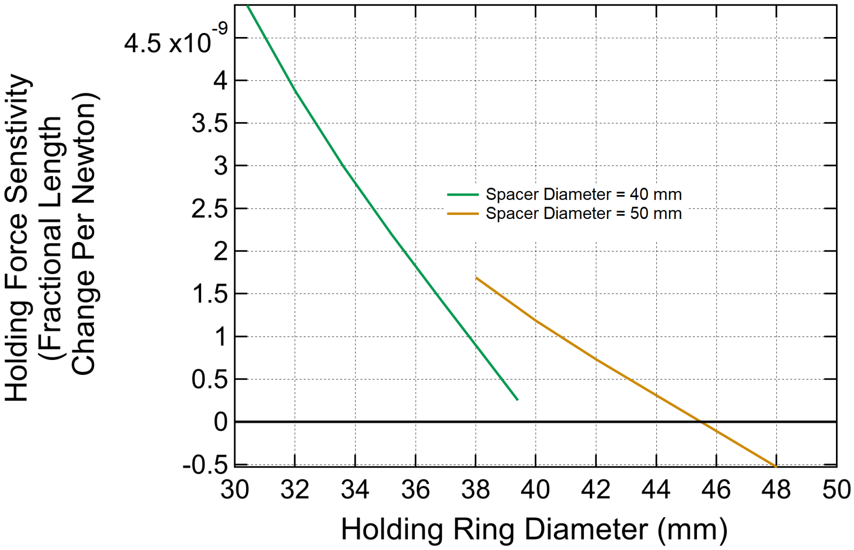

Figure 7.2: A holding force sensitivity plot for the Yb cavity based on COMSOL simulations. With the green trace, the spacer diameter is set to 40 mm. There is no holding force zero-crossing before the edge of the spacer with this cavity. In the gold trace, the spacer diameter is set to 50 mm. There is a zero-crossing in the holding force sensitivity near 45 mm in this case. In general, more "pancake-like" (R larger than L) cylindrical cavities have holding force zero-crossings.

between the mirror and the spacer. Further polishing the contact annulus can quickly erase the curved center of the mirror and further polishing the curved portion of the mirror can change the amount of contact annulus.

7.1.1 FS-ULE and ULE-ULE Holding Force Measurement

Sensitivity to holding force was measured and compared to simulations, as shown in Fig. 7.4. The cavity is held by rings on the end faces of the spacer, and can be first-order insensitive to changes to the holding force. For the FS-ULE cavity and an optical contact annulus width of 6.4 mm, a holding-force zero-crossing is predicted for a holding diameter just above 20.5 mm, slightly larger than our largest o-ring. Perhaps more importantly, simulations of the FS-ULE cavity geometry show a weak dependence of the holding force sensitivity to the o-ring diameter. This can benefit manufacturability because it can be difficult to obtain an o-ring with diameter that exactly matches that of the zero-crossing. To further verify our holding force results, we simulated and measured the holding force sensitivity of the all-ULE cavity, also shown in Fig. 7.4. In this case, the holding rings are placed on the backside of the mirrors. For both cavity designs, the dependence of holding force sensitivity on the contact area is displayed using the shaded sections. For each simulation, the upper bound of the shaded region represents a larger contact area, and the lower bound represents a smaller contact area. The primary cavity design (FS-ULE) has a lesser dependence on contact area and is more resilient to manufacturing error in this way.

To measure the holding force sensitivity, the cavity was mounted in air with the optical axis aligned vertically (parallel to the force due to gravity). A small weight of known mass was applied to the top of the cavity for each available holding diameter. The change in frequency of a laser locked to the cavity was observed, and the resulting fractional frequency shift per newton was calculated. The weight was applied and removed a minimum of eight times to establish statistics on the reproducibility of holding force sensitivity measurement. Potential systematic errors, such as a small angle between the optical axis and the force due to gravity, are ignored.

The results are consistent with the simulations, verifying our understanding of the cavity

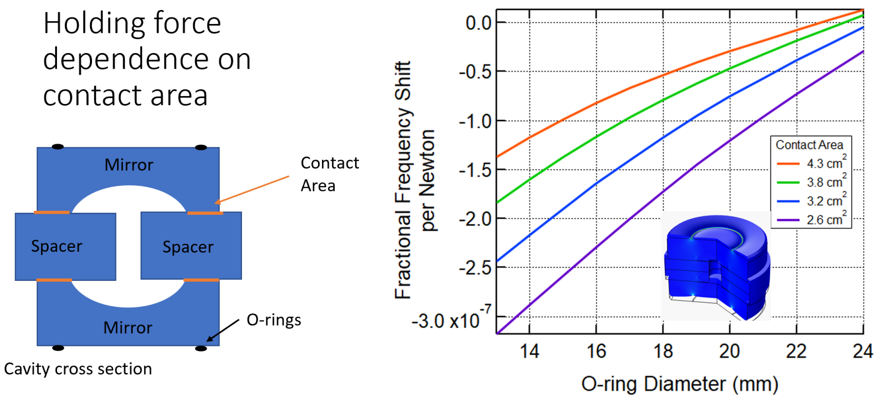

Figure 7.3: **Left:** an exaggerated cartoon showing the contact area between the mirror and spacer. **Right:**A plot showing holding force sensitivity vs o-ring diameter for the ULE-ULE cavity. Each trace represents a different contact area between the mirror and spacer. From top to bottom the contact area decreases. The contact area between the mirror and spacer is a variable that can be difficult to control exactly due to variations in the polishing step and a very small sag in the mirror for large radius of curvature, but the green trace is the ideal and the blue trace is similar to what we observed in the lab as the clear area between the mirror and spacer.

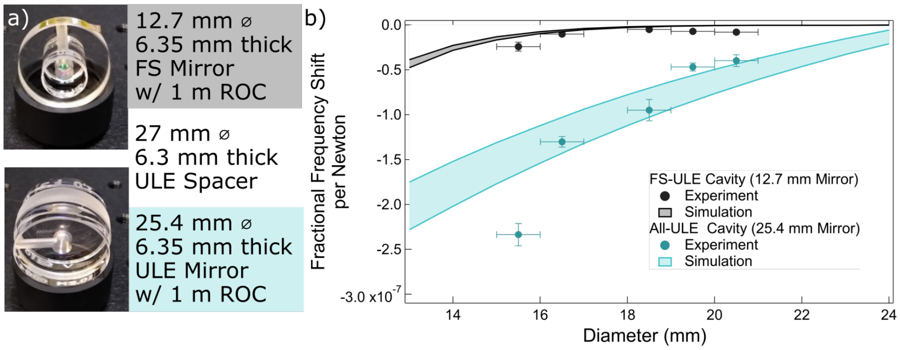

Figure 7.4: a) Photographs of the primary cavity and the supplemental all-ULE cavity. The cavities have identical spacers, but different mirrors. b) Experimental results showing the holding force sensitivity's dependence on o-ring size, demonstrating excellent agreement with the finite element analysis results, which are shown as shaded regions. The y-error bars are a combination of the standard deviation in the frequency shift measurement and the uncertainty in the mass of the weight applied. This does not include any systematic offsets. The x-axis uncertainty is an estimate based on the thickness of the o-ring (1 mm). Simulations incorporated a range of mirror-spacer contact areas, where the contact annulus width varied from 3.2 mm to 2.5 mm in the FS-ULE cavity, and 6.4 mm to 5.1 mm in the all-ULE cavity.

and its design. The primary cavity design with 12.7 mm FS mirrors has a fractional frequency shift per newton of less than 2.4×10^{-8} with all of the o-ring diameters that were tested. This behavior is contrasted with the secondary cavity with 25.4 mm ULE mirrors, where the holding force sensitivity has a stronger dependence on o-ring diameter. These simulations also agree with the holding force sensitivity measurements.

We assess the holding force sensitivity by considering a change in holding force due to a temperature change of the rigid mounting structure. By accounting for the CTE of the Invar structure and the elastic properties of the o-rings, we estimate the temperature-dependent holding force change on the cavity as ~ 3 mN/K. This leads to a fractional cavity length change of $< 10^{-10}$/K. This is several orders of magnitude smaller than the CTE of the FS-ULE cavity of $\sim 10^{-7}$/K. This is also smaller than what one could expect when operating near the cavity T_{zc}, where the CTE for a 1K change is $\sim 10^{-9}$/K. Thus, the temperature induced cavity length change will be dominated by the cavity itself as opposed to the holding force changes.

7.2 Acceleration Sensitivity

Cutting-edge vacuum-gap Fabry-Pérot cavities are typically installed on vibration-isolation platforms within soundproof enclosures. These enclosures are strategically placed in low-traffic areas, with some cases involving measurements of floor vibrations to identify the quietest spot. These measures are implemented to minimize vibration-induced frequency changes in the optical cavity. Portable cavities cannot operate in a fixed location, and although some level of active and passive vibration isolation may be used, it has to be compact enough to be mobile. Ideally, the optical cavity and its mounting structure exhibit a high degree of passive insensitivity to vibrations.

Compact cavities have the potential for inherently lower acceleration sensitivity. We can begin to understand this by imagining a glass cylinder resting on a surface under gravity. For small deformations, glass is a linear elastic material. A linear elastic cylinder resting on a surface under gravity will compress due to the stress applied to the surface of the cylinder under its own weight.

The stress-strain relationship for a linear elastic material is:

$$\sigma = E\epsilon, \tag{7.1}$$

where σ is the stress or the pressure applied, ϵ is the strain or the fractional length change, $\Delta L/L$, and E is Young's modulus that describes the stiffness of the material. The force due to gravity acting on the cylinder, F_g is related to the cylinder's mass, which we can write in terms of the density ρ, length L, area of the circle resting on the surface A: $F_g = mg = \rho g L A$. The strain is this force divided by the surface area. So, we can write the strain ϵ like so:

$$\epsilon = \frac{\Delta L}{L} = \frac{\rho g}{E} L. \tag{7.2}$$

What is significant about this expression is that the fractional length change (and therefore the fractional frequency change) depends on the length of the cylinder. If you have two cylinders with the same density and Young's modulus, the longer cylinder will be more sensitive to changes in acceleration (like g). This is why compact cavities are considered desirable for passively low acceleration sensitivity.

7.2.1 Theory

When a cavity is under an acceleration, a, in the direction of the optical axis, the cavity will be compressed by a factor that depends on its young's modulus, density, and geometry (Eq. 7.2). What about when the cavity is under vibration, $a(t)$? How does the cavity length change in this case? This question is a bit tricky when the cavity is symmetric about the plane perpendicular to the direction of acceleration. In this case, the length of the cavity, L, is the same when a is positive or negative. So, we need to think about the absolute value of the acceleration. Suppose $a(t) = A\cos(\omega t)$, now $L(t) = c|A\cos(\omega t)| + L_0$, where A is the amplitude of the acceleration modulation and c is an acceleration sensitivity coefficient. What will this look like in the frequency domain?

Let us take the Fourier transform of $L(t)$. For simplicity, let us call ωt, x. $L(t)$ is an even function, so there are no $\sin(nx)$ coefficients in the Fourier transform. For the $\cos(nx)$ coefficients:

$$l_n = \frac{1}{\pi}\int_{-\pi}^{\pi} cA|\cos(x)|\cos(nx)dx = \frac{2}{\pi}\int_{0}^{\pi} cA|\cos(x)|\cos(nx)dx. \tag{7.3}$$

The absolute value function can be a little difficult to look at so we can break it up into a piecewise function over the $[0,\pi]$ interval:

$$|\cos(x)| = \left\{\begin{array}{ll} \cos(x), & 0 \le x < \pi/2] \\ -\cos(x) & \pi/2 \le x \le \pi \end{array}\right\}. \tag{7.4}$$

Now,

$$l_n = \frac{2}{\pi}\int_{0}^{\pi/2} cA\cos(x)\cos(nx)dx - \frac{2}{\pi}\int_{\pi/2}^{\pi} cA\cos(x)\cos(nx)dx. \tag{7.5}$$

For $n = 1$, l_n =0. For $n > 1$,

$$l_n = cA\Big(\frac{2}{\pi}\Big)\Big[\frac{\cos(n\pi/2)}{1-n^2} - \frac{\cos(n\pi/2) - n\sin(\pi n)}{n^2-1}\Big]. \tag{7.6}$$

This expression simplifies because $\sin(\pi n) = 0$ for all integers n:

$$l_n = cA\Big(\frac{4}{\pi(1-n^2)}\Big)\cos(n\pi/2). \tag{7.7}$$

The first non-zero coefficient is $a_2 = cA\frac{4}{3\pi}$.

Because of symmetry, the acceleration response of the cavity is spread out into higher frequency tones. This can be an advantage because it can essentially raise the acceptable acceleration level if your goal is to keep the acceleration-induced tones below the frequency noise of the laser. In this case, the ratio of the PSD of the single tone of the acceleration to the PSD of the first non-zero tone in the length PSD is:

$$\frac{PSD_L(2\omega)}{PSD_a(\omega)} = \frac{a_2^2}{(A)^2} = c^2\frac{16}{9\pi^2} \approx 0.18c^2. \tag{7.8}$$

However, this solution assumes that the acceleration is centered around zero. Along the axis parallel to g, the vibrations will always look like $a(t) = A\cos(\omega t) - g$. Suppose $a(t)$ is always negative $(A < g)$. In this case, we do not get to take advantage of the symmetry of the cavity about the plane perpendicular to g. The PSD of the length will now have peaks at the same frequencies as the acceleration:

$$\frac{PSD_L(\omega)}{PSD_a(\omega)} = c^2. \tag{7.9}$$

This picture helps us develop intuition about how symmetry impacts the acceleration sensitivity of the cavity. When the optical axis is aligned with the direction of the acceleration, we can use the stress-strain equation and the material properties to estimate c, but for accelerations along other axes, we need to think extra carefully about how the material will flex. For this, we need to consider the deformation of the cavity under acceleration and also take into consideration the full cavity geometry including the mirrors, boreholes, and backing rings. COMSOL can be used to do this analysis. Ultimately, we find that symmetric objects perform better, but we run up against obstacles like machine tolerances. Further, the acceleration sensitivity in the symmetric case can be difficult to simulate accurately. For the Yb cavity, the number of points required to simulate the cavity carefully (and have converging results), often caused the program to crash.

Previous work on cavities ranging from 5 cm to 20 cm in length with cubic, spherical, and cylindrical geometries have demonstrated passive (without vibration feedforward correction) acceleration sensitivities in the $10^{-12}g^{-1}$ to mid $10^{-10}g^{-1}$ range [38, 5, 3, 95, 7, 96, 1, 97]. There are two common ways to measure the acceleration sensitivity. One is to flip the cavity along three mechanical axes such that the cavity experiences an acceleration change from $-g$ to g and measure the frequency shift under this $2g$ acceleration change. This method inherently involves the symmetry case, and could under-predict the sensitivity of the mechanical axis normally aligned with g. I think of this as the residual asymmetry vibration sensitivity. Another method is to place the cavity on a vibrating platform [38] and measure the frequency noise of a laser locked to that cavity at the frequency offset equal to the frequency applied. In this method, one of the axis will be more strongly aligned with g, which captures the worst case acceleration sensitivity. Although, when the vibrations are small, which they typically are, and the platform is not perfectly perpendicular to g, which can be difficult to to obtain, g will likely have some small component projecting into all of the axes tested which breaks the symmetry along all axes. Even if g does not break the symmetry, machine tolerances and the mounting structure will likely break the symmetry. Additionally, the acceleration spectrum is never really a single tone in practice. The harmonics of the tone applied are involved too. This can make disentangling the acceleration sensitivity difficult. I had hoped to see a second harmonic response in the phase noise higher than the first, but I never saw this in practice.

7.3 FS-ULE Flip Test Acceleration Sensitivity Measurements

For the Mini FS-ULE cavity, I employed the flip test method. We simulated and measured the acceleration sensitivity of our FS-ULE cavity under a 2g static flip test [3, 1, 5]. We placed the cavity in vacuum onto a rotatable optical breadboard that allowed us to flip the cavity along three mechanical axes. This table is shown in Fig. 7.5. The cavity was flipped along three mechanical axes using a special table designed to flip all of the free space optics, detectors, and the optical cavity inside of the vacuum can.

The first measurement of the acceleration sensitivity is shown in Fig. 7.6. One thing to note is that the axes that are drawn are the axes that get flipped in the measurement. There is an ambiguity with rotational axes. For example, consider the black axis that is drawn in figure 7.6. A rotation about this axis can take the optical axis from -g to g and it can also take the vent hole from -g to g. From here on out, the axes that are drawn in flip tests are the mechanical axis that are flipped. So, the red axis, for example, flips the vent hole from -g to g.

The acceleration sensitivity of axes 1, 2, and 3 in this measurement are $3 \times 10^{-9} g^{-1}$, $4 \times 10^{-10} g^{-1}$, and $1 \times 10^{-10} g^{-1}$. These values seemed a little high compared to the literature. From simulations, we knew that the mounting of the cavity could significantly impact the acceleration sensitivity. If, for example, the cavity was placed such that the o-rings were not concentric with the mirrors and spacers, this could result in a higher measured acceleration sensitivity. I remounted the cavity and measured the acceleration sensitivity again. The results of this measurement are in Fig. 7.7.

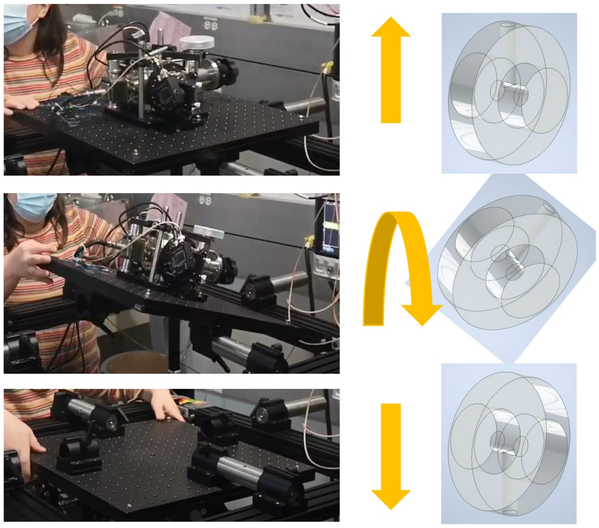

Figure 7.5: Photographs of the flip table that was used in the FS-ULE cavity acceleration sensitivity measurement next to a cartoon illustration of how the cavity orientation will change during the flip. In this case, the cavity vacuum vent hole goes from pointing up to pointing down.

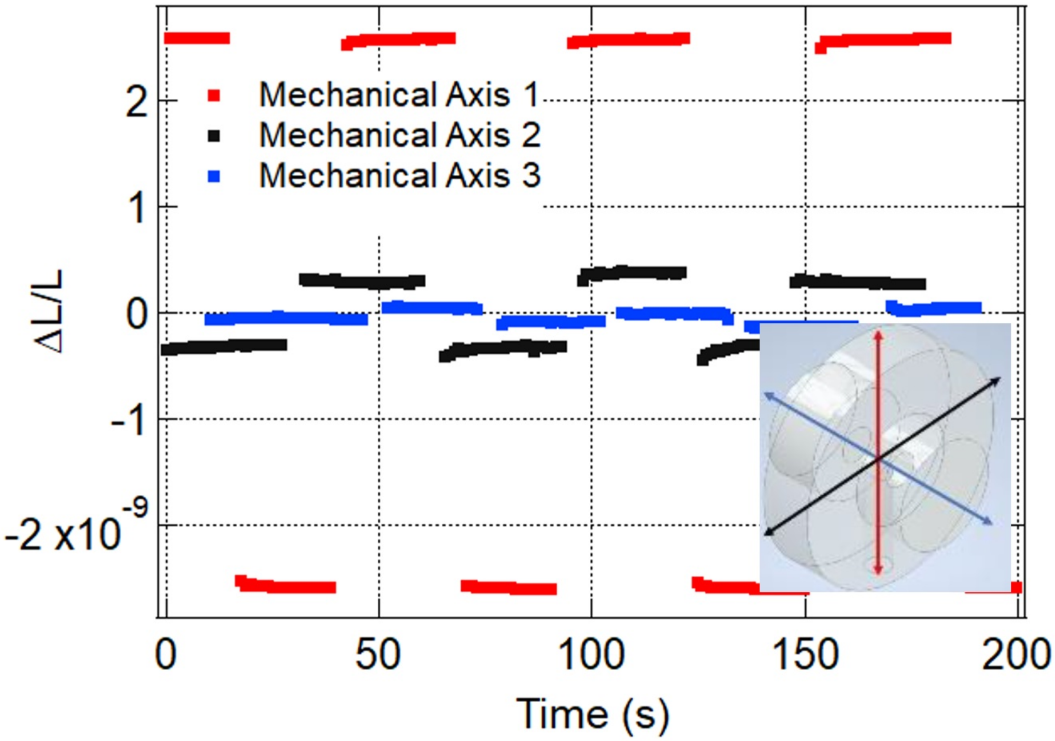

Figure 7.6: Preliminary acceleration sensitivity measurement of the FS-ULE cavity using the flip tests. A linear drift (presumably due to temperature) has been removed from the measurement. Mechanical axis 1 corresponds to the flip which takes the vent hole on the cavity from up to down. Mechanical axis 2 flips the cavity axis that is perpendicular to both the vent hole and the optical axis. Mechanical axis 3 flips the optical axis. The acceleration sensitivity of axes 1, 2, and 3 are $3 \times 10^{-9} g^{-1}$, $4 \times 10^{-10} g^{-1}$, and $1 \times 10^{-10} g^{-1}$.

The final measured acceleration sensitivities along the three axes are $5 \times 10^{-11}g^{-1}$, $3 \times 10^{-10}g^{-1}$, and $6 \times 10^{-10}g^{-1}$. The axis with the highest sensitivity corresponds to a flip that changes the cavity vent hole from pointing up to pointing down. This is the largest mechanical asymmetry in the design, and FEA simulations indicate that the acceleration sensitivity should be at best $\sim 3 \times 10^{-10}g^{-1}$ along this mechanical axis.

We note that this low level of acceleration sensitivity was achieved without active alignment of the cavity supports (although we did remount once). The cavity is simply centered in the mount by visual inspection and the Viton o-rings are centered to the mount using grooves in the holding structure. Simulations indicate that additional minor asymmetries would result in higher acceleration sensitivity. For example, offsets in the mirrors along the vent hole direction can cause $\sim 6 \times 10^{-10}g^{-1}$ per millimeter offset, and offsets in the holding rings along the vent hole direction result in $\sim 8 \times 10^{-11}g^{-1}$ per millimeter offset. A similar geometry with smaller vent holes evenly spaced radially should perform better due to a higher degree of symmetry. In the high symmetry cavity case, alignment tolerance will dominate, likely at the $10^{-11}g^{-1}$ level assuming sub-millimeter alignment tolerance, but this depends on a wide parameter space and could likely be further optimized by changing variables like mirror thickness.

7.4 Portable Yb Vibration Platform Test

In order to improve the symmetry of the cavity compared to the FS-ULE and the ULE-ULE designs, four vacuum vent holes were utilized in the Yb cavity case. The vent holes are as narrow as was deemed achievable by the machinist, 3 mm in diameter. This is because larger vent holes represent larger asymmetry in the mass distribution of the cavity. However, in future designs, it is also worth considering how narrow vent holes limit vacuum conductance. For four vent holes of 3 mm diameter and 9 mm in length (connected in parallel in terms of vacuum conductance), the estimated molecular flow vacuum conductance of air at 20°C is ≈1.5 L/s, which is on the same order as the typically pumping speed of the ion pumps we use at 3-5l/s. These narrow vent holes already represent a choke point in vacuum conductance so further study may be required in future

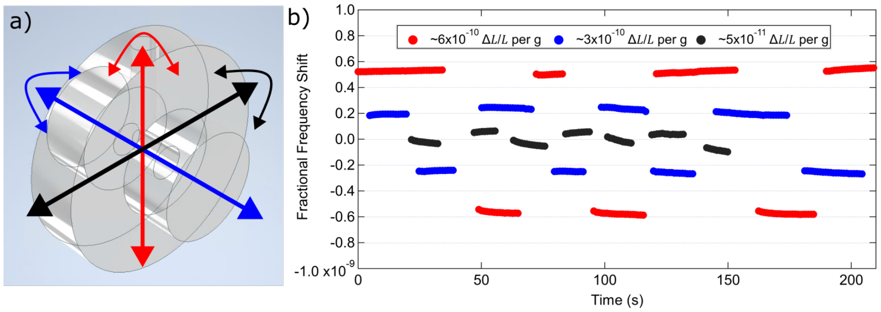

Figure 7.7: a) Diagram of the cavity indicating the mechanical axis along which the cavity is flipped. In the red flip test, the cavity vent hole goes from up to down. In the blue flip test, the optical axis is flipped, and in the black flip test, the mechanical axis which is perpendicular to both the vent hole and the optical beam is flipped. b) Flip test measurements of the primary cavity acceleration sensitivity. The cavity is flipped along three mechanical axes inducing a 2g acceleration change while a laser stays locked to the cavity. The change in frequency is observed. Linear drift, attributed to cavity temperature change, is removed from the data. The worst axis is $6 \times 10^{-10}\frac{\Delta L}{L}$ per g, and this axis corresponds to flipping the vent hole up and down. The asymmetry caused by the vent hole is likely contributing to higher acceleration sensitivity along this axis.

designs to balance these two needs.

For the Yb cavity, I measured acceleration sensitivity using an active vibration isolation table (Herzan TS-150 LP). The mechanical axes can be individually driven while the active isolation is enabled. The mechanical axes are named V, which is the vertical axis aligned roughly with g, H1, which is the horizontal axis aligned with the short side of the TS-150 which is roughly aligned with the optical axis, and H2 which is aligned with the long side of the TS-150. The cavity is mounted so that the four vacuum vent holes are at a 45-degree angle with respect to g. This means that the V and the H2 mechanical axes probe roughly the same mechanical behavior of the cavity due to the cavity symmetry. However, the V axis sees less benefit from the symmetry of the cavity (due to g breaking the symmetry of the acceleration probe) and we expect that it will perform worse as a result.

For each vibration axis V, H1, H2, I modulated the table at 11 Hz and recorded the cavity phase noise, as well as the PSD of the acceleration noise using an accelerometer that was mounted along each of these axes. I also took the same data when no modulation was engaged. Fig. 7.8 shows the phase noise spectrum of an optical beat note between a laser locked to the portable Yb cavity and a low noise reference laser. The phase noise spectrum, even without any modulation, is surprisingly high. This is likely because the phase noise cancellation link is unlocked and adding noise to the reference arm. However, the modulation tones come in above the unmodulated phase noise level so we can live with this level of phase noise for this measurement.

Along the V direction, we can see a clear response at 11 Hz, 33 Hz, and 55 Hz. These harmonics can be used to asses the flatness in the acceleration response because each of these harmonics is also present on the acceleration spectrum. The acceleration sensitivity is 2×10^{-10} at 11 Hz, 33 Hz, and 55 Hz. For the other mechanical axes, it is more difficult to detect harmonics in the phase noise. It would be interesting to revisit this measurement with a lower noise reference arm. The H1 modulation probes along the optical axis. Along the H1 direction, the acceleration sensitivity is $\approx 6{\times}10^{-11} g^{-1}$. This is the lowest acceleration sensitivity response. This is also the axis along which the cavity is suspended by Viton o-rings. There may be some frequency-dependent

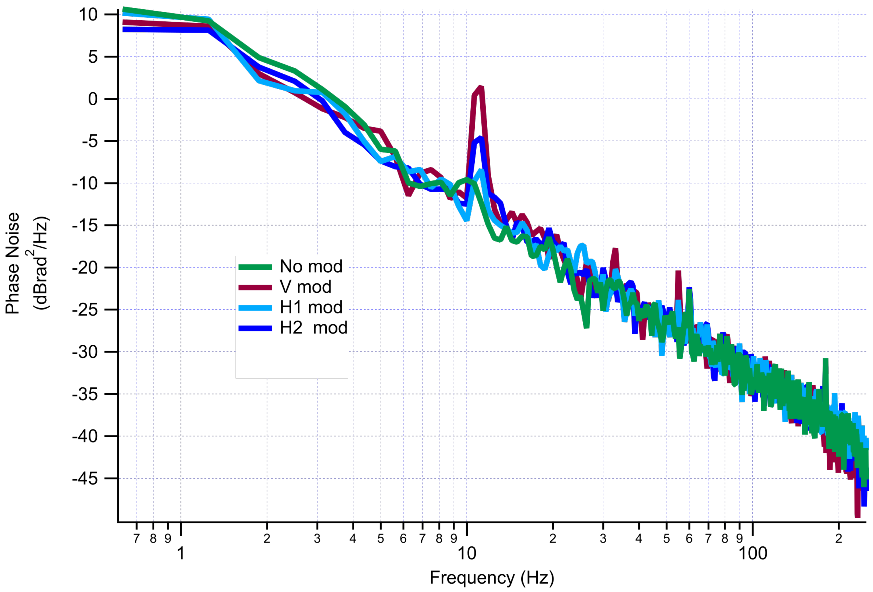

Figure 7.8: Phase noise measurement of the portable Yb cavity against a reference. The reference noise level is significantly above the noise of the portable Yb cavity, but it is low enough to see some phase noise response at the modulation tone for the acceleration sensitivity measurement. The green trace is the phase noise when there is no modulation. The red trace is the V modulation, which is closely aligned with g. The light blue trace is the H1 modulation, which is closely aligned with the optical axis of the cavity. The dark blue trace is the H2 modulation perpendicular to the previous two axes.

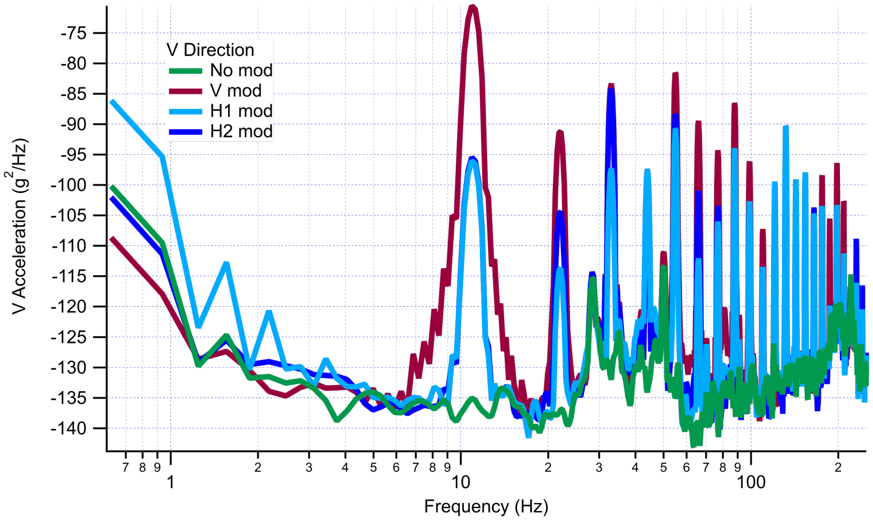

Figure 7.9: The acceleration noise spectrum when the v-direction modulation is engaged. The measurement is taken along all three mechanical axes to confirm the coupling to the other axes is minimal.

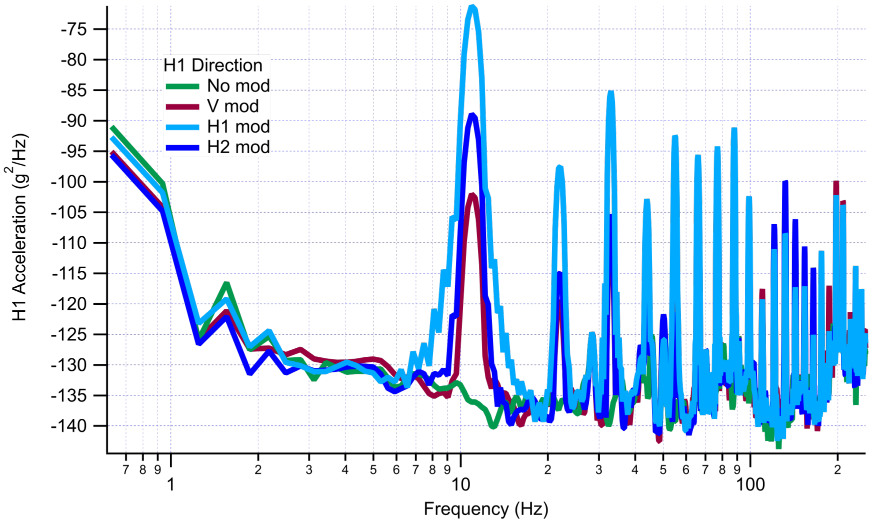

Figure 7.10: The acceleration noise spectrum when the H1-direction modulation is engaged. The measurement is taken along all three mechanical axes to confirm the coupling to the other axes is minimal.

filtering that is caused by these o-rings, but it is too difficult to tell at this time. It would be interesting to repeat the measurement for multiple frequencies. The viton o-rings like have a low mechanical resonance in the 10's of Hz range. Along the H2 direction, the acceleration sensitivity is $\approx 9 \times 10^{-11} g^{-1}$. It would also be interesting to carefully level the platform, rotate the vacuum chamber, and repeat the measurement to see if the second harmonic can be made to be stronger than the first in a symmetry dominated measurement of the acceleration sensitivity. Unfortunately, time constraints, which were worsened by several occurrences of mirror contamination and ion pump death, have made a repeat of this measurement impossible at this time. I have included the preliminary results on this cavity here as a reference for any future grad students who may wish to make similar measurements. Along the H2 direction, the acceleration sensitivity is $\approx 9 \times 10^{-11} g^{-1}$.

To see the acceleration PSD for the modulation applied in the V, H1, and H2 directions, please see Fig. 7.9 Fig. 7.10 and Fig. 7.11. For the phase noise response, please see Fig. 7.8.

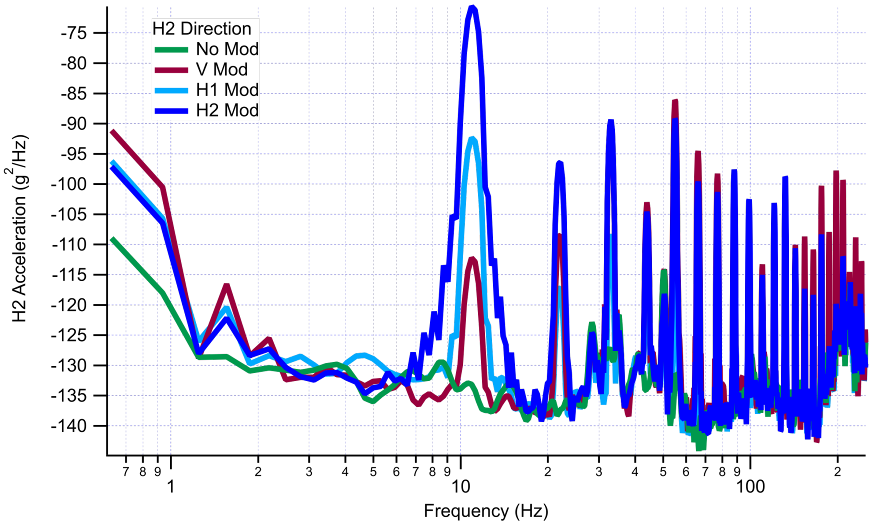

Figure 7.11: The acceleration noise spectrum when the H2-direction modulation is engaged. The measurement is taken along all three mechanical axes to confirm the coupling to the other axes is minimal.

Direction	Acceleration g^2_{rms}/Hz	Phase Noise Level dBrad$^2/Hz$	Acceleration Sensitivity g^{-1}
g-direction / V	8.7×10^{-8}	1.5	2×10^{-10}
g-direction / V 3rd Harmonic	4.7×10^{-9}	-17.7	2×10^{-10}
g-direction / V 5th harmonic	7.0×10^{-9}	-20.7	2×10^{-10}
Optical Axis / H1	7.6×10^{-8}	-8.4	6×10^{-11}
Other Horizontal / H2	8.7×10^{-8}	-4.6	9×10^{-11}

Table 7.1: A table of the values used to calculate the acceleration sensitivity of the portable Yb axis. The acceleration noise spectrum PSD and the phase noise PSD are taken using the same resolution bandwidth, 940 mHz. The height of the peak in the acceleration noise PSD and in the phase noise PSD are entered into columns 2 and 3 and the acceleration sensitivity is calculated using these values. The modulation frequency is 11 Hz. For the V direction modulation, the 3rd and 5th harmonic are also visible on the phase noise PSD and can be used to calculate the acceleration sensitivity.

Chapter 8

Distributed Acoustic Sensing Using Underwater Fiber Optic Cables

The Earth is covered in an underwater fiber-optic cable network thanks to the telecom industry (see Fig. 8.1). These fibers are used to transmit data all over the world, but they also have the potential to operate as remote sensors in parts of the ocean that are difficult to access with traditional measurement devices, such as seismometers. These undersea cables can be used to detect earthquakes [34], observe whales [98], and detect ships [99]. Monitoring of ocean currents, earthquakes, and swells has been demonstrated using both distributed acoustic sensing (DAS) [100, 101], state-of-polarization (SOP)[102, 103, 104], and laser phase interferometry [104, 34].

For laser phase interferometry it is useful have a low noise laser, because the measured signal includes a noise contribution from the reference laser. However, space in a telecom environment comes at a premium. Using large cavities in large enclosures would not be feasible. Compact cavities can offer lower phase noise than unstabilized lasers, and they can be packaged to be compatible with standard telecom racks. To demonstrate the portability and the utility of our cavity stabilised systems, we packed and shipped the ULE-ULE cavity to a telecom fiber launch site (see fig. 8.2 for photos of the system packaging [27]), and made some measurements of the undersea fiber noise.

In early laser phase interferometry demonstrations, the phase of the fiber was integrated over the whole cable length [105]. More recently it was shown it is possible to improve the sensitivity in the submarine cable experiments by taking advantage of the periodic reflections in the telecom cables [104], which are normally used to check on the health of the optical amplifiers. Separate phase tracking in each spans allows for:

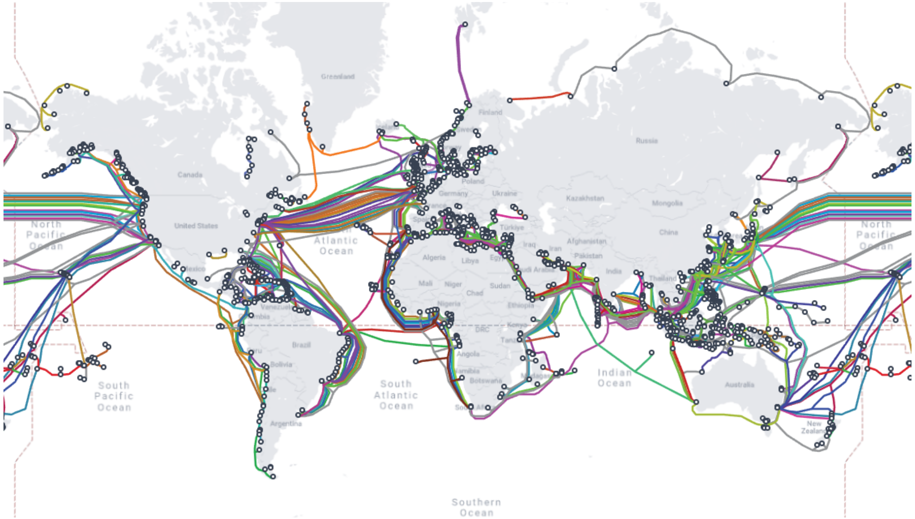
Greenland
Canada
United States
North Pacific Ocean
Atlantic Ocean
Russia
Kazakhstan
Mongolia
China
India
Brazil
South Pacific Ocean
South Atlantic Ocean
Indian Ocean
Australia
Southern Ocean

Figure 8.1: Map of the underwater telecom fibers from TeleGeography [26].

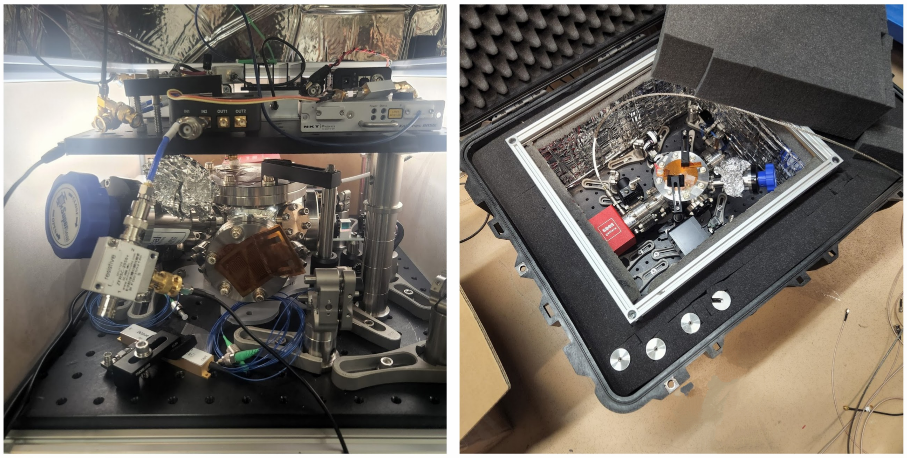

Figure 8.2: Photographs showing packaging and shipping of the ULE-ULE cavity. The free space optical components, fiber components, vacuum can and cavity all fit inside of a box that is 15.7 in x17.7in x14in. This box fits inside of a Pelican shipping case and was mailed to the fiber launch site. A NEG ion pump combo is used to maintain vacuum. The ion pump was not on durring the shipping stages. At the launch site, this box and a few additional microwave components are installed in a standard 18" rack. Further reductions in the volume of the cavity stabilized laser system will be implemented in future demonstrations.

- A lower measurement floor for earthquake detection. The section of the fiber near the shore has a lot of signal from waves and ships (and sometimes road traffic if a section of the fiber is on land), which can hide small earthquake signals. The deep ocean fiber is relatively quiet if treated independently.
- Identification of the approximate location of an earthquake using time of arrival in each fiber span.
- Less stringent requirements on the reference laser. Because the delay time is shorter is a signal span than in the whole length of the fiber, there is more common mode rejection of the reference noise and a noisier reference laser is acceptable.

Given the last point, a commercial laser may be suitable for this technique in many circumstances. However, there are other cases where a local low noise reference laser may be desirable such as time-transfer over a fiber. I will show the fiber noise with and without this separate phase tracking technique. This demonstration shows that our system works in a challenging environment and that the cavity is truly portable.

8.1 Measurement Setup

The fiber cable in this experiment uses pairs of single-mode fiber for bi-directional transmission. It is transatlantic cable connecting North America with Europe. About 80 repeaters are required to amplify the signal and the cable is equipped with high loss loop-back configurations in each repeater, allowing backscattered light from the forward transmission span to be coupled into the fiber going to the opposite direction.

For a schematic of the parts involved in the measurement, please see Fig. 8.3. Light from the cavity stabilized laser is split and half is sent into a single sideband EOM that applies a sawtooth frequency sweep. Then the light is sent into the fiber in the ocean. At each repeater, a small fraction of the light is sent back to the launch site in the parallel fiber. This light is then combined with a portion of the original reference light and detected. Because of the frequency sweep and

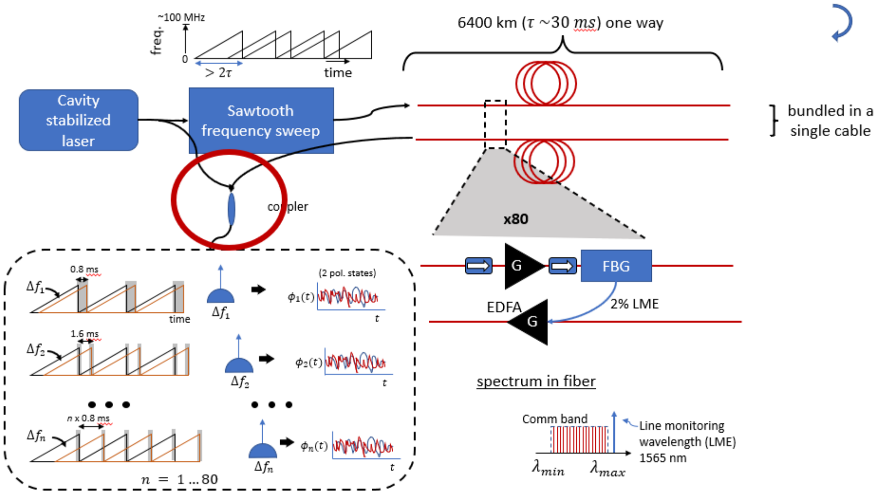
~100 MHz
freq.
0
> 2τ
time
6400 km (τ ~30 ms) one way
Cavity stabilized laser
Sawtooth frequency sweep
bundled in a single cable
coupler
x80
G
FBG
EDFA
G
2% LME
0.8 ms
Δf₁
time
(2 pol. states)
φ₁(τ)
τ
1.6 ms
Δf₂
φ₂(τ)
n x 0.8 ms
Δfₙ
φₙ(τ)
n = 1…80
spectrum in fiber
Comm band
Line monitoring wavelength (LME) 1565 nm
λmin
λmax

Figure 8.3: Light from the cavity stabilized laser is sent through a single side band EOM which applies a sawtooth frequency sweep (there are actually two polarization channels each with separate sawtooth frequency sweeps - these channels can be separated at the end). The fiber is then sent under the Atlantic ocean. There are periodic erbium-doped fiber amplifiers (EDFA) which are followed by fiber Bragg gratings which send a small portion of the line monitoring signal backwards through a separate fiber. This signal is normally used to check the health of the amplifiers, but can be used for our purposes as the sensing light. Back at the launch site, the return signal is combined with a portion of the cavity stabilized light before frequency modulation, detected, and digitally demodulated. For details on the signal acquisition please see Mazur et al. [27]

the different time delays, each reflection is represented with a separate microwave frequency tone. These tones are digitally demodulated in using a special FPGA-based processing system that is real-time capable and allows coherent tracking of the phase and amplitude of each polarization state of every tone. For the purposes of this chapter, we are interested in the phase changes of each reflector and we ignore the separate polarization state tracking.

8.2 Fiber Frequency Noise Measurement

The frequency noise measured at the detector, $S_{\nu,measured}$, contains both the acoustic noise of the fiber, $S_{\nu,fiber}$, which is essentially the signal in this experiment, and a contribution of the laser reference noise, $S_{\nu,ref}$:

$$S_{\nu,measured} = S_{\nu,fiber} + S_{\nu,ref}. \tag{8.1}$$

The reference noise contribution is related to the frequency noise noise of laser, $S_{f,laser}$, the laser RIN, and the time delay in the fiber [106].

Unfortunately, there is easy no way at the fiber launch site at this time to make a direct measurement of the laser noise. Space is limited and bringing a separate reference of similar or lower noise level to compare against would be challenging. The telecom environment is very loud with many air conditioning systems running at once. It is very possible that the frequency noise of the cavity stabilized laser that we measured in the lab is lower than the frequency noise of the cavity stabilized laser in this environment. To get a sense of the improvement that the cavity stabilized laser might offer, we looked at the frequency noise of each reflector (after the first 10, which have been removed) shown in Fig. 8.4 for both a commercially available etalon stabilized laser and the compact cavity stabilized laser. In this plot, the phase of the previous reflector has not been subtracted. We are looking at the noise accumulated up to that point for each reflector. These frequency noise measurements cannot be made simultaneously so the fiber noise contribution may be different between the commercial system and our compact cavity system measurements. However, by looking at the frequency noise of the reflected signals, we can draw some conclusions about the upper limits of the reference laser noise. It does seem like the measurement may be reference limited above 100 Hz, where the cavity stabilized laser outperforms the commercially available system. Note that at the low frequency end, there is little variation between the spans with either laser. This is because the noise in the first few reflectors is dominating and the further spans are not contributing much.

Fig. 8.5 shows the phase in each reflector and the phase difference for each reflector (except for the first 10 reflectors, which have been removed from the data). By removing the phase of the previous reflector, we can see what the phase change is within a single span of the fiber instead of the cumulative noise up to that reflector. The frequency noise of each span (except for the first 10, which have been removed) after taking this phase difference is shown in Fig. 8.6. This is the same data that was used to calculate the frequency noise in Fig. 8.4, but see much greater sensitivity from 1 Hz-10 Hz for both laser systems. The measurements deeper in the ocean are now less affected by the acoustic noise in the fiber near the shore, which is typically worse due to shallower depths and greater sensitivity to ships and waves. This is important when looking for quieter signals such as small earthquakes deep in the ocean. However, the frequency noise could still dominated by fiber noise at low frequency offsets, so it is too difficult to say if the cavity stabilized laser is providing much advantage at frequencies below 100 Hz. Most of the interesting signals when it comes to waves, ships and earthquakes are below 100 Hz so it is still an open question if the cavity stabilized provides any enhancement for these measurements. However, from 100 Hz-10 kHz the measurement appears to be laser noise limited and the cavity stabilized laser is quieter. The dips in the noise starting around 1 kHz offset are indicative of reference noise limited performance. These dips occur when the frequency offset is $1/\tau$. They occur because at this frequency, laser noise becomes strongly correlated and has greater rejection [106].

Although it is an open question as to whether or not the cavity stabilized laser offers much improvement to this application, we are satisfied that we were able to ship the system and run the laser remotely. There are other applications, like time transfer using fiber, that may benefit from having low noise frequency references in similar environments.

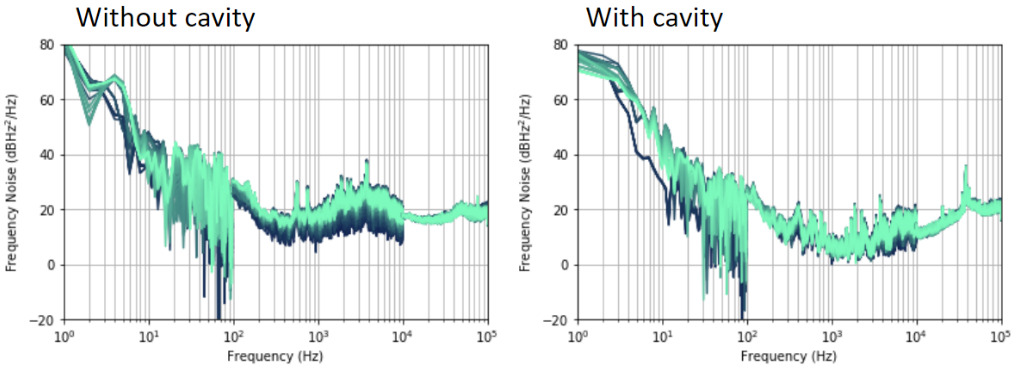

Figure 8.4: Plots of the frequency noise of each reflector. The color indicates the closeness of the detector with dark navy representing detectors that are close to the fiber launch and light teal representing detectors that are further away. The right plot shows the measurement made using a commercial etalon stabilized laser. The left plot shows the fiber noise measurement using our cavity stabilized laser. These measurements were made at different times, so it is possible that the fiber noise changed in between these measurements. However, it does look like there may be some reference-limited noise above 100 Hz. In this region, the cavity stabilized laser looks like it would be a better choice as a reference laser. Note that at the low frequency end, there is little variation between the spans with either laser. This is because the noise in the first few reflectors is dominating and the further spans are not contributing much.

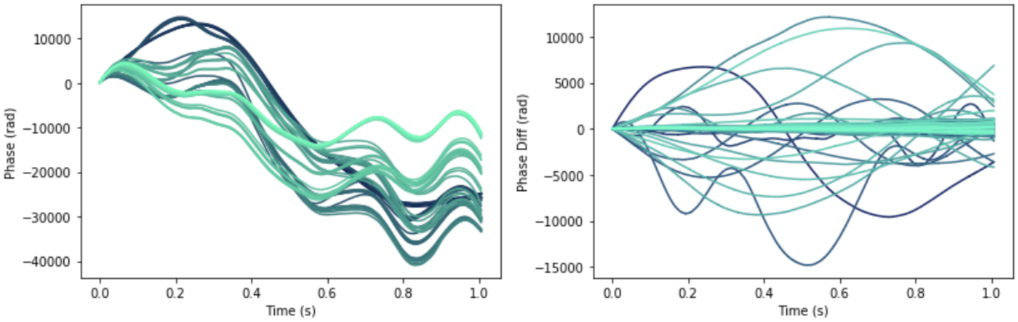

Figure 8.5: Phase vs time for each reflector. The color indicates the closeness of the detector with dark navy representing detectors that are close to the fiber launch and light teal representing detectors that are further away.

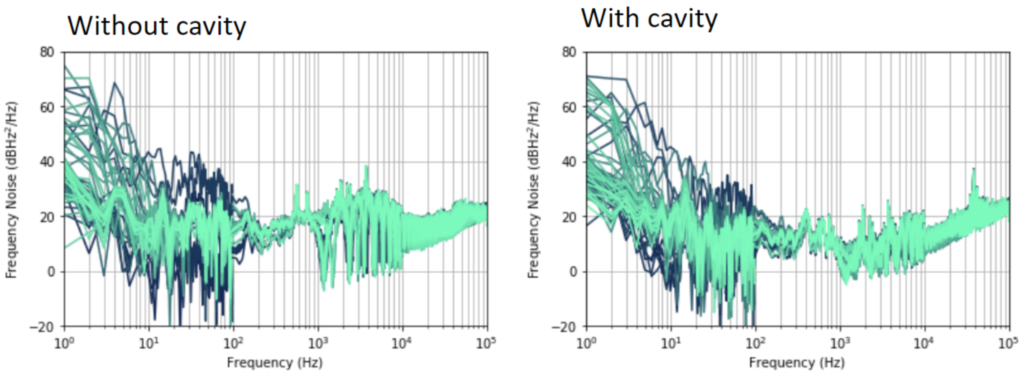
Without cavity

With cavity

Figure 8.6: A comparison of the noise spectrum measured with a commercial available etalon stabilized laser vs the compact cavity stabilized laser. Below 100 Hz, no obvious improvement to the noise can be identified when comparing the two systems. Some bands look quieter, but hard to make a conclusion knowing that the fiber noise may be different in the two measurements. From 100 Hz – 10 KHz, we see an improvement in the noise. However, above 1 kHz, both systems appear to be limited by laser noise, though the cavity stabilized noise level appears lower. The color indicates the closeness of the detector with dark navy representing detectors that are close to the fiber launch and light teal representing detectors that are further away.

Chapter 9

Conclusions

The pursuit of portable vacuum-gap reference cavities arises from the need for rigid, compact, and robust laser frequency stabilization solutions in demanding and unpredictable environments. Many applications, such as portable optical atomic clocks, earthquake detection using undersea optical fiber, and low phase noise microwave generation, require the sub-10^{-13} stability available in the optical domain, but the size, weight, and infrastructure demands of large or cryogenic cavity systems are incompatible with these applications. To address these challenges, I designed and developed three compact optical cavities. These designs represent promising steps towards achieving high stability performance while overcoming the limitations of traditional cavity systems, thereby opening up new possibilities for practical applications that require precise and portable laser frequency references.

The first design involves a series of two cavities with 6.3 mm long spacers, specifically tailored for low phase noise microwave generation. These cavities offer compactness while aiming to maintain high stability levels. We have demonstrated a compact optical frequency reference cavity design, with a cavity volume of 5.2 mL, compatible with out-of-the-lab applications which can support ultralow noise microwave generation through OFD. The design uses a simple cylindrical geometry for ease of manufacturing and is rigidly held. Using a frequency-locking technique utilizing EOM feedback with >1 MHz bandwidth, we demonstrated near thermal noise-limited optical phase noise performance, reaching nearly -110 dBc/Hz at 10 kHz offset. Despite the higher thermal noise floor resulting from its compact size, this system provides one of the lowest phase noise results at 10 kHz offset for any optical reference cavity of which we are aware. For larger offsets, the noise remains below -100 dBc/Hz. Moreover, the cavity demonstrated near thermal noise limited fractional frequency stability of 2×10^{-14} at 0.1 s. A lower frequency drift rate was achieved with an all-ULE cavity variation of the design.

Additionally, a low holding force sensitivity of the cavity was measured, demonstrating agreement with simulations. Importantly, the holding force sensitivity showed minimal dependence on the holding radius. Measurements of the acceleration sensitivity ranged from $\sim 6 \times 10^{-10} g^{-1}$ for the cavity's mechanical axis that displays the largest asymmetry to $\sim 5 \times 10^{-11} g^{-1}$ for the least sensitive mechanical axis. This low acceleration sensitivity was achieved with a simple holding geometry and minimal alignment of the cavity into the mount.

Further improvements to the cavity performance are straightforward. The acceleration sensitivity can be reduced by implementing a more symmetric vent hole pattern in the cavity spacer. An all-ULE version of the 12.7 mm cavity design could combine the low dependence of the holding force diameter with low frequency drift (at a minimal cost to the low phase noise). With its demonstrated low noise performance, our cavity design fills an important gap in the performance-size trade space, enabling compact out-of-the-lab systems with improved phase and frequency stability.

The second design targets a portable Yb lattice clock, featuring an optical cavity with a 25 mm long spacer, with four symmetric vent holes. This cavity has a calculated thermal noise limited fractional frequency instability of $\approx 10^{-15}$. The design is highly-symmetric, and the acceleration sensitivity is better than 2×10^{-10} per g along all mechanical axes. Preliminary phase noise measurements show more than 90 dB suppression of the free running laser noise, and thermal noise limited performance between 1 and 10 Hz. Preliminary measurement of the ADEV show that the laser lock is likely suffering from residual amplitude modulation (RAM) noise and drifting due to temperature. Further efforts are needed to improve the long-term stability of the cavity, but the remaining challenges are technical and not fundamental.

9.1 Future Outlook

The field trial of the ULE-ULE cavity at the fiber launch site demonstrates the increasing portability of compact vacuum gap Fabry-Pérot cavities. The entire system fits into an 18” telecom rack and can be operated remotely. The laser effectively locked onto the cavity despite significant environmental acoustic noise.

Cavity mirrors can now be made using lithographic techniques [41] and that these cavities can even be integrated with waveguide-based lasers [42]. The size, weight, and portability of these vacuum-gap Fabry-Perot resonators is only improving. Further, a recent vacuum-bonded cavity demonstration shows potential to eliminate the need for bulky vacuum cans and ion pumps [43].

The ULE-ULE cavity was recently employed for generating low-noise microwaves via two-point optical frequency division, utilizing self-injection locked integrated lasers and a microcomb [40]. As these systems continue get smaller and more portable, I expect we will see them integrated into more applications, especially those that require low phase noise microwaves.

Bibliography

[1] J. Davila-Rodriguez, F. N. Baynes, A. D. Ludlow, T. M. Fortier, H. Leopardi, S. A. Diddams, and F. Quinlan. Compact, thermal-noise-limited reference cavity for ultra-low-noise microwave generation. Opt. Lett., 42(7):1277–1280, Apr 2017.

[2] Garrett D. Cole, Wei Zhang, Michael J. Martin, Jun Ye, and Markus Aspelmeyer. Tenfold reduction of brownian noise in high-reflectivity optical coatings. Nature Photonics, 7(8):644–650, July 2013.

[3] Stephen Webster and Patrick Gill. Force-insensitive optical cavity. Opt. Lett., 36(18):3572–3574, Sep 2011.

[4] David R. Leibrandt, Michael J. Thorpe, Mark Notcutt, Robert E. Drullinger, Till Rosenband, and James C. Bergquist. Spherical reference cavities for frequency stabilization of lasers in non-laboratory environments. Opt. Express, 19(4):3471–3482, Feb 2011.

[5] David R. Leibrandt, James C. Bergquist, and Till Rosenband. Cavity-stabilized laser with acceleration sensitivity below 10^{-12} g^{-1}. Phys. Rev. A, 87:023829, Feb 2013.

[6] A. D. Ludlow, X. Huang, M. Notcutt, T. Zanon-Willette, S. M. Foreman, M. M. Boyd, S. Blatt, and J. Ye. Compact, thermal-noise-limited optical cavity for diode laser stabilization at 1×10–15. Opt. Lett., 32(6):641–643, Mar 2007.

[7] B. Argence, E. Prevost, T. Lévèque, R. Le Goff, S. Bize, P. Lemonde, and G. Santarelli. Prototype of an ultra-stable optical cavity for space applications. Opt. Express, 20(23):25409–25420, Nov 2012.

[8] Dariusz Świerad, Sebastian Häfner, Stefan Vogt, Bertrand Venon, David Holleville, Sébastien Bize, André Kulosa, Sebastian Bode, Yeshpal Singh, Kai Bongs, Ernst Maria Rasel, Jérôme Lodewyck, Rodolphe Le Targat, Christian Lisdat, and Uwe Sterr. Ultra-stable clock laser system development towards space applications. Scientific Reports, 6(1):33973, Sep 2016.

[9] T. Kessler, C. Hagemann, C. Grebing, T. Legero, U. Sterr, F. Riehle, M. J. Martin, L. Chen, and J. Ye. A sub-40-mhz-linewidth laser based on a silicon single-crystal optical cavity. Nature Photonics, 6(10):687–692, Oct 2012.

[10] D. G. Matei, T. Legero, S. Häfner, C. Grebing, R. Weyrich, W. Zhang, L. Sonderhouse, J. M. Robinson, J. Ye, F. Riehle, and U. Sterr. 1.5 μm lasers with sub-10 mhz linewidth. Phys. Rev. Lett., 118:263202, Jun 2017.

[11] B. C. Young, F. C. Cruz, W. M. Itano, and J. C. Bergquist. Visible lasers with subhertz linewidths. Phys. Rev. Lett., 82:3799–3802, May 1999.

[12] Y. Y. Jiang, A. D. Ludlow, N. D. Lemke, R. W. Fox, J. A. Sherman, L.-S. Ma, and C. W. Oates. Making optical atomic clocks more stable with 1016-level laser stabilization. Nature Photonics, 5(3):158–161, Mar 2011.

[13] M. Schioppo, R. C. Brown, W. F. McGrew, N. Hinkley, R. J. Fasano, K. Beloy, T. H. Yoon, G. Milani, D. Nicolodi, J. A. Sherman, N. B. Phillips, C. W. Oates, and A. D. Ludlow. Ultrastable optical clock with two cold-atom ensembles. Nature Photonics, 11(1):48–52, Jan 2017.

[14] Michael J. Martin. Quantum metrology and many-body physics: Pushing the frontier of the optical lattice clock. PhD thesis, 2013.

[15] Sebastian Häfner, Stephan Falke, Christian Grebing, Stefan Vogt, Thomas Legero, Mikko Merimaa, Christian Lisdat, and Uwe Sterr. 8×10^{-17} fractional laser frequency instability with a long room-temperature cavity. Opt. Lett., 40(9):2112–2115, May 2015.

[16] L. M. Baumgartel, R. J. Thompson, and N. Yu. Frequency stability of a dual-mode whispering gallery mode optical reference cavity. Opt. Express, 20(28):29798–29806, Dec 2012.

[17] Liron Stern, Wei Zhang, Lin Chang, Joel Guo, Chao Xiang, Minh A Tran, Duanni Huang, Jonathan D Peters, David Kinghorn, John E Bowers, et al. Ultra-precise optical-frequency stabilization with heterogeneous III–V/Si lasers. Optics Letters, 45(18):5275–5278, 2020.

[18] Hansuek Lee, Myoung-Gyun Suh, Tong Chen, Jiang Li, Scott A. Diddams, and Kerry J. Vahala. Spiral resonators for on-chip laser frequency stabilization. Nature Communications, 4(1), 2013.

[19] Wei Zhang, Fred Baynes, Scott A Diddams, and Scott B Papp. Microrod optical frequency reference in the ambient environment. Physical Review Applied, 12(2):024010, 2019.

[20] William Loh, Jules Stuart, David Reens, Colin D Bruzewicz, Danielle Braje, John Chiaverini, Paul W Juodawlkis, Jeremy M Sage, and Robert McConnell. Operation of an optical atomic clock with a Brillouin laser subsystem. Nature, 588(7837):244–249, 2020.

[21] Janis Alnis, Albert Schliesser, Christine Y Wang, Johannes Hofer, Tobias J Kippenberg, and TW Hänsch. Thermal-noise-limited crystalline whispering-gallery-mode resonator for laser stabilization. Physical Review A, 84(1):011804, 2011.

[22] Megan L. Kelleher, Charles A. McLemore, Dahyeon Lee, Josue Davila-Rodriguez, Scott A. Diddams, and Franklyn Quinlan. Compact, portable, thermal-noise-limited optical cavity with low acceleration sensitivity. Opt. Express, 31(7):11954–11965, Mar 2023.

[23] Xiaopeng Xie, Romain Bouchand, Daniele Nicolodi, Michele Giunta, Wolfgang Hänsel, Matthias Lezius, Abhay Joshi, Shubhashish Datta, Christophe Alexandre, Michel Lours, Pierre-Alain Tremblin, Giorgio Santarelli, Ronald Holzwarth, and Yann Le Coq. Photonic microwave signals with zeptosecond-level absolute timing noise. Nature Photonics, 11(1):44–47, Jan 2017.

[24] Fred N. Baynes, Franklyn Quinlan, Tara M. Fortier, Qiugui Zhou, Andreas Beling, Joe C. Campbell, and Scott A. Diddams. Attosecond timing in optical-to-electrical conversion. Optica, 2(2):141–146, Feb 2015.

[25] Enrico Rubiola and Francois Vernotte. The cross-spectrum experimental method. arXiv.1003.0113, 2010.

[26] https://www.submarinecablemap.com/.

[27] Mikael Mazur, Nicolas K. Fontaine, Megan Kelleher, Valey Kamalov, Roland Ryf, Lauren Dallachiesa, Haoshuo Chen, David T. Neilson, and Franklyn Quinlan. Advanced distributed submarine cable monitoring and environmental sensing using constant power probe signals and coherent detection, 2023.

[28] Fritz Riehle, Patrick Gill, Felicitas Arias, and Lennart Robertsson. The CIPM list of recommended frequency standard values: guidelines and procedures. Metrologia, 55(2):188, feb 2018.

[29] Kyle Beloy, Martha I. Bodine, Tobias Bothwell, Samuel M. Brewer, Sarah L. Bromley, Jwo-Sy Chen, Jean-Daniel Deschênes, Scott A. Diddams, Robert J. Fasano, Tara M. Fortier, Youssef S. Hassan, David B. Hume, Dhruv Kedar, Colin J. Kennedy, Isaac Khader, Amanda Koepke, David R. Leibrandt, Holly Leopardi, Andrew D. Ludlow, William F. McGrew, William R. Milner, Nathan R. Newbury, Daniele Nicolodi, Eric Oelker, Thomas E. Parker, John M. Robinson, Stefania Romisch, Stefan A. Schäffer, Jeffrey A. Sherman, Laura C. Sinclair, Lindsay Sonderhouse, William C. Swann, Jian Yao, Jun Ye, and Xiaogang Zhang. Frequency ratio measurements at 18-digit accuracy using an optical clock network. Nature, 591(7851):564–569, Mar 2021.

[30] Miguel Dovale Álvarez. Optical cavities for optical atomic clocks, atom interferometry and gravitational-wave detection. Springer, 2019.

[31] Josep Sanjuan, Klaus Abich, Martin Gohlke, Andreas Resch, Thilo Schuldt, Timm Wegehaupt, Geoffrey P. Barwood, Patrick Gill, and Claus Braxmaier. Long-term stable optical cavity for special relativity tests in space. Opt. Express, 27(25):36206–36220, Dec 2019.

[32] J. Zhang, W. Wu, X. H. Shi, X. Y. Zeng, K. Deng, and Z. H. Lu. Design verification of large time constant thermal shields for optical reference cavities. Review of Scientific Instruments, 87(2):023104, 2016.

[33] Andrew D. Ludlow, Martin M. Boyd, Jun Ye, E. Peik, and P. O. Schmidt. Optical atomic clocks. Rev. Mod. Phys., 87:637–701, Jun 2015.

[34] Giuseppe Marra, Cecilia Clivati, Richard Luckett, Anna Tampellini, Jochen Kronjäger, Louise Wright, Alberto Mura, Filippo Levi, Stephen Robinson, André Xuereb, Brian Baptie, and Davide Calonico. Ultrastable laser interferometry for earthquake detection with terrestrial and submarine cables. Science, 361(6401):486–490, 2018.

[35] T. M. Fortier, M. S. Kirchner, F. Quinlan, J. Taylor, J. C. Bergquist, T. Rosenband, N. Lemke, A. Ludlow, Y. Jiang, C. W. Oates, and S. A. Diddams. Generation of ultrastable microwaves via optical frequency division. Nature Photonics, 5(7):425–429, Jul 2011.

[36] Lisheng Chen, John L. Hall, Jun Ye, Tao Yang, Erjun Zang, and Tianchu Li. Vibration-induced elastic deformation of Fabry-Pérot cavities. Phys. Rev. A, 74:053801, Nov 2006.

[37] Alexandre Didier, Jacques Millo, Baptiste Marechal, Cyrus Rocher, Enrico Rubiola, Roméo Lecomte, Morvan Ouisse, Jérôme Delporte, Clément Lacroûte, and Yann Kersalé. Ultracompact reference ultralow expansion glass cavity. Appl. Opt., 57(22):6470–6473, Aug 2018.

[38] Sofia Herbers, Sebastian Häfner, Sören Dörscher, Tim Lücke, Uwe Sterr, and Christian Lisdat. Transportable clock laser system with an instability of 1.6×10^{-16}. Opt. Lett., 47(20):5441–5444, Oct 2022.

[39] Charles A. McLemore, Naijun Jin, Megan L. Kelleher, James P. Hendrie, David Mason, Yizhi Luo, Dahyeon Lee, Peter Rakich, Scott A. Diddams, and Franklyn Quinlan. Miniaturizing ultrastable electromagnetic oscillators: Sub-10^{-14} frequency instability from a centimeter-scale Fabry-Pérot cavity. Phys. Rev. Applied, 18:054054, Nov 2022.

[40] Igor Kudelin, William Groman, Qing-Xin Ji, Joel Guo, Megan L. Kelleher, Dahyeon Lee, Takuma Nakamura, Charles A. McLemore, Pedram Shirmohammadi, Samin Hanifi, Haotian Cheng, Naijun Jin, Sam Halliday, Zhaowei Dai, Lue Wu, Warren Jin, Yifan Liu, Wei Zhang, Chao Xiang, Vladimir Iltchenko, Owen Miller, Andrey Matsko, Steven Bowers, Peter T. Rakich, Joe C. Campbell, John E. Bowers, Kerry Vahala, Franklyn Quinlan, and Scott A. Diddams. Photonic chip-based low noise microwave oscillator, 2023.

[41] Naijun Jin, Charles A. McLemore, David Mason, James P. Hendrie, Yizhi Luo, Megan L. Kelleher, Prashanta Kharel, Franklyn Quinlan, Scott A. Diddams, and Peter T. Rakich. Micro-fabricated mirrors with finesse exceeding one million. Optica, 9(9):965–970, Sep 2022.

[42] Joel Guo, Charles A. McLemore, Chao Xiang, Dahyeon Lee, Lue Wu, Warren Jin, Megan Kelleher, Naijun Jin, David Mason, Lin Chang, Avi Feshali, Mario Paniccia, Peter T. Rakich, Kerry J. Vahala, Scott A. Diddams, Franklyn Quinlan, and John E. Bowers. Chip-based laser with 1-hertz integrated linewidth. Science Advances, 8(43):eabp9006, 2022.

[43] Yifan Liu, Charles McLemore, Megan Kelleher, Dahyeon Lee, Takuma Nakamura, Naijun Jin, Susan Schima, Peter Rakich, Scott Diddams, and Franklyn Quinlan. Thermal-noise-limited, compact optical reference cavity operated without a vacuum enclosure. 7 2023.

[44] A. Gillespie and F. Raab. Thermally excited vibrations of the mirrors of laser interferometer gravitational-wave detectors. Phys. Rev. D, 52:577–585, Jul 1995.

[45] Peter R. Saulson. Thermal noise in mechanical experiments. Phys. Rev. D, 42:2437–2445, Oct 1990.

[46] Herbert B. Callen and Theodore A. Welton. Irreversibility and generalized noise. Phys. Rev., 83:34–40, Jul 1951.

[47] Yu. Levin. Internal thermal noise in the ligo test masses: A direct approach. Phys. Rev. D, 57:659–663, Jan 1998.

[48] Thomas Kessler, Thomas Legero, and Uwe Sterr. Thermal noise in optical cavities revisited. J. Opt. Soc. Am. B, 29(1):178–184, Jan 2012.

[49] Kenji Numata, Amy Kemery, and Jordan Camp. Thermal-noise limit in the frequency stabilization of lasers with rigid cavities. Phys. Rev. Lett., 93:250602, Dec 2004.

[50] François Bondu, Patrice Hello, and Jean-Yves Vinet. Thermal noise in mirrors of interferometric gravitational wave antennas. Physics Letters A, 246(3):227–236, 1998.

[51] Yuk Tung Liu and Kip Thorne. Thermoelastic noise and homogeneous thermal noise in finite sized gravitational-wave test masses. Physical Review D, 62, 11 2000.

[52] Dhruv Kedar, Jialiang Yu, Eric Oelker, Alexander Staron, William R. Milner, John M. Robinson, Thomas Legero, Fritz Riehle, Uwe Sterr, and Jun Ye. Frequency stability of cryogenic silicon cavities with semiconductor crystalline coatings. Optica, 10(4):464–470, Apr 2023.

[53] M. Cerdonio, L. Conti, A. Heidmann, and M. Pinard. Thermoelastic effects at low temperatures and quantum limits in displacement measurements. Phys. Rev. D, 63:082003, Mar 2001.

[54] Eric D. Black, Akira Villar, and Kenneth G. Libbrecht. Thermoelastic-damping noise from sapphire mirrors in a fundamental-noise-limited interferometer. Phys. Rev. Lett., 93:241101, Dec 2004.

[55] M. Evans, S. Ballmer, M. Fejer, P. Fritschel, G. Harry, and G. Ogin. Thermo-optic noise in coated mirrors for high-precision optical measurements. Phys. Rev. D, 78:102003, Nov 2008.

[56] R. W. P. Drever, J. L. Hall, F. V. Kowalski, J. Hough, G. M. Ford, A. J. Munley, and H. Ward. Laser phase and frequency stabilization using an optical resonator. Applied Physics B, 31(2):97–105, Jun 1983.

[57] Eric D. Black. An introduction to Pound–Drever–Hall laser frequency stabilization. American Journal of Physics, 69(1):79–87, 2001.

[58] Xiaohui Shi, Jie Zhang, Xiaoyi Zeng, Xiaolong Lü, Kui Liu, Jing Xi, Yanxia Ye, and Zehuang Lu. Suppression of residual amplitude modulation effects in pound–drever–hall locking. Applied Physics B, 124(8):153, Jul 2018.

[59] François Bondu and Olivier Debieu. Accurate measurement method of fabry-perot cavity parameters via optical transfer function. Appl. Opt., 46(14):2611–2614, May 2007.

[60] Christina J. Hood, H. J. Kimble, and Jun Ye. Characterization of high-finesse mirrors: Loss, phase shifts, and mode structure in an optical cavity. Phys. Rev. A, 64:033804, Aug 2001.

[61] N. C. Wong and J. L. Hall. Servo control of amplitude modulation in frequency-modulation spectroscopy: demonstration of shot-noise-limited detection. J. Opt. Soc. Am. B, 2(9):1527–1533, Sep 1985.

[62] Fabian Schmid, Johannes Weitenberg, Theodor W. Hänsch, Thomas Udem, and Akira Ozawa. Simple phase noise measurement scheme for cavity-stabilized laser systems. Opt. Lett., 44(11):2709–2712, Jun 2019.

[63] Ping Lu, Nageswara Lalam, Mudabbir Badar, Bo Liu, Benjamin T. Chorpening, Michael P. Buric, and Paul R. Ohodnicki. Distributed optical fiber sensing: Review and perspective. Applied Physics Reviews, 6(4):041302, 2019.

[64] Leilei Shi, Tao Zhu, Qian He, and Shihong Huang. Effect of laser linewidth on phase-OTDR based distributed vibration sensing regime. In José M. López-Higuera, Julian D. C. Jones, Manuel López-Amo, and José Luis Santos, editors, 22rd International Conference on Optical Fibre Sensors, volume 9156, page 91575H. International Society for Optics and Photonics, SPIE, 2013.

[65] J.C. Juarez, E.W. Maier, Kyoo Nam Choi, and H.F. Taylor. Distributed fiber-optic intrusion sensor system. Journal of Lightwave Technology, 23(6):2081–2087, 2005.

[66] F. Bondu, P. Fritschel, C. N. Man, and A. Brillet. Ultrahigh-spectral-purity laser for the VIRGO experiment. Opt. Lett., 21(8):582–584, Apr 1996.

[67] Kaikai Liu, Nitesh Chauhan, Jiawei Wang, Andrei Isichenko, Grant M. Brodnik, Paul A. Morton, Ryan O. Behunin, Scott B. Papp, and Daniel J. Blumenthal. 36 hz integral linewidth laser based on a photonic integrated 4.0 m coil resonator. Optica, 9(7):770–775, Jul 2022.

[68] W. Liang, V. S. Ilchenko, D. Eliyahu, A. A. Savchenkov, A. B. Matsko, D. Seidel, and L. Maleki. Ultralow noise miniature external cavity semiconductor laser. Nature Communications, 6(1):7371, Jun 2015.

[69] Robert Fasano. A Transportable Ytterbium Optical Lattice Clock. PhD thesis, CU Boulder, 2021.

[70] Eugen Wiens and Stephan Schiller. Simulation of force-insensitive optical cavities in cubic spacers. Applied Physics B, 124(7), 2018.

[71] Richard W. Fox. Temperature analysis of low-expansion Fabry-Pérot cavities. Opt. Express, 17(17):15023–15031, Aug 2009.

[72] Thomas Legero, Thomas Kessler, and Uwe Sterr. Tuning the thermal expansion properties of optical reference cavities with fused silica mirrors. J. Opt. Soc. Am. B, 27(5):914–919, May 2010.

[73] T. Nazarova, F. Riehle, and U. Sterr. Vibration-insensitive reference cavity for an ultra-narrow-linewidth laser. Applied Physics B, 83(4):531–536, 2006.

[74] S J Waldman. Ray optics calculations of alignment matrices, LIGO-T0900647-02-I, Dec 2009.

[75] Mamoru Endo and Thomas R. Schibli. Residual phase noise suppression for Pound-Drever-Hall cavity stabilization with an electro-optic modulator. OSA Continuum, 1(1):116–123, Sep 2018.

[76] J. L. Hall and T. W. Hänsch. External dye-laser frequency stabilizer. Opt. Lett., 9(11):502–504, Nov 1984.

[77] Jeff A. Sherman and Robert Jördens. Oscillator metrology with software defined radio. Review of Scientific Instruments, 87(5):054711, 2016.

[78] V.B. Braginsky, M.L. Gorodetsky, and S.P. Vyatchanin. Thermo-refractive noise in gravitational wave antennae. Physics Letters A, 271(5):303–307, 2000.

[79] Kenji Numata, Masaki Ando, Kazuhiro Yamamoto, Shigemi Otsuka, and Kimio Tsubono. Wide-band direct measurement of thermal fluctuations in an interferometer. Phys. Rev. Lett., 91:260602, Dec 2003.

[80] Mark Notcutt, Long-Sheng Ma, Andrew D. Ludlow, Seth M. Foreman, Jun Ye, and John L. Hall. Contribution of thermal noise to frequency stability of rigid optical cavity via hertz-linewidth lasers. Phys. Rev. A, 73:031804, Mar 2006.

[81] Steven Peil, James L Hanssen, Thomas B Swanson, Jennifer Taylor, and Christopher R Ekstrom. Evaluation of long term performance of continuously running atomic fountains. Metrologia, 51(3):263, may 2014.

[82] M Schioppo, RC Brown, WF McGrew, N Hinkley, RJ Fasano, K Beloy, TH Yoon, G Milani, D Nicolodi, JA Sherman, et al. Ultrastable optical clock with two cold-atom ensembles. Nature Photonics, 11(1):48–52, 2017.

[83] May E Kim, William F McGrew, Nicholas V Nardelli, Ethan R Clements, Youssef S Hassan, Xiaogang Zhang, Jose L Valencia, Holly Leopardi, David B Hume, Tara M Fortier, et al. Improved interspecies optical clock comparisons through differential spectroscopy. Nature Physics, pages 1–5, 2022.

[84] WF McGrew, X Zhang, RJ Fasano, SA Schäffer, K Beloy, D Nicolodi, RC Brown, N Hinkley, G Milani, M Schioppo, et al. Atomic clock performance enabling geodesy below the centimetre level. Nature, 564(7734):87–90, 2018.

[85] Tobias Bothwell, Dhruv Kedar, Eric Oelker, John M Robinson, Sarah L Bromley, Weston L Tew, Jun Ye, and Colin J Kennedy. Jila sri optical lattice clock with uncertainty of. Metrologia, 56(6):065004, oct 2019.

[86] S. M. Brewer, J.-S. Chen, A. M. Hankin, E. R. Clements, C. W. Chou, D. J. Wineland, D. B. Hume, and D. R. Leibrandt. $^{27}\mathrm{al}^{+}$ quantum-logic clock with a systematic uncertainty below 10^{-18}. Phys. Rev. Lett., 123:033201, Jul 2019.

[87] Krehlik, P., Buczek, L., Kolodziej, J., Lipi´nski, M., ´Sliwczy´nski, L., Nawrocki, J., Noga´s, P., Marecki, A., Pazderski, E., Ablewski, P., Bober, M., Ciurylo, R., Cygan, A., Lisak, D., Maslowski, P., Morzy´nski, P., Zawada, M., Campbell, R. M., Pieczerak, J., Binczewski, A., and Turza, K. Fibre-optic delivery of time and frequency to vlbi station. A&A, 603:A48, 2017.

[88] Thilo Schuldt, Martin Gohlke, Markus Oswald, Jan Wüst, Tim Blomberg, Klaus Döringshoff, Ahmad Bawamia, Andreas Wicht, Matthias Lezius, Kai Voss, Markus Krutzik, Sven Herrmann, Evgeny Kovalchuk, Achim Peters, and Claus Braxmaier. Optical clock technologies for global navigation satellite systems. GPS Solutions, 25(3):83, Apr 2021.

[89] Hua Guan, Baolin Zhang, Huaqing Zhang, Yao Huang, Yanmei Hao, Mengyan Zeng, and Kelin Gao. 40ca+ optical clocks in china. AVS Quantum Science, 3(4):044701, 2021.

[90] Jacopo Grotti, Silvio Koller, Stefan Vogt, Sebastian Häfner, Uwe Sterr, Christian Lisdat, Heiner Denker, Christian Voigt, Ludger Timmen, Antoine Rolland, Fred N. Baynes, Helen S. Margolis, Michel Zampaolo, Pierre Thoumany, Marco Pizzocaro, Benjamin Rauf, Filippo Bregolin, Anna Tampellini, Piero Barbieri, Massimo Zucco, Giovanni A. Costanzo, Cecilia

Clivati, Filippo Levi, and Davide Calonico. Geodesy and metrology with a transportable optical clock. Nature Physics, 14(5):437–441, May 2018.

[91] Masao Takamoto, Ichiro Ushijima, Noriaki Ohmae, Toshihiro Yahagi, Kensuke Kokado, Hisaaki Shinkai, and Hidetoshi Katori. Test of general relativity by a pair of transportable optical lattice clocks. Nature Photonics, 14(7):411–415, 2020.

[92] Wesley Brand, Tobias Bothwell, Robert Fasano, Tristan Rojo, Richard Fox, and Andrew Ludlow. First deployments of nist's transportable yb optical lattice clock. Bulletin of the American Physical Society, 2023.

[93] Eng K. Wong, Mark Notcutt, Colin T. Taylor, Anthony G. Mann, and David G. Blair. Temperature-compensated cryogenic fabry–perot cavity. Appl. Opt., 36(33):8563–8566, Nov 1997.

[94] Josep Sanjuan, Norman Gürlebeck, and Claus Braxmaier. Mathematical model of thermal shields for long-term stability optical resonators. Opt. Express, 23(14):17892–17908, Jul 2015.

[95] Xiaotong Chen, Yanyi Jiang, Bo Li, Hongfu Yu, Haifeng Jiang, Tao Wang, Yuan Yao, and Longsheng Ma. Laser frequency instability of 6×10^{-16} using 10-cm-long cavities on a cubic spacer. Chinese Optics Letters, 18(11):030201, 3 2020.

[96] Qun-Feng Chen, Alexander Nevsky, Marco Cardace, Stephan Schiller, Thomas Legero, Sebastian Häfner, Andre Uhde, and Uwe Sterr. A compact, robust, and transportable ultra-stable laser with a fractional frequency instability of 1×10^{-15}. Review of Scientific Instruments, 85(11):113107, 2014.

[97] Ian R Hill, Richard J Hendricks, Sean Donnellan, Paul Gaynor, Ben Allen, Geoffrey P Barwood, and Patrick Gill. Dual-axis cubic cavity for drift-compensated multi-wavelength laser stabilisation. Opt. Express, 29(22):36758–36768, Oct 2021.

[98] Léa Bouffaut, Kittinat Taweesintananon, Hannah J. Kriesell, Robin A. Rørstadbotnen, John R. Potter, Martin Landrø, Ståle E. Johansen, Jan K. Brenne, Aksel Haukanes, Olaf Schjelderup, and Frode Storvik. Eavesdropping at the speed of light: Distributed acoustic sensing of baleen whales in the arctic. Frontiers in Marine Science, 9, 2022.

[99] Diane Rivet, Benoit de Cacqueray, Anthony Sladen, Aurélien Roques, and Gaëtan Calbris. Preliminary assessment of ship detection and trajectory evaluation using distributed acoustic sensing on an optical fiber telecom cable. The Journal of the Acoustical Society of America, 149(4):2615–2627, 04 2021.

[100] Martin Landrø, Léa Bouffaut, Hannah Joy Kriesell, John Robert Potter, Robin André Rørstadbotnen, Kittinat Taweesintananon, Ståle Emil Johansen, Jan Kristoffer Brenne, Aksel Haukanes, Olaf Schjelderup, and Frode Storvik. Sensing whales, storms, ships and earthquakes using an arctic fibre optic cable. Scientific Reports, 12(1):19226, Nov 2022.

[101] Nathaniel J. Lindsey, T. Craig Dawe, and Jonathan B. Ajo-Franklin. Illuminating seafloor faults and ocean dynamics with dark fiber distributed acoustic sensing. Science, 366(6469):1103–1107, 2019.

[102] Zhongwen Zhan, Mattia Cantono, Valey Kamalov, Antonio Mecozzi, Rafael Müller, Shuang Yin, and Jorge C. Castellanos. Optical polarization based seismic and water wave sensing on transoceanic cables. Science, 371(6532):931–936, 2021.

[103] Antonio Mecozzi, Mattia Cantono, Jorge C. Castellanos, Valey Kamalov, Rafael Muller, and Zhongwen Zhan. Polarization sensing using submarine optical cables. Optica, 8(6):788–795, Jun 2021.

[104] Mikael Mazur, Jorge C. Castellanos, Roland Ryf, Erik Borjeson, Tracy Chodkiewicz, Valey Kamalov, Shuang Yin, Nicolas K. Fontaine, Haoshuo Chen, Lauren Dallachiesa, Steve Corteselli, Philip Copping, Jurgen Gripp, Aurelien Mortelette, Benoit Kowalski, Rodney Dellinger, David T. Neilson, and Per Larsson-Edefors. Transoceanic phase and polarization fiber sensing using real-time coherent transceiver, 2021.

[105] Giuseppe Marra, Cecilia Clivati, Richard Luckett, Anna Tampellini, Jochen Kronjäger, Louise Wright, Alberto Mura, Filippo Levi, Stephen Robinson, André Xuereb, Brian Baptie, and Davide Calonico. Ultrastable laser interferometry for earthquake detection with terrestrial and submarine cables. Science, 361(6401):486–490, 2018.

[106] V Michaud-Belleau, H Bergeron, P S Light, N B Hébert, J D Deschênes, A N Luiten, and J Genest. Passive coherent discriminator using phase diversity for the simultaneous measurement of frequency noise and intensity noise of a continuous-wave laser. Metrologia, 53(5):1154, aug 2016.